
Simulation of Graphene Mechanics

Sandeep Kumar Jain

Cover page: Front page-honeycomb graphene lattice, back page-buckled graphene sheet with a Stone-Wales (a pair of pentagon and heptagon rings) defect in red color.

Copyright © 2017 by Sandeep Kumar Jain
PhD thesis, Utrecht University, the Netherlands, May 2017.
ISBN: 978-90-393-6751-3

Simulation of Graphene Mechanics

Simulatie van Grafeen Mechanica

(met een samenvatting in het Nederlands)

Proefschrift

ter verkrijging van de graad van doctor aan de Universiteit Utrecht op
gezag van de rector magnificus, prof. dr. G.J. van der Zwaan, ingevolge
het besluit van het college van promoties in het openbaar te verdedigen
op maandag 1 mei 2017 des middags te 2.30 uur

door

Sandeep Kumar Jain

geboren op 30 augustus 1990 te Rajasthan, India

Promotor: Prof. dr. G.T. Barkema

This thesis was financially supported by FOM-SHELL-CSER programme (12CSER049). This work is part of the research programme of the Foundation for Fundamental Research on Matter (FOM), which is part of The Netherlands Organisation for Scientific Research (NWO).

LIST OF PAPERS

- I S. K. Jain, G. T. Barkema, N. Mousseau, C. Fang and M. A. van Huis, "Strong long-range relaxations of structural defects in graphene simulated using a new semiempirical potential", *J. Phys. Chem. C*, 119:9646, 2015.
- II S. K. Jain, V. Juricic and G. T. Barkema, "Probing crystallinity of graphene samples via the vibrational density of states", *J. Phys. Chem. Lett.*, 6:3897, 2015.
- III S. K. Jain, V. Juricic and G. T. Barkema, "Boundaries determine the formation energies of lattice defects in two-dimensional buckled materials", *Phys. Rev. B*, 94:020102(R), 2016.
- IV S. K. Jain, V. Juricic and G. T. Barkema, "Structure of twisted and buckled bilayer graphene", *2D Mater.*, 4:015018, 2016.
- V S. K. Jain, V. Juricic and G. T. Barkema, "Probing the shape of a graphene nanobubble", *Phys. Chem. Chem. Phys.*, DOI:10.1039/C6CP08535K, 2017.
- VI A. J. Pool, S. K. Jain and G. T. Barkema, "Structural characterization of carbon nanotubes via the vibrational density of states", *Carbon*, DOI:10.1016/j.carbon.2017.03.030, 2017.

CONTENTS

1	Introduction	1
1.1	Graphene	2
1.1.1	Buckling and defects	3
1.2	Bilayer graphene	6
1.3	Graphene bubbles	7
1.4	Thesis outline	8
2	Long-range relaxations of structural defects in graphene	9
2.1	Introduction	10
2.2	Method	11
2.2.1	Empirical potential	11
2.2.2	Obtaining the fitting parameters from DFT calculations	12
2.3	Results and discussion	14
2.3.1	Stone-Wales defect	14
2.3.2	Line defect: dislocations formed by a separated SW defect	18
2.3.3	Effect of substrate	22
2.3.4	Grain boundaries (domains) in graphene	25
2.4	Conclusion	31
2.5	Acknowledgments	32
3	Probing crystallinity of graphene samples via VDOS	33
3.1	Introduction	34
3.2	Method	35
3.3	Results and discussion	36
3.3.1	Pristine flat and buckled graphene sheets	36
3.3.2	Point SW defects in flat and buckled graphene samples	37
3.3.3	Signatures of the domains and the substrate in the VDOS	40
3.4	Conclusion	40
3.5	Acknowledgments	42
4	Boundaries determine the formation energies of lattice defects in two-dimensional buckled materials	43
4.1	Introduction	44
4.2	Method	44
4.3	Results and discussion	45
4.3.1	Effective (1+1)D and (2+1)D models	45
4.3.2	Energetics of SW defect in graphene	48
4.3.3	Energetics of dislocations in graphene	52
4.4	Conclusion	54

4.5	Acknowledgments	54
4.6	Appendices	55
4.6.1	(1+1)D model	55
4.6.2	(2+1)D model	57
5	Structure of twisted and buckled bilayer graphene	61
5.1	Introduction	62
5.2	Method	63
5.3	Results and discussion	63
5.3.1	Structure of twisted bilayer graphene	63
5.3.2	Buckling in twisted bilayer graphene	68
5.4	Conclusion	73
6	Probing the shape of a graphene nanobubble	75
6.1	Introduction	76
6.2	Method	77
6.3	Results and discussion	77
6.3.1	Structure of graphene nanobubble	78
6.3.2	VDOS of graphene nanobubble	81
6.3.3	Elastic energy distribution in nanobubble	83
6.4	Conclusion	84
	Summary	85
	Samenvatting	87
	Bibliography	91
	Acknowledgements	105
	About the author	107

1

INTRODUCTION

In this chapter we give a brief introduction about graphene and its importance and applicability, various kinds of intrinsic defects in graphene, experimental techniques used in characterization, bilayer graphene, graphene bubbles and an overview of the chapters in the thesis.

1.1 Graphene

Carbon is the prime material for life on earth and fundamental for all organic and polymer chemistry. Various carbon structures are known because of the flexibility in its bonding nature. Graphite is a three-dimensional (3D) allotrope of carbon which is widely used in writing pencils.¹ Graphite is made of stacks of graphene layers which are weakly coupled by van der Waals forces. Graphene, a honeycomb lattice, is a two-dimensional (2D) allotrope of carbon and is the first 2D crystal ever isolated.² A carbon nanotube is a one-dimensional (1D) allotrope of carbon and can be obtained by rolling up the graphene layer along a particular direction.^{3,4} Fullerenes are molecules where carbon atoms are arranged spherically, and can be thought of as wrapped-up graphene by the introduction of pentagons in the otherwise hexagonal lattice. Therefore from the physical point of view fullerenes are considered as zero-dimensional (0D) carbon objects.⁵ These carbon based structures are shown in Figure 1.1.

The theoretical and experimental study of graphene and other 2D materials is an exceedingly growing field of today's condensed matter research. Over four hundred years after the invention of graphene, it was isolated in 2004 by mechanical exfoliation of pyrolytic graphite using scotch tape.⁶ This research was rewarded the Nobel Prize in Physics in 2010. Graphene is the first truly 2D crystal ever observed in nature. The stability of 2D crystals has been doubted in the past, namely due to the Mermin-Wagner theorem which states that a 2D crystal loses its long-range order, and therefore melts, at any small non-zero temperature due to thermal fluctuations.^{7,8}

Graphene has emerged as one of the most remarkable new materials of the last decade due to its extraordinary and unusual electronic, mechanical, optical and thermal properties.^{2,6,9–13} These peculiar properties of graphene have provoked a revolution in nanotechnology and semi-conductor industry. The carrier density in a graphene sheet can be controlled by simple application of a gate voltage.⁶ This effect is a fundamental element for the design of electronic devices. The miniaturization of electronic devices can be improved significantly by using transistors made up of graphene strips. Graphene has emerged as the strongest material ever found¹³ therefore suggesting its potential applications as hierarchical structures and membranes in biological materials, nanocomposites featuring superior stiffness, dry lubricants for macroscale metallic sliding components and high-pressure contacts.^{14,15} The very high thermal conductivity of graphene makes it useful in photovoltaics and energy storage devices.

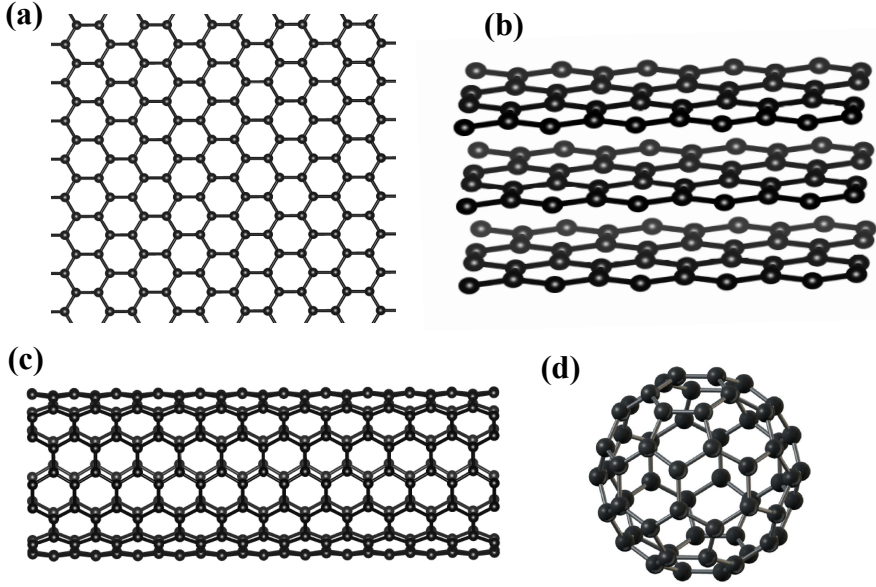


Figure 1.1: Carbon based structures. (a) Graphene is a 2D honeycomb lattice. (b) Graphite can be viewed as a stack of graphene layers. (c) Carbon nanotubes are 1D allotrope of carbon and can be viewed as rolled-up graphene cylinders. (d) Fullerenes are considered as wrapped graphene with pentagons.⁵

Graphene has a sp^2 hybridized structure where each carbon atom is connected to three nearby carbon atoms constructing a hexagonal lattice. The carbon-carbon bond separation distance in graphene is 1.42 Å. Experimental fabrication of graphene can be achieved by various techniques such as exfoliation of graphite,⁶ epitaxial growth on a SiC substrate,¹⁶ and chemical vapor deposition (CVD) on germanium (Ge),¹⁷ ruthenium (Ru),¹⁸ and iridium (Ir).¹⁹

1.1.1 Buckling and defects

Graphene is a one atom thick two-dimensional system embedded in three dimensional space. Hence, it is subjected to out-of-plane distortions due to thermal fluctuations and interaction with a substrate; mainly referred as ripples and buckles.^{20,21} The purity of graphene samples is crucial for both their practical and experimental use. The experimentally synthesized graphene samples are quite generically polycrystalline and therefore contain structural lattice defects.^{22,23}

These defects generally play a role in many characteristics of graphene such as the conductivity, mechanical strength and optical properties. In this regard, their detection is of crucial importance. Intrinsic defects such as Stone-Wales (SW) and similar defects made of polygons different than hexagons are frozen in during the production of large graphene samples, as is experimentally observed.^{24–26}

Based on dimensionality, various defects in graphene have been categorized. Point defects, typically SW defects, vacancies or interstitial atoms, are zero-dimensional defects. Separated dislocations and line defects are considered as one-dimensional defects whereas network of grain boundaries or stacking faults are two-dimensional defects.²³ An SW defect consists of two pentagons and two heptagons²⁷ and can be considered as a dislocation dipole. The structures of various defects in graphene are shown in Figure 1.2. Experimentally, SW defects are formed via rapid quenching from high temperature or under irradiation.²² When four hexagons are converted into a pair of pentagons and heptagons in order to create an SW defect, the change in bond angles and bond lengths is significant, forcing buckling to decrease the induced strain. In Chapter 2, we study the long-range structural relaxations due to the defects in graphene via computer simulations.

Several experimental techniques have been used to study lattice defects in graphene. Scanning tunneling microscopy (STM),^{28,29} transmission electron microscopy (TEM),^{22,30} and atomic force microscopy (AFM)^{31,32} have been used to obtain images of graphene with defects with atomic resolution. Apart from these direct techniques the indirect ones, among which Raman spectroscopy,^{33–35} X-ray absorption spectroscopy,^{36–38} inelastic electron tunneling spectroscopy (IETS),^{39–41} and neutron scattering^{42,43} are also widely used in characterization of defects in graphene.

The production of high-quality graphene samples would benefit from a non-intrusive way to monitor the quality, i.e. crystallinity, of the film. Candidate experimental techniques include Raman scattering, IETS, infrared spectroscopy (IR) and inelastic neutron scattering spectroscopy. For all these techniques, an interpretation of the measurement data requires an understanding of the vibrational density of states (VDOS). In Chapter 3, we study the vibrational spectrum of graphene in order to characterize various defects.

Computer simulations are widely in use to study the buckling defects in various 2D materials. Georgii *et al.*, for example, have reported three different out-of-plane buckling modes because of an SW defect and their activation barrier in carbon nanotubes (CNTs).⁴⁴ The formation and activation energies of a single SW defect in graphene have been calculated using various methods like quantum molecular dynamics calculations,⁴⁵ density functional theory (DFT) calculations,^{46,47} and using the combination of a semiempirical *ab initio* method

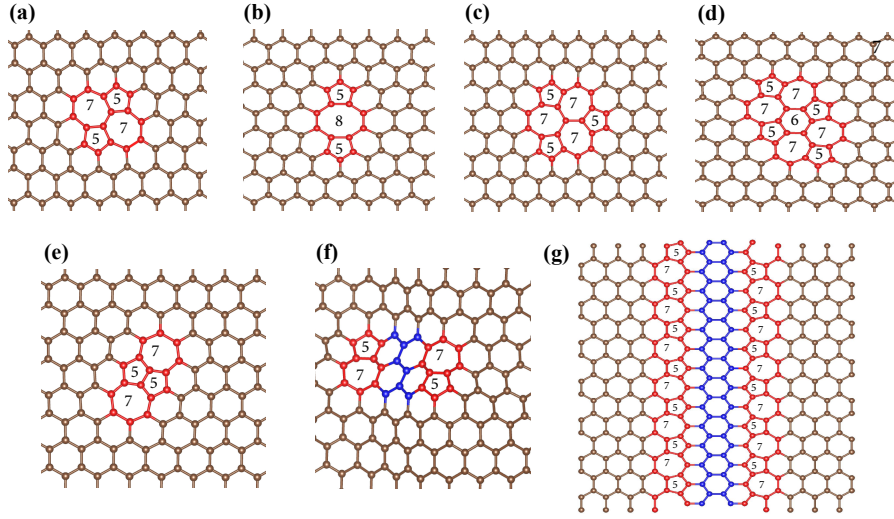


Figure 1.2: Structures of various defects in graphene. (a) Stone-Wales (SW) defect is considered as a dislocation dipole. (b-d) various types of di-vacancy defects in graphene. (e) Two carbon adatoms give rise to the structure of inverse Stone-Wales defect. (f) Separated dislocations. (g) Grain boundaries (line of 5-7 rings) in graphene.

and an Amber force field.⁴⁸ The main problem with various quantum chemical methods such as DFT is that these calculations are limited in system size since computationally they are very demanding. This problem can be overcome by the development of an effective empirical potential which can describe the structural properties of graphene quite accurately. In this way one has the flexibility to study very large samples with far less computational requirements. This is important to study the long range structural relaxations in the form of buckling due to a defect, to capture the finite size effect of the defect formation energy, and in the studies of vibrational properties.

Bond order empirical potentials such as the reactive empirical bond order (REBO) potential,⁴⁹ Brenner potential,⁵⁰ Tersoff potential,⁵¹ and reactive force field (Reaxff) potential⁵² are frequently used in the simulations of various carbon materials. Harmonic potentials such as Kirkwood's⁵³ and Keating's,⁵⁴ represent a cheap and surprisingly accurate approach to study elastic deformation in fully connected covalent systems, even when fully disordered, with only a few fitted parameters.^{55,56} These simple potentials also allow us to better understand the origin of the various energy contributions. Therefore we develop in Chapter 2, a semiempirical potential based on Kirkwood's and Keating's potentials to study the structural properties of graphene.

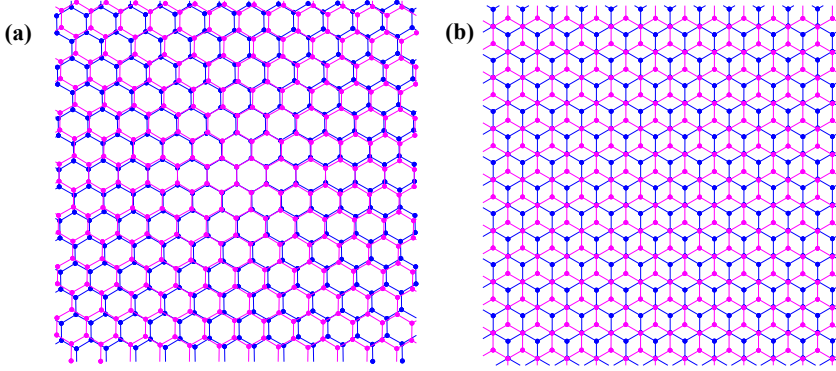


Figure 1.3: Atomic structures of two types of stackings in bilayer graphene. (a) Atomic structure of a vortex region (AA stacking). (b) Atomic structure of a Bernal stacked region (AB/BA stacking).

1.2 Bilayer graphene

Bilayer graphene (BLG) consists of two stacked graphene sheets with usually a stacking of either AB (Bernal) or AA type as shown in Figure 1.3. However, two graphene layers can also be placed on top of each other in other arrangements, characterized in general by a mismatch angle θ . Such a structure is usually referred to as twisted bilayer graphene (TBLG),^{57,58} and represents an example of a Van der Waals heterostructure.⁵⁹ Since TBLG is made of two stacked misaligned lattices, a superlattice with a larger periodicity known as Moiré pattern emerges in the structure.^{60–63}

Recently, this form of BLG has attracted a lot of attention theoretically and experimentally due to its exotic electronic^{64–72} and optical properties^{73–75} arising due to the formation of the Moiré patterns. In particular, it has been theoretically suggested that the twist in the BLG may lead to a renormalization of the Fermi velocity,⁷⁶ possible appearance of the flat electronic bands,⁷⁷ neutrino-like oscillation of Dirac fermions⁷⁸ as well as localization of electrons.⁷⁹ Moreover, TBLG when placed in a magnetic field, exhibits a fractal spectrum of the Landau levels.⁸⁰ The theoretical interest has been motivated by the experimental observation of TBLG with Moiré patterns in samples grown on SiC substrates,⁸¹ and using chemical vapour deposition.^{82,83} Furthermore, the mismatch angle has a significant impact on the quantum Hall effect in TBLG, as has been recently

reported;⁸⁴ and breaking of the interlayer coherence for very small angles was experimentally found as well.⁸⁵ In Chapter 5, we study the structure of twisted and buckled bilayer graphene with a combination of effective intralayer and interlayer potentials.

1.3 Graphene bubbles

As mentioned before, graphene has emerged as a very strong material¹³ and N-doped graphene has been recently reported as the stiffest material ever found.⁸⁶ Its mechanical properties are also fundamentally and practically interesting when it is in contact with other materials. An important physical and chemical aspect of graphene is its ability to trap gas molecules under high pressure when placed on different substrates, leading to a formation of bubbles with nanometer to micrometer sizes. Such nanobubbles have been experimentally observed in a graphene membrane placed on top of a SiO₂/Si substrate,^{87,88} epitaxial graphene grown on 4H-SiC,⁸⁹ and in an irradiated graphene sample on Ir.⁹⁰ Experimentally, it is observed that absorbed water and hydrocarbons between graphene and substrates can also lead to sub-micron sized bubbles.^{91,92} The bubbles have been used for Raman characterization of strained graphene⁹³ and have been reported to induce pseudo-magnetic fields greater than 300 T at room temperature.⁹⁴ The van der Waals (vdW) pressure inside the bubble has an important role in determining the properties of the trapped materials.^{95,96} Pressure due to the confinement can modify the properties of a material, e.g., ice in graphene nanocapillaries at room temperature,^{97,98} nanocrystals and biological molecules trapped in graphene liquid cells.^{99–101}

Nanobubbles proved to be an effective tool for strain engineering which is used to modify electronic and mechanical properties of graphene.^{102,103} Controllable curvature of graphene bubbles can be used as optical lenses with variable focal length.⁸⁸ Gas molecules in graphene bubbles on patterned substrates have shown remarkable impermeability¹⁰⁴ therefore suggesting the applicability in gas storage devices.^{87,105} Graphene nanobubbles are also used to measure elastic properties and the adhesion energy between substrates.¹⁰⁶ Very recently, nanobubbles of different sizes, ranging from a few tens of nanometers to a micrometer, and shapes, such as circular, trapezoidal, and triangular, have been found in van der Waals heterostructures.¹⁰⁷ In Chapter 6, with our computer simulations we capture the universal scaling behavior in the shape of graphene nanobubbles.

1.4 Thesis outline

Here we briefly outline the rest of the thesis. In Chapter 2, we present our newly developed semiempirical potential with an out-of-plane energy term fitted with density functional theory (DFT) calculations. We use this potential in the simulations of various defects such as SW defects, separated dislocations and grain boundaries. In Chapter 3, we show that the crystallinity of graphene samples can be determined via the VDOS. In Chapter 4, we present our study on the boundary effect on the formation energy of lattice defects in 2D materials. By using a combination of intralayer and interlayer potentials we study the structure of twisted and buckled bilayer graphene which is discussed in Chapter 5. In Chapter 6, we discuss the shape of a gas bubble trapped between graphene and a substrate.

LONG-RANGE RELAXATIONS OF STRUCTURAL DEFECTS IN GRAPHENE

Abstract: We present a new semiempirical potential for graphene, which includes also an out-of-plane energy term. This novel potential is developed from density functional theory (DFT) calculations for small numbers of atoms, and can be used for configurations with millions of atoms. Our simulations show that buckling caused by typical defects such as the Stone-Wales (SW) defect extends to hundreds of nanometers. Surprisingly, this long-range relaxation lowers the defect formation energy dramatically - by a factor of 2 or 3 - implying that previously published DFT-calculated defect formation energies suffer from large systematic errors. We also show the applicability of the novel potential to other long-range defects including line dislocations and grain boundaries, all of which exhibit pronounced out-of-plane relaxations. We show that the energy as a function of dislocation separation diverges logarithmically for flat graphene, but converges to a constant for free standing buckled graphene. A potential in which the atoms are attracted to the 2D plane restores the logarithmic behavior of the energy. Future simulations employing this potential will elucidate the influence of the typical long-range buckling and rippling on the physical properties of graphene.

This chapter is based on "Strong long-range relaxations of structural defects in graphene simulated using a new semiempirical potential" by S. K. Jain, G. T. Barkema, N. Mousseau, C. Fang and M. A. van Huis, *J. Phys. Chem. C*, 119:9646, 2015.

2.1 Introduction

The unusual electronic and mechanical properties make graphene an important component in the nanotechnology and semiconductor industry.^{24,108,109} For these applications, however, defects need to be closely controlled since they can significantly alter the physical and chemical properties of graphene.^{110,111} We are interested here in pronounced out-of-plane deformations (buckling) that arise naturally in the presence of defects in the two-dimensional (2D) structure of graphene.^{20,112–114} These deformations occur already in the presence of intrinsic defects, the simplest defects in graphene. We study zero-, one- and two-dimensional defects. Specifically, we consider a Stone-Wales (SW) defect, a dislocation line caused by the separation of two pairs of pentagon-heptagon rings, and grain boundaries.

Since buckling depends on the defect rotation angle and shear force, defect orientation is important.^{115,116} The most stable buckling mode for an SW defect in graphene is the mode where one pentagon ring moves above the plane and the other below the plane at the dislocation core.^{47,117} Moreover, and in agreement with the Mermin-Wagner theorem that states that the energy should diverge logarithmically and dislocations should attract each other in a two-dimensional sheet,^{7,8} Samsonidze *et al.* have shown that the attraction potential increases logarithmically as a function of the distance between dislocations.¹¹⁸

In this chapter, we further characterize this attraction potential in graphene's both flat and buckled modes. Experimental evidence shows that out-of-plane buckling in the graphene due to the dislocation dipole is quite significant and has a long-range effect that extends well beyond the size accessible to DFT calculations.^{119–121} It is necessary, therefore, to turn to empirical potentials to study this effect. While empirical potentials for carbon have already been reported in the literature, such as the Tersoff-Brenner^{50,51} and the Stillinger-Weber potentials,¹²² they have not been fitted directly to graphene. Here, we turn to a simpler harmonic form based on the Keating potential⁵⁴ and Kirkwood potential⁵³ to describe the covalent bonds. We add an out-of-plane energy term, that is missing in all these empirical potentials, which allows us to better reproduce experimental and *ab initio* results, and to better understand the effects of intrinsic defects on the graphene sheet structure.

We first present the semi-empirical potential as fitted from DFT-calculations, and show its good performance in predicting structural properties of graphene, such as the elastic constants. Using this novel potential, we then study the effect

of defects themselves on buckling. In particular, we look at a single SW defect and at the buckling caused by the splitting of an SW defect into a dislocation pair. We find that the elastic energy does not diverge logarithmically for buckled structures and we propose a mechanism to restore this logarithmic behavior. We further demonstrate the applicability of the potential by simulating grain boundaries in graphene for both flat and buckled modes.

2.2 Method

In this section we describe the empirical potential with an out-of-plane energy term and fitting of elastic parameters from DFT-calculations.

2.2.1 Empirical potential

Harmonic potentials such as Kirkwood's⁵³ and Keating's,⁵⁴ represent a cheap and surprisingly accurate approach to study elastic deformation in fully connected covalent systems, even when fully disordered, with only a few fitted parameters.^{55,56} These simple potentials also allow us to better understand the origin of the various energy contributions.

For semiconductors, these potentials typically include two energy terms—a two-body bond-stretching and a three-body angular contribution—and offer similar predictive quality, differing only in the details of implementation. While the Keating potential is more commonly used for computational convenience, Kirkwood's representation has the advantage of providing a full separation between bond-stretching and angular contributions.¹²³ Because, with current computing capabilities, cost difference between these representations is not an issue, we retain the second form, for formal convenience.

For a two-dimensional hexagonal network, Kirkwood's potential is written as

$$E_0 = \frac{3}{16} \frac{\alpha}{d^2} \sum_{i,j} (r_{ij}^2 - d^2)^2 + \frac{3}{8} \beta d^2 \sum_{j,i,k} \left(\theta_{j,i,k} - \frac{2\pi}{3} \right)^2 \quad (2.1)$$

where α and β are parameters fitted to the bulk and shear modulus, and the $2\pi/3$ term enforces 120 degree angles between the bonds.

To allow for deformation in the third dimension, here we introduce an additional term that imposes a harmonic restoring force in addition to the fourth-order energy correction that comes out from the bond-stretching pair term. The final potential is therefore written as

$$E = \frac{3}{16} \frac{\alpha}{d^2} \sum_{i,j} (r_{ij}^2 - d^2)^2 + \frac{3}{8} \beta d^2 \sum_{j,i,k} (\theta_{j,i,k} - \frac{2\pi}{3})^2 + \gamma \sum_{i,jkl} r_{ijkl}^2 \quad (2.2)$$

with $d = 1.420$ Å, the ideal bond length for graphene, and the other parameters being extracted from DFT calculations are: $\alpha = 26.060$ eV/Å², $\beta = 5.511$ eV/Å² and $\gamma = 0.517$ eV/Å². Here, r_{ijkl} is the distance between atom i and the plane through the three atoms j , k and l connected to atom i .

2.2.2 Obtaining the fitting parameters from DFT calculations

Parameters for the empirical potential are fitted from DFT calculations using the first-principles Vienna *ab initio* Simulation Package (VASP).^{124, 125} To describe buckling accurately, we used a van der Waals functional,¹²⁶ which is shown to work well for solids.¹²⁷ The van der Waals functional was formulated by Dion and co-workers.¹²⁸ The cut-off energy of the wave functions was 400 eV. The cut-off energy of the augmentation functions was about 650 eV. The electronic wave functions were sampled on a $6 \times 8 \times 1$ grid with 24 k-points in the irreducible Brillouin zone (BZ) of graphene using the Monkhorst and Pack method.¹²⁹ Structural optimizations were performed for both lattice parameters and coordinates of atoms. Different k-meshes were tested for a primitive graphene cell, and the cut-off energies for the wave functions and augmentation wave functions were also tested in order to ensure good energy convergence (< 1 meV/atom).

The various parameters were fitted by imposing elastic deformation onto a graphene sheet. The value of α was obtained by fitting the quadratic energy evolution as a function of uniform deformations on a 50-atom monoclinic perfectly crystalline graphene sample as shown in Figure 2.1(a). Since this is a homogeneous compression, with deformation constrained to the plane, only the two-body term in the potential contributes to the energy. The obtained value, $\alpha = 26.060$ eV/Å², is in good agreement with the reported experimental value of 25.880 eV/Å².^{38, 130}

To obtain β , we repeat the procedure, this time by shearing the box, i.e. changing the angle between the periodicity vectors L_x and L_y . During the process of

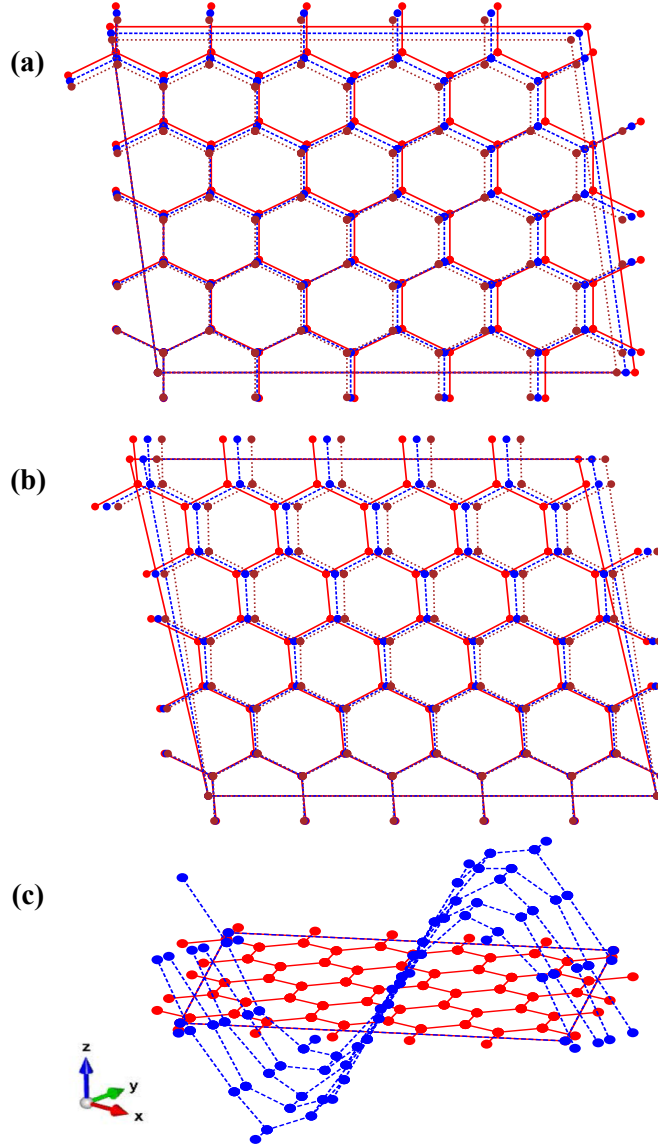


Figure 2.1: Fifty-atom samples in which different kinds of elastic modes are excited. (a) Homogeneous compression of the box. (b) Shearing of the box at constant area. (c) Sinusoidal displacement in the z -direction. These excitations are used to determine the parameters α , β and γ in our potential eq. (2.2).

shearing the box, the area is kept constant by scaling the box length in the y -direction accordingly, as shown in Figure 2.1(b). The energy as a function of shearing is also well fitted by a quadratic equation, leading to $\beta = 5.511 \text{ eV}/\text{\AA}^2$.

Finally, γ is obtained through sinusoidal displacements in the z -direction given as

$$z_i = A \sin \left(\frac{2\pi k x_i}{L_x} \right). \quad (2.3)$$

The amplitude A of the displacement is varied from -0.1 to 0.1 \AA as shown in Figure 2.1(c). Deformed samples are allowed to relax laterally at the fitted value of α and β .

The energy of these laterally relaxed samples is then fitted to

$$E = E_0 N + \gamma^l A^2 \left(\frac{k}{L_x} \right)^2 N. \quad (2.4)$$

Here, N is the total number of the atoms in the sample and γ^l is a fitting parameter. The energies of these samples were also computed by DFT, employing the same boundary conditions and fitted to eq. (2.4). Whereas the value thus found, $\gamma = 0.517 \text{ eV}/\text{\AA}^2$, is almost 2 orders of magnitude smaller than α and one order of magnitude smaller than β , it remains significant, demonstrating the need to include such a harmonic term in the potential energy.

2.3 Results and discussion ---

To demonstrate the applicability of this novel potential, we study the deformation caused by intrinsic defects in graphene. The effect of defects on the geometry of a graphene sheet is examined in three parts. First, we look at the long-range deformation associated with the creation of an SW defect, representing a dislocation dipole. We then consider two types of line defects; split dislocation pairs and grain boundaries.

2.3.1 Stone-Wales defect ---

A single SW defect (5-7-7-5 member rings)²⁷ is created in a perfectly hexagonal lattice via a bond-switching move as shown in Figure 2.2. After the bond trans-

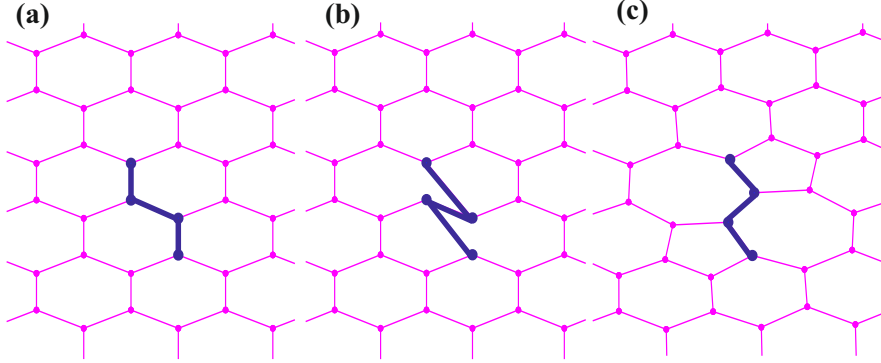


Figure 2.2: Creation of single Stones-Wales defect by bond transposition. (a) A perfect hexagonal arrangement. (b) Bonds are rearranged to create the topology of a defect. (c) The atomic positions are relaxed to generate a single SW defect.

position, the sample is relaxed with the novel potential, both when constraining the atoms in the 2D plane and when allowing full 3D relaxation. Several samples containing different numbers of atoms are generated to study the formation energy of SW defect in both flat and buckled modes.

We first compare the SW-defect formation energy for the DFT and the semiempirical description using a small 42-atom model with a fixed area, to maintain a constant electronic density. Periodic boundary conditions apply in all cases. For the 2D relaxation, we find a good agreement between formation energy of 7.95 eV as obtained from DFT calculations and the value of 7.50 eV obtained when using the Kirkwood-like potential (Table 2.1). To trigger relaxation in the third dimension, the symmetry is broken by the addition of a small out-of-plane displacement (0.01\AA) with alternating sign to the atoms participating to the SW defect. This buckling initialization was adopted to avoid metastable configurations. This leads to a staggered configuration that is of lower energy with atoms moving above and below the plane during the relaxation.⁴⁴ As seen in Table 2.1, the additional degree of freedom in the out-of-plane direction reduced the strain by more than 2 eV in the small box.

We also study the energy convergence of the SW defect with system size, looking at systems ranging from $N = 42$ to 69200 atoms. This time, we allow the box size to relax, which also decreases the elastic energy by more than 2 eV (Table

Table 2.1: Formation energy of an SW defect calculated using DFT and using our semi-empirical potential. These values are obtained for a 42-atom sample at fixed crystalline density. The value E_{2d} is obtained in a planar geometry, and the value E_{3d} is obtained with out-of-plane relaxation. ΔE is the energy difference between these two configurations after relaxation.

Method	E_{2d} (eV)	E_{3d} (eV)	ΔE (eV) = $E_{2d} - E_{3d}$
DFT	7.952	5.933	2.019
Semiempirical potential	7.496	5.274	2.222

Table 2.2: Formation energy of an SW defect calculated using our semi-empirical potential. The value E_{2d} is obtained in a planar geometry, and the value E_{3d} is obtained with out-of-plane relaxation. In contrast to Table 1, the density is not fixed to its crystalline value but the box is allowed to relax (box lengths L_x and L_y as well as the angle between them). ΔE represents the energy difference between the two energy-minimized structures and Δz_{max} , the buckling height, defined as the difference between maximum and minimum z -direction coordinates.

Sample size (Number of the atoms)	E_{2d} (eV)	E_{3d} (eV)	ΔE (eV) = $E_{2d} - E_{3d}$	Δz_{max} (Å)
42	5.963	2.636	3.327	2.460
336	6.642	2.814	3.823	3.226
680	6.686	2.831	4.037	3.640
1008	6.700	2.840	3.860	3.939
1344	6.707	2.843	3.864	4.190
3344	6.721	2.852	3.869	5.215
6696	6.725	2.856	3.869	6.190
17200	6.728	2.861	3.867	7.790
34160	6.729	2.866	3.863	9.178
69200	6.729	2.868	3.861	10.855

2.2). Nevertheless, size convergence for both relaxation types is slow. In the 2D case, the elastic energy associated with the SW defect is 5.96 eV for a 42-atom structure, and converges to 6.73 eV for a system containing 6696 atoms. Overall, the formation energy for the 2D SW defect is in very good agreement with values reported in the literature calculated by DFT⁴⁷ and using a combination of semiempirical *ab-initio* method and an amber force field⁴⁸ for small samples.

The energy (E_{3d}) for the buckled samples is significantly lower (around 3.86 eV) than for the 2D-constrained models. The resulting 3D relaxation leads to a local minimum-energy structure for the SW defect, with one pentagon ring moving above the plane while the other moves below the plane. The bond connecting

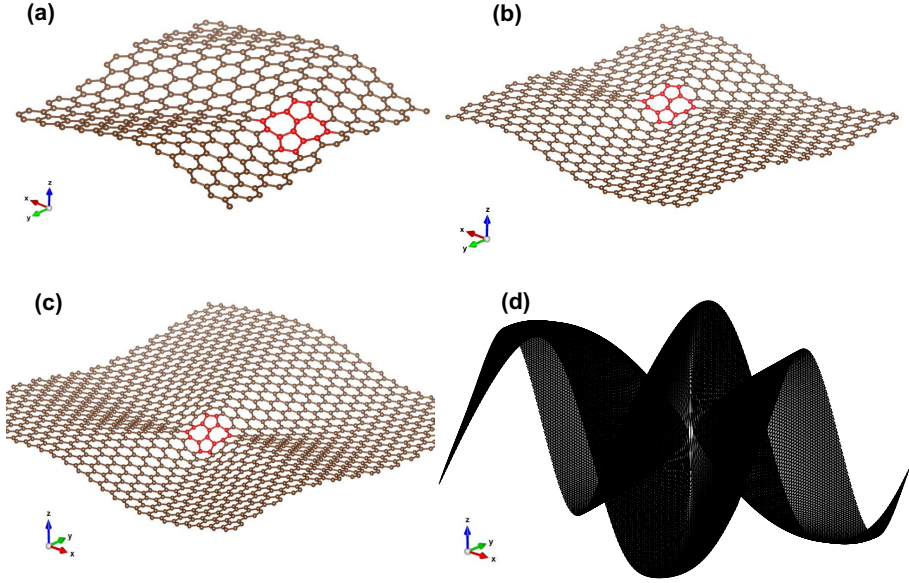


Figure 2.3: Well-relaxed buckled graphene samples having a single SW defect. Periodic boundary conditions apply. During the minimization process one pentagon ring goes above the plane and another goes below the plane. These out-of-plane displacements extend throughout the sample causing long-ranged buckling. (a) Sample with 336 atoms with x and y dimensions of ~ 40 Å and bulging in z -direction up to ~ 3 Å. (b) Sample with 680 atoms with x and y dimensions of ~ 50 Å and bulging in z -direction up to ~ 3.5 Å. (c) Sample with 1344 atoms with x and y dimensions of ~ 60 Å and bulging in z -direction up to ~ 4 Å. (d) Sample with 69200 atoms with x and y dimensions of ~ 500 Å and bulging in z -direction up to ~ 11 Å.

both rings has the tendency to be at an angle of inclination of approximately 18° with respect to the plane. This relaxation is accompanied by significant buckling — varying from 2.5 Å for the smallest box to almost 11 Å for the largest system — that continues to grow with system size, a phenomenon that cannot be captured with small DFT calculations (see Figure 2.3). Note that the formation energy of the 3D SW defect for the largest system is 2.87 eV, which is more than two times lower than the DFT-calculated value of 5.93 eV for the small 42-atom sample. This clearly shows that long-range relaxation can drastically reduce defect formation energies, and that these effects cannot be studied using only DFT simulations.

Figure 2.4 shows $\ln \left[1 - \frac{E}{E_{(\infty)}} \right]$ as a function of $\ln(N)$ with $E_{2d(\infty)}$ and $E_{3d(\infty)}$ determined by extrapolation to be 6.729 eV and 2.869 eV, respectively. These data points were fitted by a straight line. In the 2D case the straight line has a

slope of -1.0 and intercept of 1.48 . In the 3D case, we observe rather a slope of -0.5 and an intercept of -1.07 . Since \sqrt{N} is proportional to the sample size (L) we can conclude that E_{3d} has a finite size correction that scales as $1/L$ in the energy, whereas E_{2d} has a finite size correction of $1/L^2$ in the energy.

2.3.2 Line defect: dislocations formed by a separated SW defect

An SW defect represents a dislocation dipole. The dislocation pairs (pentagon-heptagon rings) can then be separated by inserting hexagon rings in between them, leading to the creation of a line defect as shown in Figure 2.5.

The energy as a function of dislocation separation Δ is shown in Figure 2.6. In the 2D case where atomic motion is constrained to the xy -plane, the energy diverges logarithmically as a function of Δ ; this is consistent with the Mermin-Wagner theorem^{7,8} and the KTHNY Theory^{131–133} (see Figure 6(a)). This energy evolution was fitted to the equation

$$E_{2d}(\Delta) = a + b \ln \left[\frac{1}{\Delta + c} + \frac{1}{P - \Delta + c} \right]^{-1} \quad (2.5)$$

where a , b and c , are the fitting parameters and P is the total number of the hexagonal rings in the direction of Δ . For the 69200-atom sample, we consider $P=171$ and $\Delta_{max}=85$.

As the symmetry is broken through the introduction of small perturbations along the z -axis, relaxation is more effective and the energy as a function of dislocation separation converges to a constant with corrections scaling as $\frac{1}{\sqrt{\Delta}}$ for large values of Δ . Lehtinen *et al.* have shown experimentally that the evolution of dislocations in 2D systems is governed by long-range out-of-plane buckling.¹²¹ Our simulations also indicate that line defects in graphene (a dislocation pair) can have significant impact on buckling.

For our 69200-atom sample, for example, buckling increases dramatically with respect to dislocation separation. The buckling height increases from 10.9 \AA for $\Delta = 0$ to 46.5 \AA for $\Delta = 85$. Moreover, the interaction between dislocations, in this case, is not monotonic: whereas in 2D interaction remains attractive at all distances, the interaction changes sign when 3D relaxation is allowed and becomes repulsive after some threshold distance as can be clearly seen in Figure 2.6(b). These effects could not be observed numerically before due to the small sample sizes used previously. The behavior of the elastic energy as a

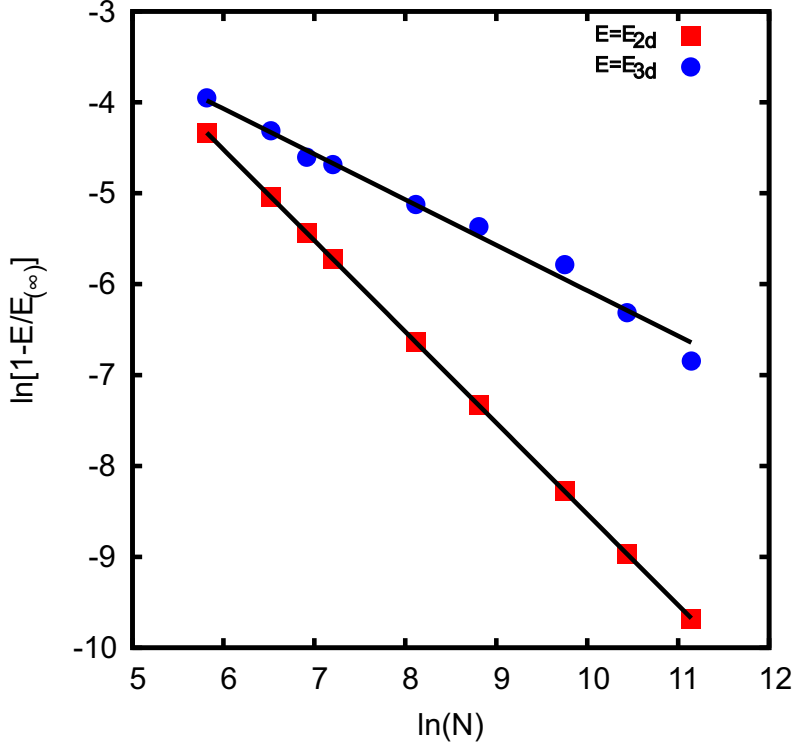


Figure 2.4: Effect of finite box size on SW formation energy, with and without buckling. We expect the energy to scale as $E(N) = E(\infty) - CN^{-p}$. Hence, $\ln[1 - E(N)/E(\infty)] = \ln(C/E(\infty)) - p \ln(N)$. The data fall on straight lines with our extrapolated energies $E_{2d(\infty)} = 6.729$ eV and $E_{3d(\infty)} = 2.869$ eV, with slopes -1.0 and -0.5 , respectively. This suggests that finite-size corrections are $\sim 1/L^2$ and $\sim 1/L$, respectively.

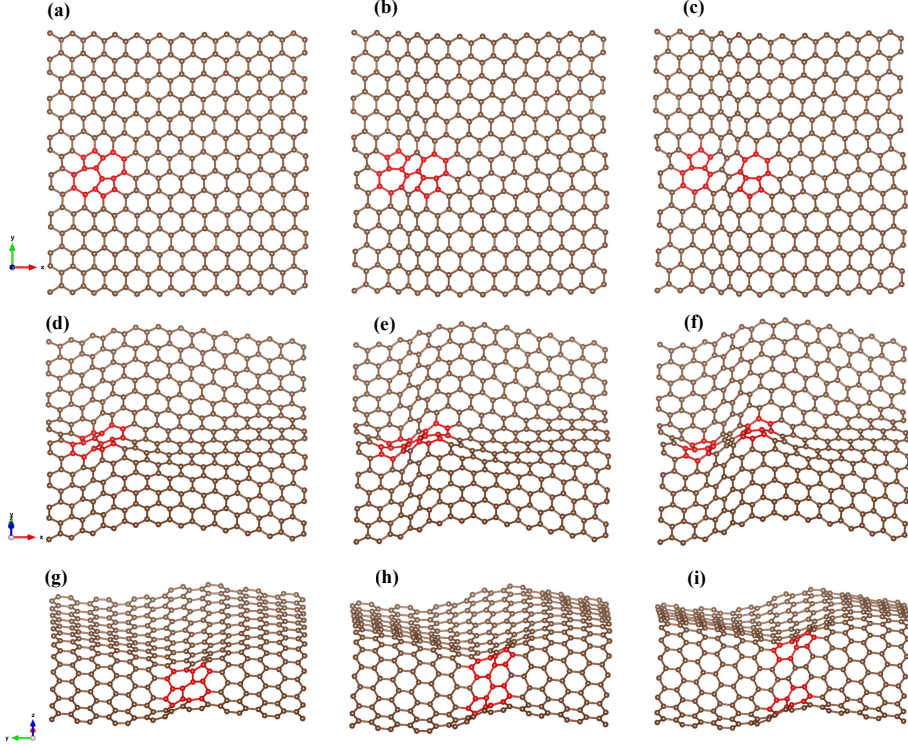


Figure 2.5: Structural changes induced by a pair of (5-7) dislocations after 3D relaxation. (a,d,g) Samples with a single Stone-Wales defect at various viewing angles (b,e,h) Dislocations separated by one hexagonal ring ($\Delta = 1$). (c,f,i) Dislocations separated by two hexagonal rings ($\Delta = 2$).

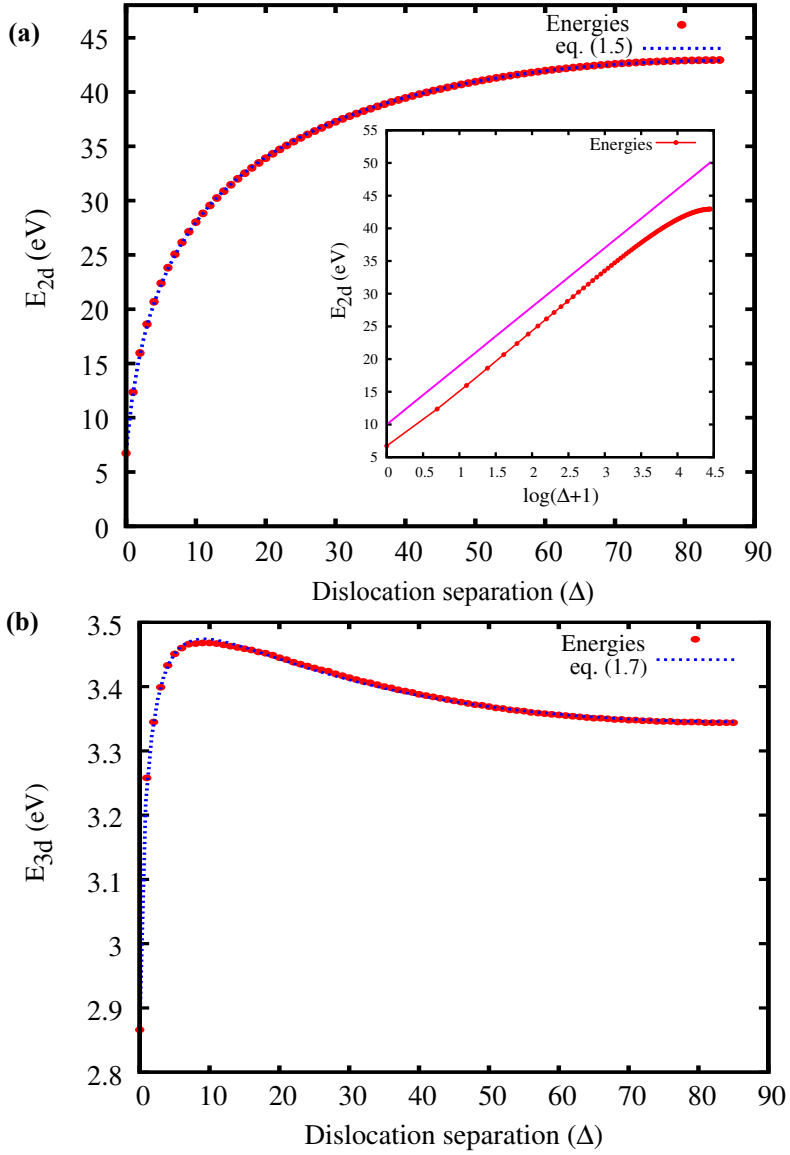


Figure 2.6: Energy ($E(\Delta)$) as a function of dislocation separation (Δ) in a 69200-atoms sample. (a) Without out-of-plane relaxation, the data points are well fitted by eq. (2.5) (line). The inset shows the logarithmic increase of the energy with Δ , which flattens once Δ approaches half the box size; the straight line is drawn to guide the eye. (b) Relationship found when out-of-plane relaxation is allowed, this time fitted by eq. (2.7) (line).

function of distance between two dislocations when 3D relaxation is allowed can be described by

$$f(\Delta) = a + \frac{c + b\sqrt{\Delta}}{d + \Delta} \quad (2.6)$$

and

$$E_{3d}(\Delta) = f(\Delta) + f(P - \Delta) \quad (2.7)$$

where a , b , c and d are the fitting parameters and P is the system size defined as total number of the six member rings in the direction of Δ . For large values of Δ , the force acting between the dislocation pairs can be written together for 2D and 3D cases as

$$F(\Delta) \propto \frac{1}{\Delta^{D/2}} \quad (2.8)$$

with D the dimensionality of the system.

2.3.3 Effect of substrate

To simulate the effect of substrate on the buckling of graphene, we add a harmonic confining energy term in our potential. The logarithmic divergence of the energy as a function of dislocation separation is again restored by this harmonic confinement energy term that is given as:

$$E_c = K \sum_{i=1}^N z_i^2. \quad (2.9)$$

K is the prefactor for this harmonic term ($\text{eV } \text{\AA}^{-2}$), N is number of the atoms present in the sample and z_i is the normal-to-plane coordinate of the atom. So, all the buckled graphene samples relaxed back to the 2D plane with the confinement potential given in eq. (2.9) for different values of K . The energy as a function of Δ was calculated and plotted as shown in Figure 2.7. It is evident from the plot that for any non-zero value of K the logarithmic behavior of the energy again restores and at $K = 5 \text{ eV } \text{\AA}^{-2}$ the energy plot overlaps with the $E = E_{2d}$ plot. With this additional confining term E_c in the potential, samples again have the tendency to become flat with some small z -direction fluctuations at the core of the defect. It has been observed that for the case $K = 0 \text{ eV } \text{\AA}^{-2}$ (free standing buckled graphene), the z -direction displacement increases with increasing dislocation separation (Table 2.3). However when a non-zero harmonic confinement potential is applied, z -direction displacements become very small and also very local near the dislocation core (Figure 2.8). These buckling heights become smaller and smaller with strong harmonic confinement. Therefore,

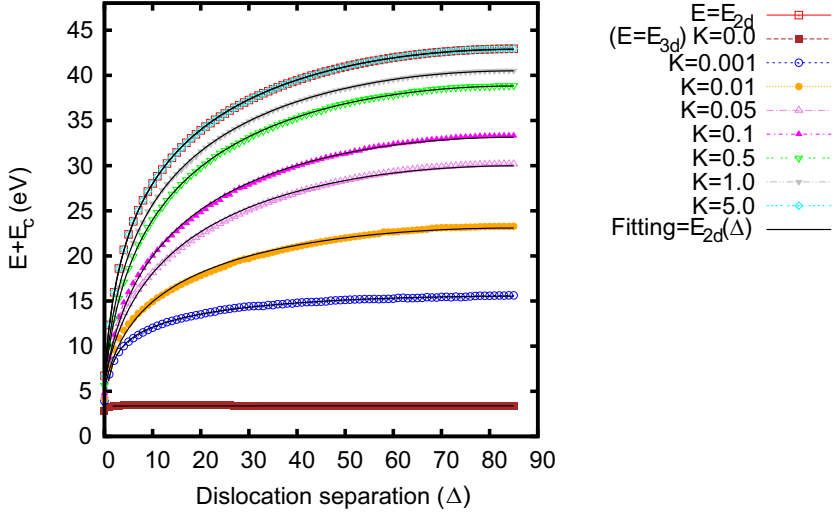


Figure 2.7: Energy ($E(\Delta)$) as a function of dislocation separation (Δ) in a 69200-atoms sample for different values of strengths K ($\text{eV } \text{\AA}^{-2}$) of the confining potential. Note that $K = 0$ (see eq. (2.9)) is for free standing graphene, while $K \rightarrow \infty$ is the limit to fully planar graphene. This figure shows that at any nonzero K , the energy diverges logarithmically, whereas for $K = 0$ (free standing graphene), the energy converges to a constant.

logarithmic behavior of the energy as a function of dislocation separation restores again with harmonic confinement.

The K value determines the lateral localization of the buckling. We have analyzed the lateral extension of the buckling at different values of K . At $K = 0.001 \text{ eV } \text{\AA}^{-2}$, the lateral extension of buckling is around 40 \AA , whereas this decreases to 20 \AA for $K = 0.01 \text{ eV } \text{\AA}^{-2}$ and 12 \AA for $K = 0.05 \text{ eV } \text{\AA}^{-2}$. Tison *et al.*²⁶ have shown that the buckling arising due to the grain boundaries extends to typically 5 to 20 \AA on SiC substrate. So, we estimate that a value of $K=0.001$ to $0.01 \text{ eV } \text{\AA}^{-2}$ is a reasonable estimate to simulate the presence of a substrate.

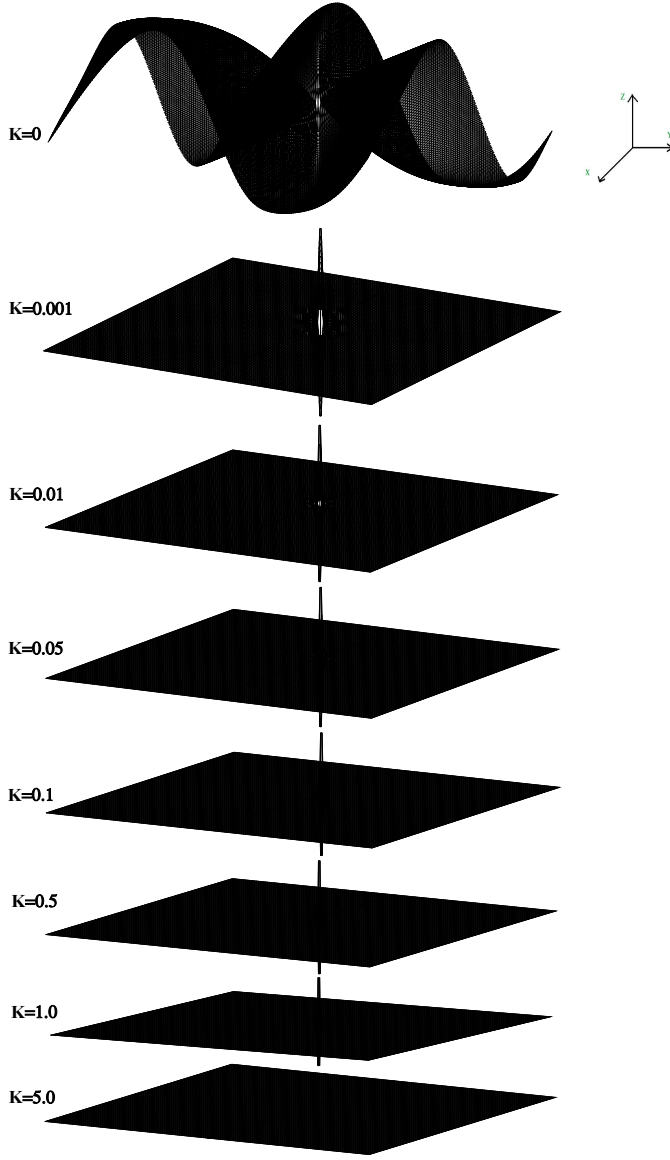


Figure 2.8: Out-of-plane structure of an SW defect, as a function of the strength K ($\text{eV } \text{\AA}^{-2}$) of the confining potential for a sample with 69200 atoms. Note that even a very small value of K already localizes the out-of-plane effect. Values of z -direction displacements are given in Table 2.3.

Table 2.3: Values of buckling height Δz_{max} in Å (difference between maximum and minimum z -direction co-ordinates) for different values of K (eV Å⁻²) (see eq. (2.9)) at different dislocation separation distances (Δ) for a sample with 69200 atoms.

Δ	$K = 0$	$= 0.001$	$= 0.01$	$= 0.05$	$= 0.1$	$= 0.5$	$= 1.0$	$= 5.0$
0	10.855	2.461	2.138	1.751	1.580	0.975	0.705	0.000
2	17.481	4.361	3.561	2.597	1.722	1.237	0.987	0.000
5	21.380	4.444	3.459	2.757	2.437	1.309	1.048	0.089
10	24.463	4.273	3.485	2.828	2.521	1.346	1.066	0.113
20	27.579	4.264	3.557	2.885	2.568	1.360	1.072	0.118
30	29.140	4.453	3.584	2.921	2.575	1.365	1.073	0.120
40	33.510	4.400	3.600	2.935	2.590	1.362	1.073	0.122
50	38.300	4.393	3.610	2.941	2.632	1.379	1.076	0.123
60	42.290	4.376	3.617	2.939	2.597	1.364	1.076	0.124
70	44.973	4.388	3.593	2.942	2.594	1.383	1.076	0.124
80	46.304	4.389	3.600	2.943	2.599	1.371	1.076	0.124
85	46.488	4.450	3.626	2.942	2.599	1.363	1.076	0.124

2.3.4 Grain boundaries (domains) in graphene

To demonstrate the broad applicability of our newly developed potential, we also simulate grain boundaries in graphene. To generate a sample, we start with a completely random 2D sample (all sites are 3-fold connected) and allow it to evolve doing WWW bond transpositions⁵⁵ with respect to time at room temperature.

The initial connectivity is generated as follows. We first generate a Voronoi diagram from the initial random configuration,¹³⁴ whereby the boundaries between each Voronoi point are defined by the crossing normals of the mid-point connected each Voronoi point to their nearest neighbors. This allows us to generate an unbiased isotropic 3-fold connected random network.

To generate a Voronoi network we start with $N/2$ random points in a square box and place 8 copies of this box around it to implement periodic boundary conditions. Then Voronoi vertices are identified and connected in order to make bonds in between them. Hence, a random sample having N atoms is generated.

Next, we use the improved bond-switching WWW-algorithm to evolve the system,⁵⁶ using our empirical potential to describe its energy. After each bond-switch the system is fully relaxed and the configuration is accepted with a

Metropolis probability given by

$$P = \min \left[1, \exp \left(\frac{E_b - E_f}{k_B T} \right) \right]. \quad (2.10)$$

Here E_b is the energy before the bond transposition and E_f is the energy after the bond transposition.

To study the energy behavior in time of a sample with $N = 1000$ atom, we stored the samples after every N bond transposition moves. For our study we defined the unit of time as N bond transposition moves, that is one attempted bond switching move per atom. The evolution of the grain boundaries in the 1000-atom sample is shown in Figure 2.9. These samples are completely flat. However, when small out-of-plane fluctuations are given, they start to buckle. Buckling caused by the grain boundaries has a long-range effect and the buckling height is also very significant (11.5 Å) for the sample at $t=100$. Figure 2.10 shows the evolution of the domains in the free-floating buckled graphene.

We study the energy evolution of domains in time for both flat (2D) and buckled modes (3D) in graphene. Our initial samples ($t=0$) are topologically the same for both 2D and 3D cases. Figure 2.11 compares the configuration energy evolution for the 2D and 3D cases (here energy data are averaged over five samples). In comparison to the 2D flat case of domains, the energy converges much earlier in the 3D buckled case. The initial ($t=0$) buckled sample has much lower energy than the initially flat case but the energy evolution is more significant and effective in 2D in comparison to 3D case. In the process of domain evolution, domain growth becomes very slow once the system can be characterized as crystalline domains separated by grain boundaries (GBs; chains/strings of 5- and 7-fold rings). This is in agreement with experiments by Kurasch *et al.*¹³⁵ and Rasool *et al.*²⁵ They show that continuous lines of pentagons and heptagons (GBs) are energetically stable. A review on the GBs in polycrystalline graphene by Yazyev *et al.*²⁴ is also in good agreement with our simulations (Figure 2.9).

The evolution of different kinds of rings during the domain growth is shown in the form of ring statistics plots for both flat and buckled cases (see Figure 2.12 and Figure 2.13 respectively). During the domain evolution the number of hexagonal rings increases whereas the number of pentagon, heptagon, and octagon rings decreases in order to achieve an energetically stable structure. Ring statistics is more or less the same for both the cases, but after 100 units of time the number of 6-fold rings is higher in 2D (compared to 3D), which we attribute to the fact that in 2D dislocations are attracting each other; hence, they come together and are annealed during the evolution process. At the end they form GBs which are energetically stable (which is also an experimental observation). In 3D, however, dislocations repel each other, and hence they

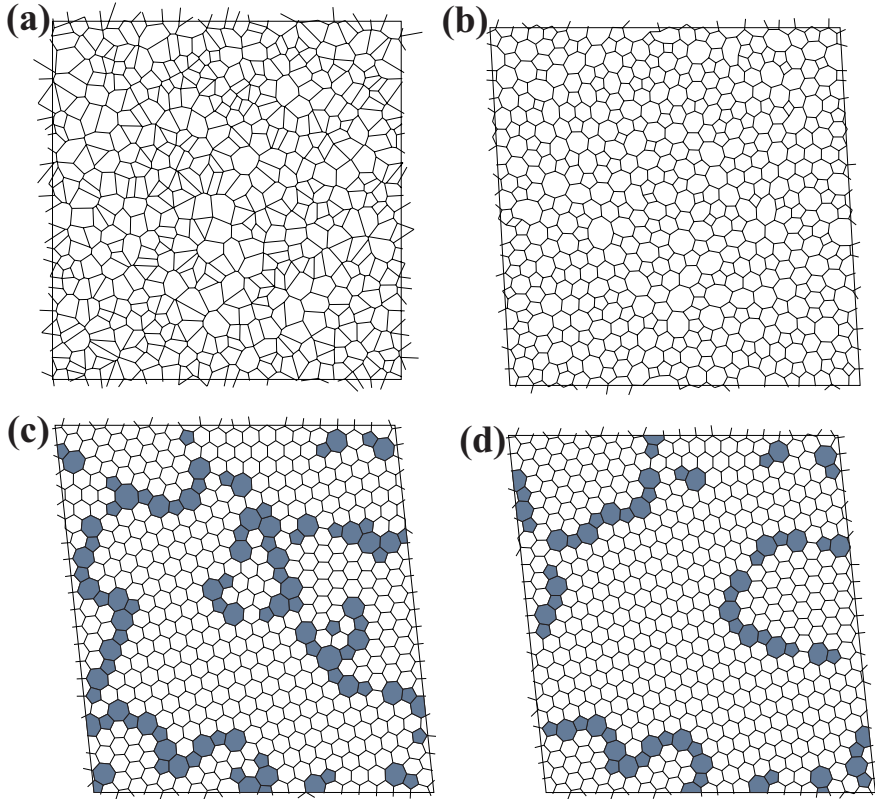


Figure 2.9: Structural evolution of a 1000-atom sample by bond transposition moves, confined to strictly planar configurations. (a) The starting sample: a random periodic Voronoi network which is unrelaxed. (b) Sample after minimization, and some minor manipulation to remove structural anomalies ($t=0$). (c) Sample having early evolved domains ($t=25$). (d) Sample having mature domains ($t=100$). The unit of time is N bond transposition moves.

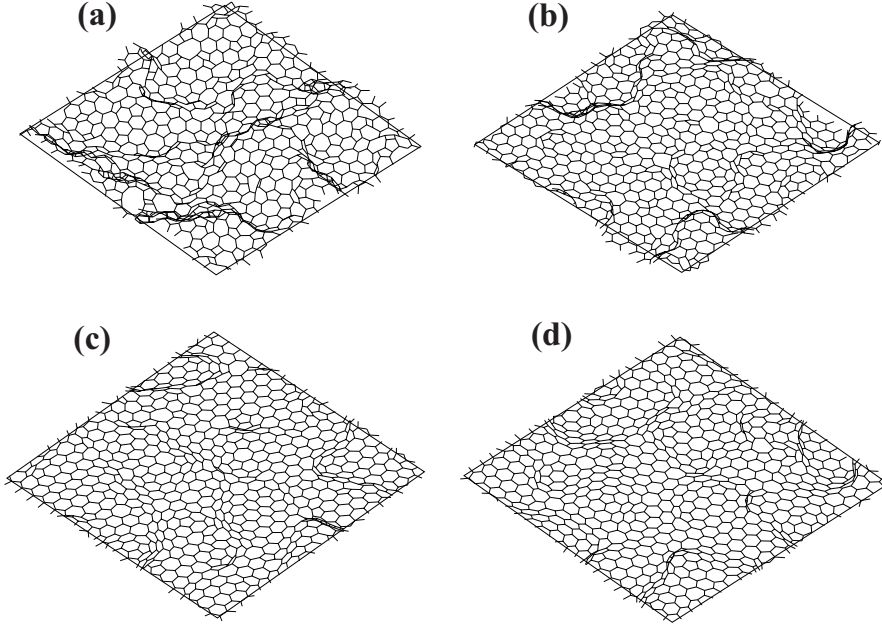


Figure 2.10: Structural evolution of a 1000-atom sample by bond transposition moves, with out-of-plane relaxation. (a) Starting sample, equal to that in Figure 2.9(b), but with random out-of-plane displacements (after which it is relaxed) ($t=0$). (b) Sample having early evolved domains ($t=5$). (c) Sample having more mature domains ($t=15$). (d) Sample with mature domains ($t=100$). Here, x and y dimensions are $50 \times 50 \text{ \AA}^2$ with bulging in z -direction up to $\pm 6 \text{ \AA}$. The unit of time is N bond transposition moves.

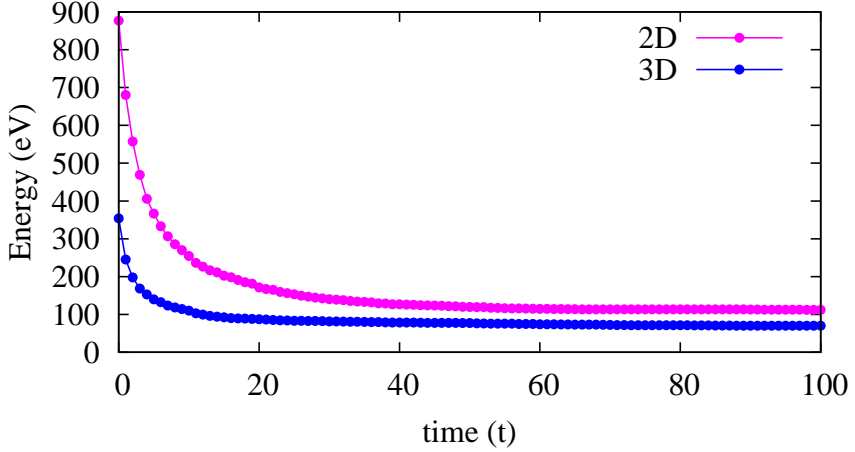


Figure 2.11: Energy as a function of evolution time for both the flat (planar) case and the buckled case (with out-of-plane relaxation).

do not come together to form long grain boundaries. We have analyzed the sample topology of the 3D relaxed sample after 100 units of time and found many disclinations (single pentagon or heptagons rings) and dislocations present in the sample.

To observe the effect of substrate on the domain evolution process we introduce the confinement energy term (eq. (2.9)) in the potential and minimized the buckled sample ($t=100$) for different values of K ($\text{eV } \text{\AA}^{-2}$). The buckling height decreases from 11.5 \AA for $K = 0 \text{ eV } \text{\AA}^{-2}$ to 7.7 \AA for $K = 0.001 \text{ eV } \text{\AA}^{-2}$, and it decreases further to 4.2 \AA for $K = 0.01 \text{ eV } \text{\AA}^{-2}$. In the recent paper by Tison *et al.*,²⁶ grain boundaries in graphene on a SiC substrate are analyzed in high resolution in three dimensions by means of scanning tunneling microscopy (STM). They find that maxima in height vary between 4 \AA and 8 \AA for different misorientation angles of GBs and that the buckling in lateral dimensions extends to typically $5\text{-}20 \text{ \AA}$. This experimentally determined height of the grain boundaries is in excellent agreement with the height of the buckling that we obtained at different values of K . Thus, we infer that reasonable values of K are in the range of $0.001\text{-}0.01 \text{ eV } \text{\AA}^{-2}$.

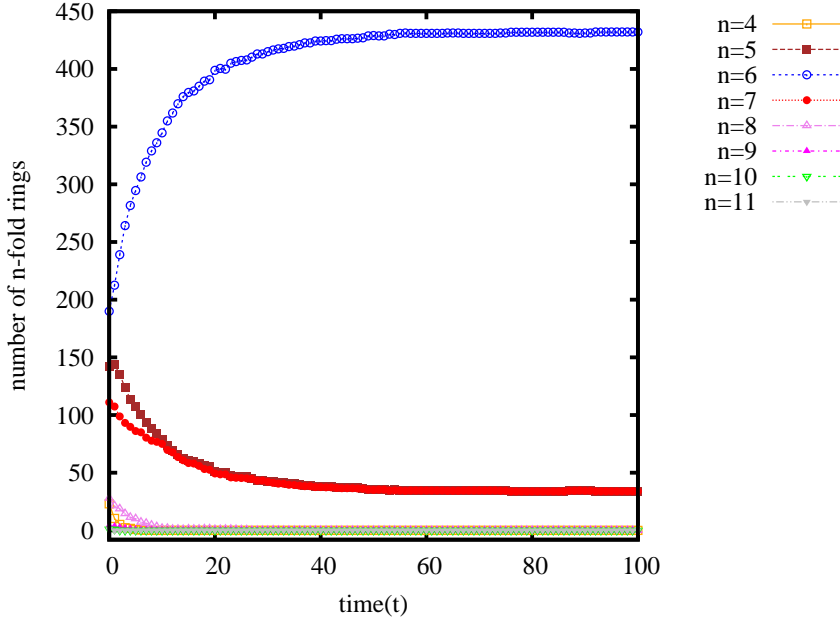


Figure 2.12: Ring statistics as a function of evolution time for the flat (planar) case.

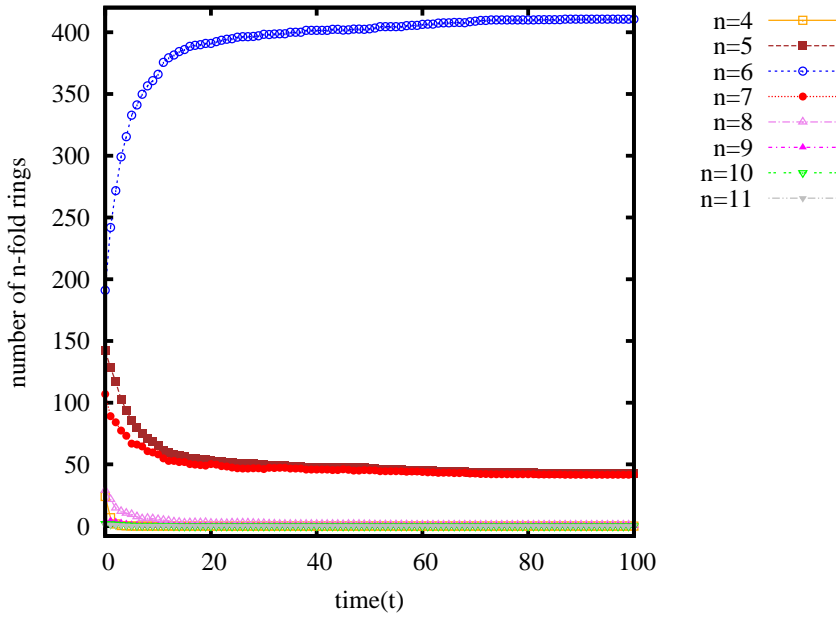


Figure 2.13: Ring statistics as a function of evolution time for the buckled case (with out-of-plane relaxation).

2.4 Conclusion

We have developed a novel potential which includes an out-of-plane buckling term which is optimized by DFT calculations. This extra term in the semiempirical potential is essential to simulate accurately buckling in graphene. This potential uses an explicit list of the bonds between the atoms and is therefore very cheap in terms of computational requirements. As this potential is an extension of the Kirkwood potential, bending and stretching have been completely separated without interference between them. The potential reproduces very well both the structural properties and the energies of defect-free graphene, defective graphene, and graphene containing well-defined point or reconstructed defects. Considering the defect energies, we have revealed that calculations which do not take long-range relaxations into account, which is typically the case in the literature, suffer from large systematic errors, since these relaxations can lower the formation energies even by a factor of 2 or 3. Although our potential cannot deal with extrinsic (dopant) atoms, this limitation could be overcome by a multi-method approach, where the local environment of dopant atoms is treated with e.g. DFT, while the long-range relaxations outside of this local environment are calculated using the novel semiempirical potential.

The current potential enables the accurate simulation of other defects as well, including line dislocations and grain boundaries. The experimentally well-known buckling and rippling of graphene is convincingly demonstrated for these defects. Without the out-of-plane component of the potential, these phenomena could not have been properly described. Furthermore, a long-standing paradox of the divergence in energy of a separating Stone-Wales defect has been solved: the out-of-plane energy contribution leads to stabilization of the energy at large separations.

In the future, the current potential could be used in simulations whereby interaction with supports, such as Ir(111) surfaces with steps at edges at the surface, can be simulated by hard interactions between the support and the graphene, whereas the typical buckling and rippling of the graphene can be simulated with the present potential. The current potential could also be modified for simulation of free edges in graphene, since free edges play a significant role in graphene or carbon nanotube morphologies.

Finally, we mention that the current approach can possibly be extended to the development of new potentials for other two-dimensional atomic crystals⁵⁹ such as h-BN, MoS₂, and WSe₂, so that long-range structural defects can be reliably simulated in these 2D materials as well.

2.5 Acknowledgments

We would like to thank Ingmar Swart and Vladimir Juricic for useful discussions.

PROBING CRYSTALLINITY OF GRAPHENE SAMPLES VIA VDOS

Abstract: The purity of graphene samples is of crucial importance for their experimental and practical use. In this regard, the detection of the defects is of direct relevance. Here, we show that structural defects in graphene samples give rise to clear signals in the vibrational density of states (VDOS) at specific peaks at high and low frequencies. These can be used as an independent probe of the defect density. In particular, we consider grain boundaries made of pentagon-heptagon pairs, and show that they lead to a shift of the characteristic vibrational D-mode toward higher frequency; this distinguishes these line defects from Stone-Wales point defects, which do not lead to such a shift. Our findings may be instrumental for the detection of structural lattice defects using experimental techniques that can directly measure VDOS, such as inelastic electron tunneling and inelastic neutron spectroscopy.

This chapter is based on "Probing crystallinity of graphene samples via the vibrational density of states" by S. K. Jain, V. Juricic G. T. Barkema, *J. Phys. Chem. Lett.*, 6:3897, 2015.

3.1 Introduction

The quality of the crystalline samples is very important for the observation of the hallmark features of graphene, such as ballistic conductivity,^{136,137} as well as for its mechanical and chemical properties, e.g., its permeability.¹³⁸ Large graphene samples produced, for instance, by chemical vapor-deposition (CVD), exfoliation or epitaxial growth on metal and SiC substrates are typically polycrystalline and thus contain intrinsic lattice defects, such as grain boundaries,^{24–26} dislocations and Stone-Wales (SW) defects, as well as extrinsic defects, e.g., adatoms.¹³⁹ Detection of the lattice defects is of both fundamental and practical relevance, since they are inevitably present in the graphene samples and can significantly alter the graphene’s chemical and physical properties.²³ In fact, the defects may not only be detrimental for the properties of graphene, but may also be interesting in their own right, as they may lead to some new effects, not present otherwise,^{140–142} and are also important for graphene nano-devices.¹⁴³

Structural defects are especially prominent in this regard.²³ In particular, graphene is a unique two-dimensional crystalline membrane that hosts lattice defects arising due to the flexibility of the carbon atoms in hybridization. As a result, polygons different from hexagons can appear in the lattice structure. Energetically favorable point-like defects of this type include the SW defect obtained when four hexagons are transformed by a bond transposition of 90° into two pentagon-heptagon pairs, thereby conserving the number of the atoms. They can be formed thermally in pristine graphene, but have a formation energy of ~ 5 eV, and thus pristine graphene may host only a few of them. On the other hand, such defects and similar ones can be frozen in during the annealing process and it is therefore not surprising that they have been experimentally observed.^{22,144,145} Moreover, there have been proposals for their controllable production in graphene.¹⁴⁰

Techniques to characterize the crystal structure of graphene include direct local ones, such as transmission electron microscopy (TEM), scanning tunneling microscopy (STM)²⁹ and atomic force microscopy (AFM),^{31,32} as well as the indirect ones, among which Raman spectroscopy,^{33–35} X-ray absorption spectroscopy,^{36–38} inelastic electron tunneling spectroscopy (IETS),^{39–41} and neutron scattering.^{42,43} Although widely used, Raman spectroscopy is limited by selection rules to only a certain number of Raman-active vibrational modes, which include the so-called G and 2D peaks located at 1580 cm^{-1} and 2680 cm^{-1} , respectively,¹⁴⁶ originating from the G and D phonon modes.¹⁴⁷ In the presence of disorder, due to the breaking of the lattice symmetry, the D mode at 1340

cm^{-1} , Raman inactive in pristine graphene, becomes active. Little is known about the specific experimentally observable signatures of the structural defects, such as point and line defects, in the vibrational spectrum. This is an important problem especially in light of the recent mapping of the entire vibrational spectrum of graphene by IETS,¹⁴⁸ and reported signature vibrational bands in CVD graphene with defects.³⁵

In this chapter, we show that the nature and density of structural point and line defects in graphene samples can be characterized by the specific and distinct features in the vibrational density of states (VDOS). These features are directly detectable in IETS and neutron scattering, which are not limited by selection rules, as opposed to the Raman spectroscopy, and can thus probe the entire vibrational spectrum.¹⁴⁸ Specifically, using a recently developed effective semiempirical elastic potential¹⁴⁹ we show that the presence of the point-like SW defects in pristine flat graphene gives rise to a simultaneous decrease in the VDOS of the peaks corresponding to high-frequency D and F modes (Figures 3.1(a) and 3.2(a)). More importantly, the graphene membrane has a natural tendency to buckle, and as a result new low-energy vibrational states appear, with particularly pronounced L and L' peaks (Figure 3.1(a)). When the SW defects are introduced, the intensities of these characteristic modes simultaneously decrease, and the peak positions shift toward higher values of frequency (blue shift), see Figure 3.3(b). On the other hand, we find that line defects give rise to a blue shift of the D peak in conjunction with the decrease of its intensity. The substrate plays an important role in the production of graphene samples,^{150, 151} and we therefore show that the decrease in the VDOS of low-frequency modes without any shift signals its presence.

3.2 Method

To calculate the vibrational spectrum of graphene, we use a potential described in Chapter 2, eq. (2.2).¹⁴⁹ Additionally, the effect of the substrate to the buckled graphene sample is described by an extra harmonic term given in Chapter 2, eq. (2.9).¹⁴⁹ The VDOS represents the number of modes at a certain frequency, and the total area under the VDOS gives the total number of vibrational modes, which is $2N$ for a flat and $3N$ for a buckled graphene sheet, with N the total number of atoms in the sample. In our plots, the VDOS is convoluted with a gaussian function with a width of $\sigma = 14 \text{ cm}^{-1}$, and $N = 680$; this is much larger than system sizes in previous *ab initio* studies of pristine graphene and graphene with defects.^{47, 117, 152, 153} Furthermore, we have computed the relative

decrease of the number of modes corresponding to the characteristic bands as a function of the defect density. We have performed this computation by counting the number of modes with a VDOS greater than a certain fixed value selected by the symmetry of the characteristic peak, see Figures 3.2(d) and 3.3(e).

3.3 Results and discussion

Here, we firstly present the reference VDOS for flat and buckled graphene and discuss the various prominent peaks and their corresponding displacement profiles. Later on we systematically present the effect of defects (both point and line-defects) on the positions of peaks in VDOS. We also discuss the effect of substrate on VDOS of graphene.

3.3.1 Pristine flat and buckled graphene sheets

We first calculate the VDOS for a flat pristine graphene sample, which serves as the reference spectrum in the following. The plot displayed in Figure 3.1(a) shows the characteristic peaks that correspond to D and G vibrational bands, of which only the latter is Raman active.¹⁴⁷ The corresponding modes, shown in Figure 3.1(b) and 3.1(c) transform under E_{2g} and A_{1g} representations of the graphene's D_{6h} point group symmetry, respectively.¹⁵⁴ Notice that the hallmark feature of the monolayer graphene, the Raman-active G mode, which is at the maximum frequency in the vibrational spectrum, see Figure 3.1(a), is positioned at $f_G \simeq 2080 \text{ cm}^{-1}$, and therefore offset by about 25% as compared to the experimentally measured value of $\sim 1580 \text{ cm}^{-1}$. The D mode at $f_D \simeq 1660 \text{ cm}^{-1}$ is also shifted by about 25% compared to the experimentally measured 1340 cm^{-1} . Deviations of this magnitude are expected since the parameters of the effective potential are obtained from DFT¹⁴⁹ with similar deviations. However, the form of the displacements of these modes, shown in Figures 3.1(b) and 3.1(c), allows us to identify them as G and D modes, respectively. Furthermore, the vibrational spectrum of graphene features the F mode, shown in Figure 3.1(d), at $f_F \simeq 1280 \text{ cm}^{-1}$. A flat graphene sheet has a natural tendency to buckle, and this leads to the appearance of additional soft out-of-plane phonon modes in the range of frequencies approximately up to $f_{3D} \sim 300 \text{ cm}^{-1}$, which is of the order of the energy scale corresponding to the parameter γ describing the buckling in the effective potential (2.2), $f^\gamma \sim (1/2\pi c)\sqrt{\gamma/m_C} \simeq 150 \text{ cm}^{-1}$, with

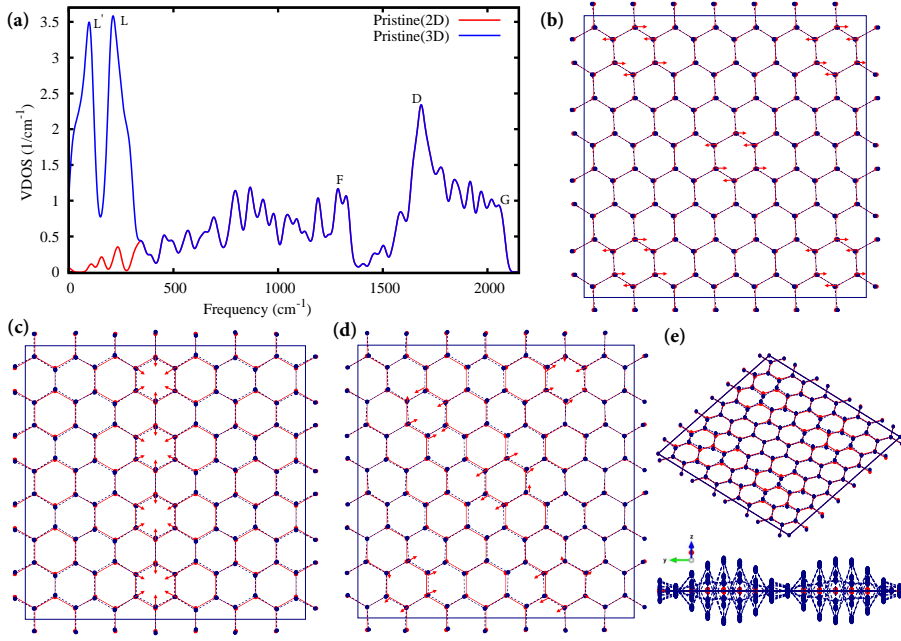


Figure 3.1: VDOS and the profile of the displacements of the prominent modes in pristine graphene. (a) VDOS of both flat and buckled pristine graphene. (b) Vibrational mode corresponding to Raman active G mode at 2080 cm^{-1} . (c) D mode at 1660 cm^{-1} . (d) F mode at 1280 cm^{-1} . (e) Out-of-plane L mode at 210 cm^{-1} : displacements in the flat graphene's ($x - y$) plane (top) and in the side $y - z$ plane (bottom).

$m_C \simeq 2 \times 10^{-26} \text{ kg}$ as the atomic mass of carbon, and $c = 3 \times 10^8 \text{ m/s}$ the velocity of light. The L and L' modes, the former being a B_{2g} mode (Figure 3.1(e)), at frequency $f_L \simeq 210 \text{ cm}^{-1}$ and $f_{L'} \simeq 100 \text{ cm}^{-1}$, respectively, are especially prominent and, as we show, can be used to probe the point defects in the buckled graphene samples.

3.3.2

Point SW defects in flat and buckled graphene samples

We now study the VDOS in flat graphene with point-like SW defects, see Figure 3.2(b). The obtained VDOS is displayed in Figure 3.2(a). We first observe that significant changes in the VDOS occur in the high-frequency region, at frequencies above 500 cm^{-1} . As the density of the defects increases, the VDOS at the peaks decreases. On the other hand, the VDOS at the minima increases, as

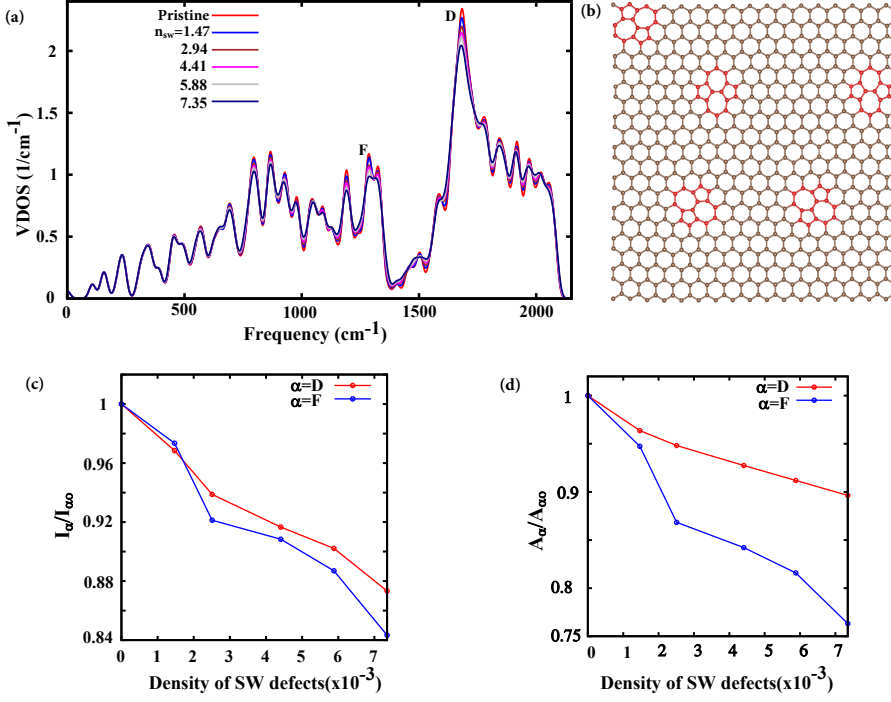


Figure 3.2: Structure of a flat graphene sample having multiple point SW defects and corresponding VDOS. (a) VDOS of flat graphene samples with different densities of SW defects $n_{SW}(\times 10^{-3})$. (b) The flat graphene sample with five SW defects. (c) Relative decrease in the intensity of D and F peaks at different defect densities. (d) Relative decrease in the number of modes of D and F bands at different defect densities in the range of frequencies in which VDOS is greater than $1.5/\text{cm}^{-1}$ and $1.0/\text{cm}^{-1}$, respectively.

a consequence of the conservation of the total number of the vibrational modes. Notice in particular that the height of both D and F peaks simultaneously decreases as more and more defects are added to the sample, see Figure 3.2(c). Particularly, for the highest defect concentration considered, $n_{SW} \simeq 0.7\%$, the VDOS decreases by about 12% and 15% for the D and F modes, respectively. This simultaneous decrease of the two peaks in the VDOS represents a hallmark feature of the presence of point defects in the flat graphene sheet, and is certainly experimentally observable. Furthermore, we have found a relative decrease in the number of modes for D and F band of $\sim 10\%$ and $\sim 25\%$, respectively, see Figure 3.2(d).

The SW defects in the buckled graphene sheet (Figure 3.3(a)) have a drastic effect on the low-frequency L and L' vibrational bands. Their presence gives rise

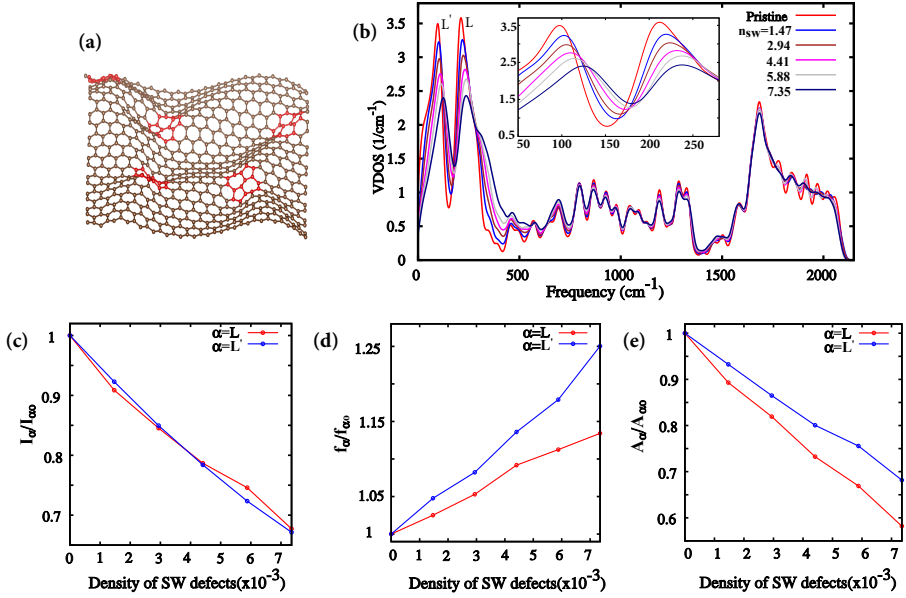


Figure 3.3: Structure of a buckled graphene sample having multiple point SW defects and corresponding VDOS. (a) The lattice structure of a buckled graphene sample with five SW defects. (b) VDOS of buckled graphene samples with different densities of SW defects $n_{SW}(\times 10^{-3})$. Inset: Low-frequency peaks in VDOS zoomed in. (c) Relative decrease in the intensity of L and L' modes at different n_{SW} . (d) Relative increase (blue shift) in the frequency of L and L' modes at different n_{SW} . (e) Relative decrease in the number of modes of L and L' bands at different defect densities in the range of frequencies in which VDOS is greater than $1.9/\text{cm}^{-1}$ and $1.5/\text{cm}^{-1}$, respectively.

to the simultaneous decrease of the corresponding peaks in the VDOS, together with the increase of the mode corresponding to the minimum between the two maxima in the VDOS, as shown in Figure 3.3(b). The decrease in the VDOS of the two peaks is proportional to the defect concentration (Figure 3.3(c)), and it appears to be significant. For instance, for the defect concentration of $n_{SW} \simeq 0.7\%$ it is of the order of 30%. Furthermore, this decrease occurs in conjunction with a systematic blue shift of the maximum of the two modes as the density of the defects increases, see Figure 3.3(d). In particular, for the defect density $n_{SW} \sim 0.7\%$, it is of the order of 25% and 15% for L' and L mode, respectively. Finally, we find a significant relative decrease in the number of modes as a function of the defect density, which is $\sim 40\%$ and $\sim 30\%$ for the L and L' bands, respectively, see Figure 3.3(e).

3.3.3 Signatures of the domains and the substrate in the VDOS

We now turn to the effects of the grain boundary (Figure 3.4(a)) to the vibrational modes in flat graphene. As can be seen in Figure 3.4(b), the most prominent features in the VDOS are visible in the high-frequency region. In particular, the intensity of both the F and D bands decreases by approximately 35%, followed by the simultaneous blue shift of both bands by about 2%. These effects should be contrasted to the behavior of the VDOS in the presence of the point-like SW defects, where no such a shift occurs either in confined two-dimensional geometry or in buckled samples. This blue shift may be attributed to the fact that due to the presence of the defects, the atomic bonds become shorter and therefore stiffer at the position of the defects. The corresponding modes thus become shifted to higher frequencies as compared to the defect-free sample. Notice that this effect is negligible in the case of the confined graphene sample because the relative change of the parameter α in the effective potential (2.2) is very small, less than 1%. In a buckled sample, on the other hand, due to the fact that the out-of-plane modes are soft, this change is much larger, $\sim 20\%$, and therefore leads to the obtained more pronounced effect, see the inset of Figure 3.3(b). Finally, we consider the effect of the substrate described by the term (2.9) in the effective potential. We plot the VDOS for several values of the parameter K in Figure 3.4(c), and observe that the intensity of the low-frequency L and L' peaks decreases by about 5% (see inset of Figure 3.4(c)), without any shift in the position, which is yet different from point defects where such a decrease is followed by the blue shift of the peaks. Notice that this suppression of the intensity of the L and L' peaks due to the confinement by the substrate is in qualitative agreement with the experimentally observed low-intensity out-of-plane phonon modes in backgated graphene samples placed on a substrate.¹⁴⁸ Although the harmonic confinement potential (2.9) is certainly a crude description of the real interaction, it may be improved to also accurately capture the quantitative features of the experimentally observed VDOS spectrum.

3.4 Conclusion

To conclude, we have shown that the VDOS can be used as a tool to detect the presence of point and line defects in graphene sheets. The confined two-dimensional graphene sample in the presence of the defects shows clear features

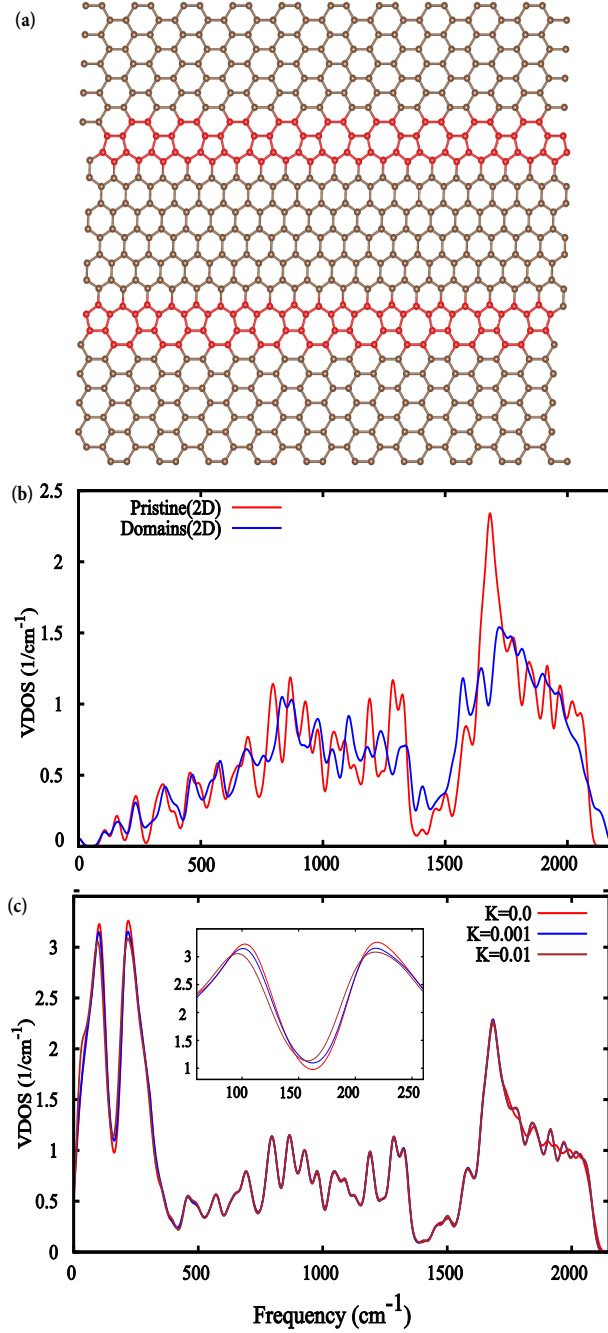


Figure 3.4: Signature of the line defect and substrate in the VDOS. (a) A graphene sample with two differently oriented domains, with angular mismatch of 30° separated by straight lines of alternating pentagon and heptagon rings. (b) Comparison of the VDOS of pristine graphene and graphene with grain boundaries. (c) VDOS of a graphene sample having one SW defect interfaced by a substrate, with the confining potential given by eq. (2.9), and with the parameter K in $\text{eV}/\text{\AA}^2$. Inset: Low-frequency part of VDOS with the prominent L and L' peaks.

in the high-frequency VDOS, while the most pronounced effects of the buckling appear at low frequencies. Given the recent measurement of the entire vibrational spectrum of backgated graphene placed on a substrate using IETS,¹⁴⁸ we hope that our findings will stimulate further experiments to probe the structural defects in this material. Our results can also be used to calculate the corresponding Raman response using different models.^{155,156} We would like to point out that our findings may also be applicable to other two-dimensional materials that could be described by a semiempirical potential of the form (2.2), such as nanoporous carbon.^{157,158} We hope that these results will stimulate further studies of vibrational properties of other carbon-based nanomaterials such as carbon-nanotubes,^{159,160} graphene nano-ribbons,¹⁶¹ and functionalized graphene.¹⁶²

3.5

Acknowledgments ---

We would like to thank Ingmar Swart and Rembert Duine for useful discussions.

BOUNDARIES DETERMINE THE FORMATION ENERGIES OF LATTICE DEFECTS IN TWO-DIMENSIONAL BUCKLED MATERIALS

Abstract: Lattice defects are inevitably present in two-dimensional materials, with direct implications on their physical and chemical properties. We show that the formation energy of a lattice defect in buckled two-dimensional crystals is not uniquely defined as it takes different values for different boundary conditions even in the thermodynamic limit, as opposed to their perfectly planar counterparts. Also, the approach to the thermodynamic limit follows a different scaling: inversely proportional to the logarithm of the system size for buckled materials, rather than the usual power-law approach. In graphene samples of ~ 1000 atoms, different boundary conditions can cause differences exceeding 10 eV. Besides presenting numerical evidence in simulations, we show that the universal features in this behavior can be understood with simple bead-spring models. Fundamentally, our findings imply that it is necessary to specify the boundary conditions for the energy of the lattice defects in the buckled two-dimensional crystals to be uniquely defined, and this may explain the lack of agreement in the reported values of formation energies in graphene. We argue that boundary conditions may also have an impact on other physical observables such as the melting temperature.

This chapter is based on "Boundaries determine the formation energies of lattice defects in two-dimensional buckled materials" by S. K. Jain, V. Juricic G. T. Barkema, *Phys. Rev. B*, 94:020102(R), 2016.

4.1 Introduction

Lattice irregularities in the form of defects, such as dislocations and grain boundaries, are quite generically present in crystalline lattices. Usually, defects have a direct impact on the various properties of the material; for instance, in graphene they reduce the mobility,¹⁶³ change Young's modulus^{164,165} and the fracture behavior.¹⁶⁶ A fundamental property characterizing a lattice defect is its formation energy, with the crucial importance for their behavior, e.g. the defects' migration and healing.¹⁶⁷ On the other hand, two-dimensional crystals have a natural tendency to buckle out of the crystalline plane to relieve the stress.^{20,23,114} For perfectly confined two-dimensional materials, the formation energy of a lattice defect does not depend on the boundary conditions, but only on the type of the defect, and in that sense is uniquely defined. However, the question arises whether this fundamentally important feature of the lattice defects changes in buckled crystals, and in particular whether the boundaries affect the defects' energy.

In this chapter, we show that this is indeed the case by studying the formation energy of the defects in both simple, analytically tractable buckled one- and two-dimensional bead-spring models, as well as in numerical simulations of graphene, a paradigmatic representative of a two-dimensional buckled crystal. In particular, we find that unlike two-, and three- dimensional materials where the formation energy of a lattice defect, such as an SW defect, is well defined, in buckled two-dimensional materials different boundary conditions give rise to different values of the formation energy of the defect in the thermodynamic limit. Moreover, while the finite-size correction in the energy scales as inversely proportional to the system size for one-, two-, and three-dimensional materials, we show that this scaling for buckled sheet-type materials is given by the inverse of logarithm of the system size.

4.2 Method

To calculate the formation energies of defects in graphene, we use a recently developed semiempirical potential described in Chapter 2, eq. (2.2).¹⁴⁹

To prepare the graphene samples, first a supercell with periodicity vectors \vec{L}_x and \vec{L}_y is created, in which N carbon atoms are placed according to the crystalline

graphene structure. The defects are then introduced in this crystalline sample, after which the atomic positions are relaxed, i.e. the energy is minimized with the effective potential (2.2). In the case of deformation free (DF) boundary conditions, the periodicity vectors are kept fixed, while in the case of force free (FF) boundaries, these vectors are allowed to adjust (their lengths as well as the angle between them) in order to minimize the total energy. Allowing the periodicity vectors to relax (FF-boundary conditions) lowers the energy. Therefore, the formation energy with FF boundaries will always be lower than with DF boundaries.

4.3 Results and discussion

Here, we firstly present (1+1)-dimensional [(1+1)D] and (2+1)-dimensional [(2+1)D] bead-spring models. We systematically demonstrate the behavior of the formation energy of a lattice defect for two different boundary conditions both by numerically and analytically. Furthermore, we describe the scaling behavior of the formation energy of defects (SW and dislocations) in both flat and buckled graphene for both DF and FF boundary conditions.

4.3.1 Effective (1+1)D and (2+1)D models

To describe the boundary effect on the formation energy of the defects in buckled crystals, we first consider a simple model of a string of N atoms with length $L = N$, connected with elastic springs and a defect created at the center of the string by making the bond angle with the y -axis equal to $\theta \neq 0$, Figure 4.1(a). This string is embedded in two-dimensional space and in this way we allow for the buckling in the model. In this (1+1)D model, the energy of the defect configuration is minimized for the two most commonly used boundary conditions: force-free boundaries which relax the global planar stress, and deformation-free boundaries which fix the density of the atoms to the crystalline density, Figure 4.1(a). We use the Hamiltonian

$$H = E_{core} + \lambda \sum_i (r_i - 1)^2 + \kappa \sum_i (\phi_{i+1} - \phi_i)^2 - f \left(\sum_i r_i \cos(\phi_i) - L \right), \quad (4.1)$$

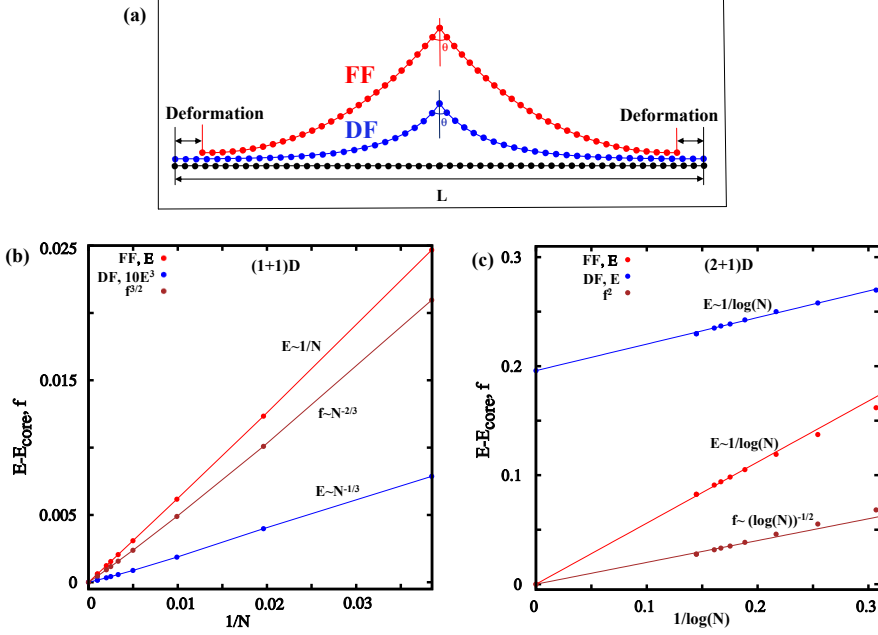


Figure 4.1: Illustration of force-free (FF) and deformation-free (DF) boundaries and calculated defect energy as a function of the system size for both (1+1)D and (2+1)D models. (a) Sketch of the elastic string model that accounts for the boundary effects on the formation energy of the defects. In the case of DF boundaries, the introduction of the defect does not change the total length (L) since a force is acting on the boundaries to keep the sample at constant density. In the case of FF boundaries, the density of the sample does change through the change of the length. (b) Finite-size correction to the energy and force for both the FF and DF boundaries in the (1+1)D model. The numerical data points are fitted well by the analytically predicted scaling of the energy for DF (blue line) and FF (red line) boundaries and force (brown line). (c) Finite-size correction to the energy and force for both the FF and DF boundaries in the (2+1)D model. The numerical data points are fitted well by the analytically predicted scaling of the energy for DF (blue line) and FF (red line) boundaries and square of the force (brown line). Here, we use the values of the parameters in the Hamiltonian (4.1), $\lambda = \kappa = 1$.

where r_i is the bond length between two neighboring atoms $i-1$ and i , and ϕ_i is the angle of this bond with respect to the x -axis. For simplicity, we set the core energy of defect $E_{core} = 0$. The elastic constants in the Hamiltonian are defined as follows: λ is the bond stretching constant, κ is the bond bending constant, and f is the force acting on the boundaries. At the FF boundary condition the energy is minimized for $r_i = 1$ and $\phi_i = \phi_0(-1 + \frac{i}{N})$, which leads to the finite-size energy scaling of $\sim 1/N$. In Figure 4.1(b) numerical values of FF energy calculations are shown (points) and are in a very good agreement with the analytical solution (fitted with line). Furthermore, DF boundary conditions yield a minimum energy for $r_i = 1 + f/(2\lambda)$ and $\phi_i = \phi_0 \exp(-\alpha i)$ with $\alpha = \sqrt{fr_i/2\kappa}$. These solutions in turn yield forces with finite-size scaling of the form $f \sim N^{-2/3}$ while the energy scales as $E \sim N^{-1/3}$. We have also performed the numerical simulations for DF boundary conditions, and these results are in agreement with the analytical ones (Figure 4.1(b)). More importantly, this very simple model already yields a different scaling of the energy with the system size for different boundaries, a feature also prominent in the (2+1)D model, which we consider next.

To obtain the defect formation energy and its dependence on the system size in two-dimensional space, we extended the one-dimensional model in two dimensions in a rotationally-symmetric manner. We analytically solve the (2+1)D model, as shown in the Appendix-(2+1)D model, and find that for FF boundary conditions the energy scales as $\sim 1/\log(N)$ with system size. Furthermore, at DF boundary conditions, the force scales as $f \sim 1/\sqrt{\log(N)}$ whereas the energy scales as $E \sim 1/\log(N)$ with a constant offset, which is the formation energy of the defect in the thermodynamic limit. In Figure 4.1(c), we show the numerical calculations of both the energy and force within this simple model. The data points are fitted with analytical predictions, and show very good agreement. The most striking result here is that both boundary conditions yield finite-size corrections of the form $1/\log(N)$, on top of a constant offset. In the limit of infinite system size, FF and DF boundaries therefore yield different formation energies. This very simple model captures an essential feature of the formation energy of a lattice defect in a buckled two-dimensional crystal, which is its dependence on the boundary conditions. Furthermore, the same model also produces the finite-size scaling of the energy as found in our computer simulations on graphene, which we present next.

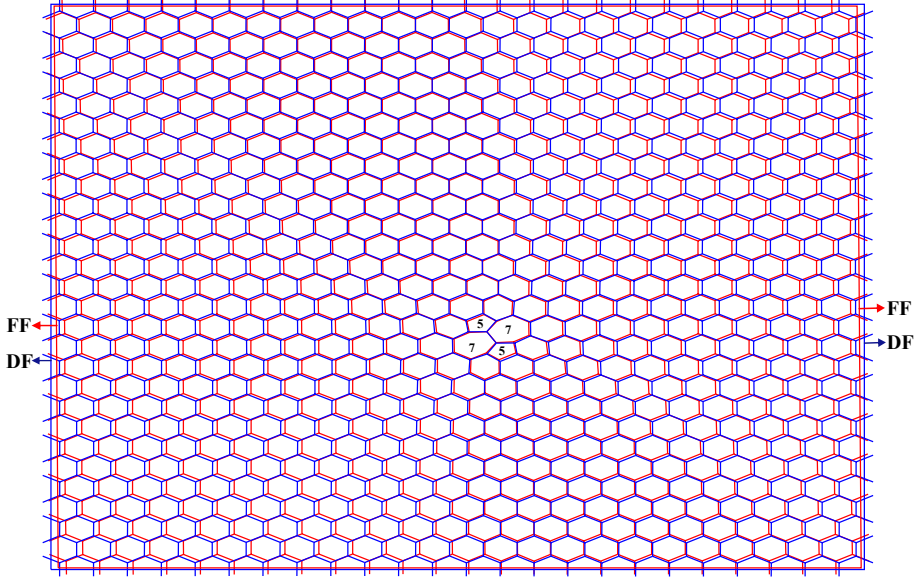


Figure 4.2: Top view of a buckled 1344-atom graphene sample with a single SW defect, minimized with DF (blue) and FF (red) boundary conditions.

4.3.2 Energetics of SW defect in graphene

The structural differences between DF and FF boundaries are shown in Figure 4.2 for a 1344-atom sample with a single Stone-Wales defect. To further demonstrate the effect of boundaries, we numerically study the formation energy of a single SW defect, made of a pair of pentagon-heptagon rings obtained when four hexagons are transformed by a bond transposition of 90° , in a graphene sheet buckled in the out-of-plane direction, as shown in Figure 4.3. We consider FF and DF boundary conditions, both of which are periodic as commonly used in simulations. Our results show that with DF boundaries the formation energy for the SW defects is always significantly higher than with FF boundaries, and such boundaries therefore strongly favor defect-free configurations of buckled graphene samples. Contrary to the natural intuition, the energy difference persists in the thermodynamic (infinite size) limit, as shown in Figure 4.4, even though all individual atomic positions become indistinguishable between the two types of boundaries. Finite-size effects remain even in very large samples, since the finite-size corrections in the energy decrease inversely proportional

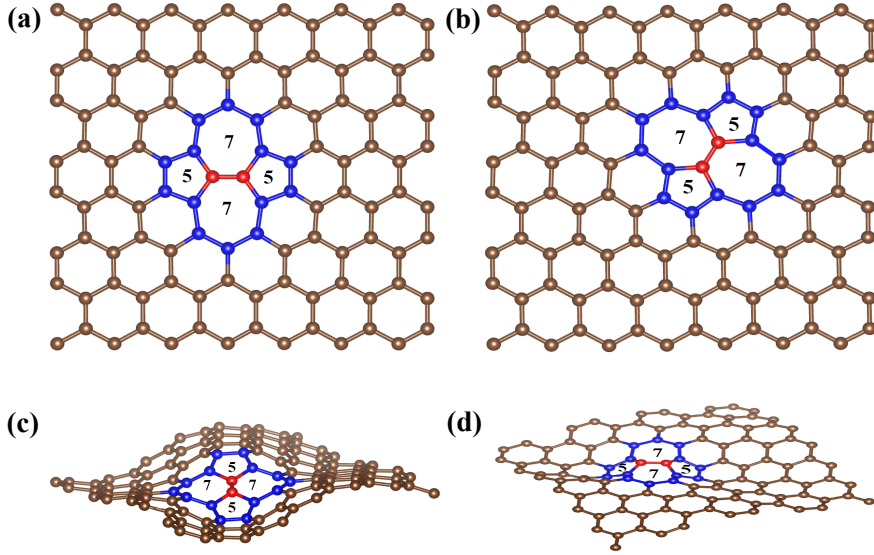


Figure 4.3: Structure of the graphene sample with a single SW defect. The two different orientations of the defect are shown: (a) 0° and (b) 60° . Two different buckling modes represent (c) sine-type buckling and (d) cosine-type buckling. The two configurations are shown from different viewing angles.

to the logarithm of the system size. In contrast, if all atoms are confined to a purely two-dimensional plane, both FF and DF boundaries quickly converge to the same formation energy which is much higher than in the buckled samples. Finite-size corrections in this case decrease much faster, inversely proportional to the system size. Apparently, buckling introduces strong finite-size effects, with boundary effects that do not vanish in the thermodynamic limit. Our results therefore imply that both the formation energy of the lattice defects and its dependence on the size of the buckled graphene samples are not well defined without specifying the boundary conditions, counter to the conventional wisdom.¹⁶⁷

Eight different geometries were used in our simulations to study the formation energy of an SW defect in graphene. They differ in the orientation of the SW defect relative to the boundaries (0° and 60°), the buckling modes (sine and cosine), and the types of boundaries (DF and FF). The two inequivalent initial bonds give rise to the two SW defects oriented by 60° relative to each other (Figure 4.3(a) and (b)). The system is then relaxed and to relieve the stress it buckles perpendicularly to the flat graphene plane with the two possible buckling

4. Boundaries determine the formation energies of lattice defects in two-dimensional buckled materials

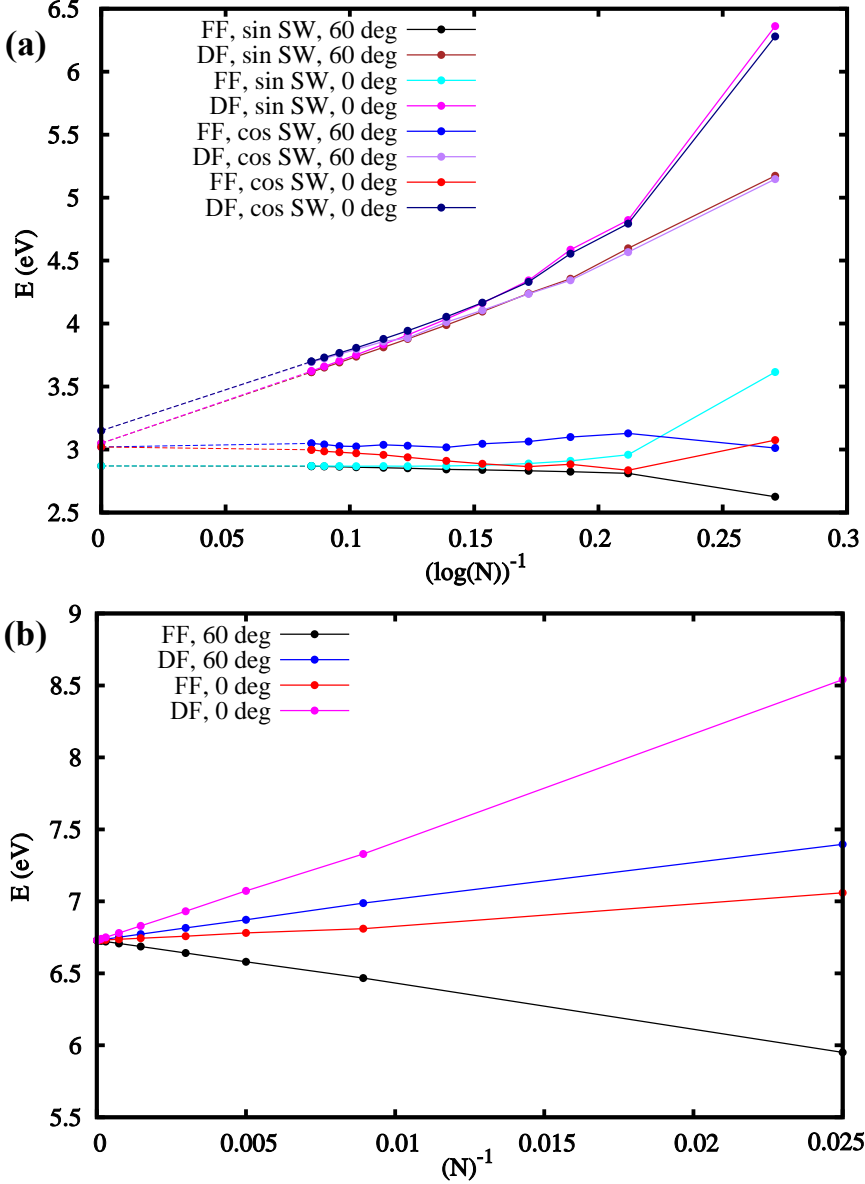


Figure 4.4: Formation energy as a function of the graphene sample size with a single SW defect for both buckled (sine and cosine) and flat configurations, with different boundaries (DF and FF) and defect orientations (0° and 60°). (a) In buckled graphene, the formation energy of the SW defect converges to four different values, determined by the boundary condition and buckling mode; different orientations do not influence the formation energy in the thermodynamic limit. Finite-size corrections scale as $1/\log(N)$, with different prefactors for different boundaries, buckling modes, and defect orientations. (b) In flat graphene, the formation energy of the SW defect converges to the same value (6.73 eV) irrespective of the orientation or the boundary condition, with finite-size corrections scaling as $1/N$.

Defect and boundary type	E_0 (eV)	$F(N)$
FF, sin SW, 60 deg	2.87	$1/\sqrt{N}$ *
DF, sin SW, 60 deg	3.05	$1/\log(N)$
FF, sin SW, 0 deg	2.87	$1/\sqrt{N}$ *
DF, sin SW, 0 deg	3.05	$1/\log(N)$
FF, cos SW, 60 deg	3.02	$1/\sqrt{N}$ *
DF, cos SW, 60 deg	3.15	$1/\log(N)$
FF, cos SW, 0 deg	3.02	$1/\sqrt{N}$ *
DF, cos SW, 0 deg	3.15	$1/\log(N)$

Table 4.1: Formation energy E_0 of an SW defect in graphene in the thermodynamic limit, and form of the corresponding leading finite-size corrections for different orientations, (0° or 60° with respect to the periodic directions, see Figure 4.3(a),(b)), different buckling (sine or cosine, see Figure 4.3(c),(d)), and different boundaries (FF or DF). Note that E_0 does not depend on defect orientation, but does depend on the buckling mode as well as on the type of boundary conditions. The leading finite-size correction in the formation energy scales as $1/\log(N)$, with varying amplitude. The lowest formation energy (2.87 eV) is for the configuration with FF boundaries and sine-type buckling, whereas the highest (3.15 eV) is for the DF boundaries with cosine-type buckling. Most importantly, the formation energies in the thermodynamic limit for DF and FF boundaries differ by 0.18 eV for sine-type buckling.

* In the case of FF boundaries, finite-size corrections for sample sizes studied here (up to 137616 atoms) are dominated by the scaling factor of $1/\sqrt{N}$,¹⁴⁹ but a correction $\sim 1/\log(N)$ with a small prefactor cannot be excluded.

configurations, sine and cosine, Figure 4.3(c) and (d), while the density of carbon atoms is kept fixed (DF) and relaxed (FF) [only FF shown in Figure 4.3].

The calculated formation energies of a single SW defect in a buckled graphene sheet for different system sizes are shown in Figure 4.4. Its scaling with the system size is given by

$$E_{\text{SW}}(N) = E_0 + F(N), \quad (4.2)$$

where E_0 is the energy contribution of the defect in an infinite (square) system, and $F(N)$ describes finite size corrections, with lateral sample size L and a number of carbon atoms $N \sim L^2$. We first observe for the eight structures that extrapolation to the infinite system size produces four different values for the formation energy E_0 of the defect; the dependence on the orientation of the defect vanishes, in agreement with the intuitive expectation based on the equivalence of the sp^2 carbon bonds. On the other hand, the defect energy depends on both the buckling configuration, and most notably, on the type of the boundary of the sample. In particular, the DF boundaries, in which the density of the carbon atoms is fixed to the crystalline value, always give a higher formation energy of the defect than FF boundaries, (see Table 4.1). Therefore, boundary conditions play a crucial role in determining the formation energy of

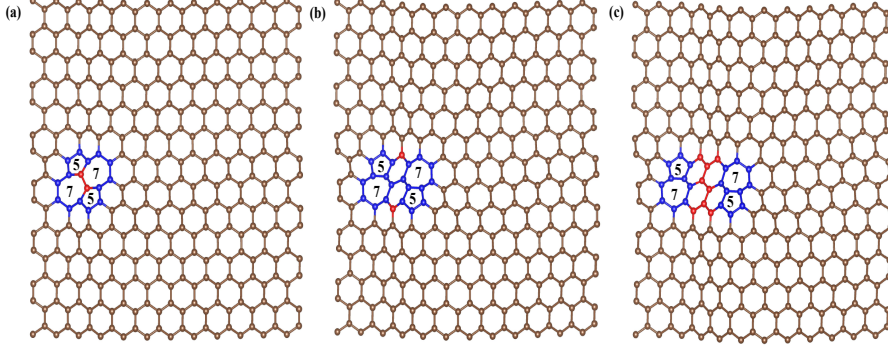


Figure 4.5: Separation of the dislocations (pentagon-hexagon pairs) by the introduction of Δ hexagon rings in between them. (a)-(c) Dislocation separation varies from $\Delta = 0$ to 2.

the defects.

This effect is especially pronounced when taking into account the finite size of the graphene samples. As shown in Figure 4.4(a), there is a notable difference in the formation energy of the SW defects of up to 30% between the samples with DF and FF boundaries at the size of $N \sim 10^4$ atoms. More importantly, the finite-size correction to the defect energy, $F(N)$, scales as $1/\log N$ for DF boundaries. Therefore, DF boundaries besides giving higher formation energy of the defects in the thermodynamic limit, also give rise to its slow decrease with the system size. On the other hand, as shown in Figure 4.4(b), when the buckling is completely suppressed, the energy of the defect in the thermodynamic limit converges to a common value independently of the type of boundaries, with finite size correction $F(N) = C/N$ in which the prefactor C differs for both types of boundaries and the defect orientations. Notice also that in the flat graphene sheet, the DF boundaries give the largest energy for the defect formation in finite-size samples.

4.3.3 Energetics of dislocations in graphene

An SW defect can be considered as a dislocation dipole,²⁷ in which a single dislocation is a pentagon-heptagon pair. Two dislocations can be separated by introducing hexagonal rings in between them as shown in Figure 4.5. We calculated the energy as a function of dislocation separation, measured as the

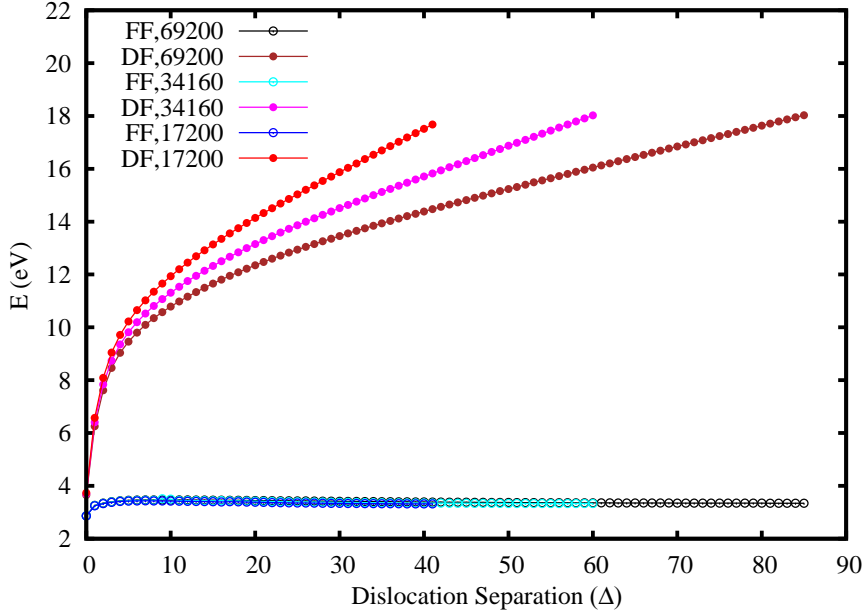


Figure 4.6: The energy of a dislocation pair as a function of the dislocation separation Δ for three different system sizes, 17200, 34160 and 69200 carbon atoms, at two different boundary conditions - FF and DF. Note that the formation energy difference between FF and DF boundaries is more than 10 eV for the largest sample at large dislocation separations.

number Δ of introduced hexagonal rings for two different boundaries (FF and DF) in the samples of three different sizes (17200, 34160 and 69200 atoms).

The effects of the boundaries are even more pronounced when considering this type of defects as shown in Figure 4.6. The size of the energy difference between the FF and DF boundaries for a dislocation pair can be of the order of 10 eV. Moreover, the form of the potential between the dislocations depends heavily on the type of boundaries, implying a strong dependence of the melting temperature of graphene^{168, 169} on the boundary conditions. For FF boundary conditions the energy of a dislocation pair as a function of separation in a buckled graphene membrane quickly becomes constant as predicted by Seung and Nelson in the inextensional limit.¹⁷⁰ The strain field around the core of a dislocation becomes short-ranged when buckling is allowed and therefore the energy converges to a finite value. On the other hand, for DF boundary conditions the energy of a dislocation pair in the buckled crystal increases with separation and this behavior is consistent with the results obtained from a different elastic potential.^{168, 171} The increase in the energy in this case is lower than logarithmic, as predicted by

Seung and Nelson. The strain field around the core of a dislocation does not become localized in the case of DF boundaries since a constant stretching force is applied at the boundaries in order to keep the atom density fixed and this could be the origin of the boundary effects. Furthermore, the force at the boundaries decreases with increasing system size, but at the same time the length of the boundary increases, and the combined effect on the defect's energy apparently is a constant offset as shown by our (2+1)D analytical model and numerical simulations on graphene.

Another qualitative way to understand our results, which at first glance seem surprising, is that a defect such as SW and dislocations, locally deforms the membrane thereby reducing the "footprint" in the 2D plane. With FF boundary conditions, the system can simply shrink to the reduced footprint, but with DF boundary conditions it cannot, resulting in significant stress. The latter raises the energy, even in the thermodynamic limit.

4.4 Conclusion

Our work demonstrates the crucial importance of boundaries for determining the formation energy of the lattice defects. Boundary effects may also be partly responsible for the large variation of the reported formation energies of defects in numerical simulations on the graphene lattice.^{167,172} Simple models for an elastic string and a membrane embedded in a higher-dimensional space suggest their independence of the lattice geometry and the model, and in that sense they may represent a universal feature of the low-dimensional buckled crystals. Our findings may be relevant to graphene samples where SW defects^{22,30,173} and grain boundaries have been observed.^{24,174,175} Finally, our study opens up a route to investigate this boundary effect on the defects' energy in other two-dimensional crystalline materials, such as Mo₂C,¹⁷⁶ as well as in recently synthesized silicene,^{177,178} germanene,¹⁷⁹ and stanene.¹⁸⁰

4.5 Acknowledgments

We are grateful to M. van Huis and J. Zaanen for critical reading of the chapter, and M. Katsnelson for useful discussions.

4.6 Appendices

As discussed in the chapter, effective models are developed to understand the effect of boundary conditions on the formation energy of defects in (1+1) and (2+1) dimensions.

4.6.1 (1+1)D model

In the (1+1)D model, a linear string of atoms is bonded by harmonic springs with unit ideal length, and neighboring bonds prefer to be aligned. The system has periodic boundary conditions, with a periodic length L . The ground state is thus a straight linear, periodic set of atoms in which atom $i = 1 \dots N$ has the coordinates $\vec{r}_i = (i, 0)$; and the periodic length is $L = N$ as shown in Figure 4.1(a).

The Hamiltonian is

$$H = E_{core} + \lambda \sum_i (r_i - 1)^2 + \kappa \sum_i (\phi_{i+1} - \phi_i)^2 - f \left(\sum_i r_i \cos(\phi_i) - L \right). \quad (4.3)$$

The parameters of the Hamiltonian are defined below eq. (4.1) in the chapter.

In this system, a defect is introduced as a single atom with its bonds that prefer to make an angle $\Delta\phi \neq 0$. Below, we present an analytic solution of the energy-minimized positions of the atoms, and in case of FF boundary conditions the periodic length.

FF boundary solution (at relaxed boundaries): With an FF boundary, the net force on the boundary is zero and the energy is minimized for

$$\frac{\partial E}{\partial r_i} = 2\lambda(r_i - 1) = 0, \quad (4.4)$$

$$\frac{\partial E}{\partial \phi_i} = -2\kappa(\phi_{i+1} - \phi_i) + 2\kappa(\phi_i - \phi_{i-1}) = 0. \quad (4.5)$$

4. Boundaries determine the formation energies of lattice defects in 56 two-dimensional buckled materials

Going to the continuum limit (lattice spacing tends to zero), with $i \rightarrow \rho$, the last equation becomes

$$2\kappa \frac{\partial^2 \phi(\rho)}{\partial \rho^2} = 0, \quad (4.6)$$

and the solutions read

$$r(\rho) = 1, \quad (4.7)$$

$$\phi(\rho) = \phi_0(-1 + \frac{\rho}{N}). \quad (4.8)$$

Using these solutions, we obtain a finite-size correction of the energy $E \sim N^{-1}$. We verified this analytical result with numerical simulation data as shown in Figure 4.1(b). The periodic length in this case is

$$L = N \left(1 - \frac{\phi_0^2}{6} \right). \quad (4.9)$$

DF solution (at fixed boundaries): With a DF boundary, a net force is acting on the ends of the string to keep the density of atoms fixed. Therefore, the energy is minimized for

$$\frac{\partial E}{\partial r_i} = 2\lambda(r_i - 1) - f \cos(\phi_i) = 0, \quad (4.10)$$

$$\frac{\partial E}{\partial \phi_i} = -2\kappa(\phi_{i+1} - \phi_i) + 2\kappa(\phi_i - \phi_{i-1}) + f r_i \sin(\phi_i) = 0. \quad (4.11)$$

For small values of ϕ_i , we use $\sin(\phi_i) \approx \phi_i$, to obtain

$$\frac{\partial E}{\partial \phi_i} = 2\kappa(2\phi_i - \phi_{i+1} - \phi_{i-1}) + f r_i \phi_i = 0. \quad (4.12)$$

This equation in the continuum limit($i \rightarrow \rho$) then reads

$$2\kappa \frac{\partial^2 \phi(\rho)}{\partial \rho^2} - f r(\rho) \phi(\rho) = 0. \quad (4.13)$$

For small values of ϕ_i , $\cos(\phi_i) \approx 1$ and in continuum limit $i \rightarrow \rho$, the solutions of eqs. (4.10) and (4.13) read

$$r(\rho) = 1 + \frac{f}{2\lambda} \quad (4.14)$$

$$\phi(\rho) = \phi_0 e^{-\alpha\rho}, \quad (4.15)$$

with

$$\alpha = \sqrt{\frac{f r(\rho)}{2\kappa}}. \quad (4.16)$$

The force required to make the atomic density equal to crystalline density is obtained from the condition of the constant length of the string

$$\sum_i r_i \cos(\phi_i) = x_N - x_0 = N. \quad (4.17)$$

In the continuum limit, $i \rightarrow \rho$

$$\int_0^N d\rho r(\rho) \cos \phi(\rho) = N. \quad (4.18)$$

After substituting the solutions for $r(\rho)$ and $\phi(\rho)$ and using that for $\phi \ll 1$, $\cos \phi \approx 1 - \frac{\phi^2}{2}$, we obtain

$$\left(1 + \frac{f}{2\lambda}\right) \int_0^N d\rho \left(1 - \frac{\phi_0^2}{2} e^{-2\alpha\rho}\right) = N, \quad (4.19)$$

which after performing the integral yields

$$\frac{fN}{2\lambda} - \left(1 + \frac{f}{2\lambda}\right) \frac{\phi_0^2}{4\alpha} = 0. \quad (4.20)$$

Substituting $\alpha = \sqrt{\frac{f r(\rho)}{2\kappa}}$ and $r(\rho) = 1 + \frac{f}{2\lambda} \approx 1$, we obtain

$$f \sim N^{-2/3}. \quad (4.21)$$

Using this result, the finite-size energy for the given solutions scales as $E \sim N^{-1/3}$. We verified this analytical result with numerical simulation data as shown in Figure 4.1(b).

4.6.2 (2+1)D model

The (1+1)D model is then generalized to (2+1)D by imposing rotational symmetry, and constraining the model such that the structure is flat at its perimeter.

The corresponding Hamiltonian reads

$$H = E_{core} + \lambda \sum_i i(r_i - 1)^2 + \kappa \sum_i i(\phi_{i+1} - \phi_i)^2 - f \left(\sum_i r_i \cos(\phi_i) - L \right). \quad (4.22)$$

FF boundary solution (no pulling on the perimeter): At the FF boundary, the net force on the boundary is zero and the energy is minimized for

$$\frac{\partial E}{\partial r_i} = 2i\lambda(r_i - 1) = 0, \quad (4.23)$$

$$\frac{\partial E}{\partial \phi_i} = -2i\kappa(\phi_{i+1} - \phi_i) + 2(i - 1)\kappa(\phi_i - \phi_{i-1}) = 0, \quad (4.24)$$

which in the continuum limit reads

$$2\rho\kappa \frac{\partial^2 \phi(\rho)}{\partial \rho^2} + 2\kappa \frac{\partial \phi(\rho)}{\partial \rho} = 0. \quad (4.25)$$

The solutions of the above equations read

$$r(\rho) = 1, \quad (4.26)$$

$$\phi(\rho) = \phi_0 \left(1 - \frac{\log(2\rho + 1)}{\log(2N + 1)} \right). \quad (4.27)$$

The energy corresponding to the above solutions of $r(\rho)$ and $\phi(\rho)$ scales with the system size as $E \sim \frac{1}{\log(N)}$. This analytical result is in very good agreement with numerical simulation data as shown in Figure 4.1(c). The periodic length in this case is

$$L = N - \frac{\phi_0^2}{2} \left[-\frac{1}{2} - \frac{1}{\log(2N + 1)} + \frac{2N}{\log(2N + 1)^2} \right]. \quad (4.28)$$

DF solution (at fixed boundaries): At the DF boundary, a net force is acting on the ends of the string to keep the density of atoms fixed. Hamiltonian (4.22) then yields

$$\frac{\partial E}{\partial r_i} = 2i\lambda(r_i - 1) - f \cos(\phi_i) = 0 \quad (4.29)$$

$$\frac{\partial E}{\partial \phi_i} = -2i\kappa(\phi_{i+1} - \phi_i) + 2(i-1)\kappa(\phi_i - \phi_{i-1}) + fr_i \sin(\phi_i) = 0. \quad (4.30)$$

In the continuum limit, for small $\phi \ll 1$, the last equation becomes

$$2\rho\kappa \frac{\partial^2 \phi(\rho)}{\partial \rho^2} + 2\kappa \frac{\partial \phi_\rho}{\partial \rho} - fr(\rho)\phi(\rho) = 0. \quad (4.31)$$

The corresponding solutions in the continuum limit read

$$r(\rho) = 1 + \frac{f}{2\rho\lambda}, \quad (4.32)$$

$$\phi(\rho) = K_0 \left(\sqrt{\frac{2f\rho}{\kappa}} \right), \quad (4.33)$$

where $K_0(x)$ is the modified Bessel function of the second kind.

To calculate the force we used the same equation as in (1+1)D model, since the (2+1)D model is rotationally symmetric. In this case, using that

$$\int_0^\infty d\rho \left[K_0 \left(\sqrt{\frac{2f\rho}{\kappa}} \right) \right]^2 = \frac{\kappa}{2f}, \quad (4.34)$$

we obtain that force scales as $f \sim \frac{1}{\sqrt{\log(N)}}$ whereas energy scales as $E \sim \frac{1}{\log(N)}$ with a constant offset. This simple (2+1)D model gives the offset in energy for two different boundaries in the thermodynamic limit which is also shown in graphene samples with defects via computer simulations.

STRUCTURE OF TWISTED AND BUCKLED BILAYER GRAPHENE

Abstract: We study the atomic structure of twisted bilayer graphene, with very small mismatch angles ($\theta \sim 0.28^\circ$), a topic of intense recent interest. We use simulations, in which we combine a recently presented semi-empirical potential for single-layer graphene, with a new term for out-of-plane deformations, [Jain et al., *J. Phys. Chem. C*, 119:9646, 2015] and an often-used interlayer potential [Kolmogorov et al., *Phys. Rev. B*, 71:235415, 2005]. This combination of potentials is computationally cheap but accurate and precise at the same time, allowing us to study very large samples, which is necessary to reach very small mismatch angles in periodic samples. By performing large scale atomistic simulations, we show that the vortices appearing in the Moiré pattern in the twisted bilayer graphene samples converge to a constant size in the thermodynamic limit. Furthermore, the well known sinusoidal behavior of energy no longer persists once the misorientation angle becomes very small ($\theta < 1^\circ$). We also show that there is a significant buckling after the relaxation in the samples, with the buckling height proportional to the system size. These structural properties have direct consequences on the electronic and optical properties of bilayer graphene.

This chapter is based on "Structure of twisted and buckled bilayer graphene" by S. K. Jain, V. Juricic G. T. Barkema, *2D Mater.*, 4:015018, 2016.

5.1 Introduction

Recently, Van der Waals heterostructures made up of two stacked two dimensional materials have drawn lot of attention in materials science and condensed-matter communities because of their peculiar electronic, mechanical and optical properties.⁵⁹ Out-of-plane buckling has a long-range effect in monolayer graphene and has significant impact on its structural properties and defect mechanics.^{20, 47, 112, 149, 181} The resulting nanometer sized ripples have been studied experimentally by transmission electron microscopy (TEM)¹⁸² and scanning probe microscopy.^{183–186} Out-of-plane ripples in bilayer graphene have been detected and investigated via TEM^{187, 188} and the combination of dark-field TEM with scanning transmission electron microscopy (STEM).¹⁸⁹ The buckling effect in bilayer graphene has also been studied using computer simulations.^{190–192}

From the point of view of its electronic and structural properties, twisted bilayer graphene (TBLG) is most interesting when the mismatch angle is small. To theoretically obtain the structure of the TBLG with periodic boundary conditions and such small mismatch angles, it is necessary to consider samples with a large size. An approach based on an effective elastic potential is quite appealing in this regard since it allows to treat systems containing millions of atoms. Since we do not restrict ourselves to completely flat graphene layers but allow for some buckling, we use a combination of potentials, based on the recently developed semi-empirical potential for the monolayer graphene¹⁴⁹ with a new term describing out-of-plane deformations, and the more standard registry-dependent interlayer graphitic potential¹⁹³ to simulate relaxed large bilayer graphene structures with very small mismatch angle ($\theta \approx 0.28^\circ$). This combination of potentials is computationally cheap and accurate.

In energy-minimized (relaxed) samples, vortices arise in the atomic displacement field, due to the energy differences between different kinds of stacking, in agreement with previous studies.^{190, 192, 194} We show that after relaxation the size of these vortices approaches a constant in the thermodynamic limit. Furthermore, we study out-of-plane buckling in bilayer graphene and find that the buckling height increases linearly with system size. We show that the buckling in the pristine bilayer graphene is significant ($\sim 3 \text{ \AA}$) and forms a Moiré pattern analogous to the in-plane displacement without any singularities and with long range structural effects.

5.2 Method

We use a new combination of intralayer and interlayer potentials to simulate bilayer graphene. For the interactions within the same layer, we use the recently developed semi-empirical potential for single-layer graphene by Jain et al.,¹⁴⁹ which has a new out-of-plane deformation term. The interlayer interactions are defined by the registry-dependent Kolmogorov-Crespi potential without the local normals.¹⁹³ This combination of empirical potentials is precise and accurate enough to capture the physical and structural changes in the system without any heavy computational requirements. These properties of the potential gives us freedom to study very large samples, which is required for having very small mismatch angles under periodic boundary conditions. In all samples studied, the energy is locally minimized, starting from well-informed choices for the initial configurations: insight obtained from many simulations of small systems is exploited to start the energy minimization of large samples from already well-relaxed samples. In our samples, we define a local energy per atom as follows: contributions due to two-body interactions are equally divided over the two interacting atoms, and contributions due to the three-body (angular) interactions are attributed to the central atom. Thus, the sum of the local energy over all atoms equals the total energy. This definition of local energy helps us to visualize the local degree of mechanical relaxation in the sample.

5.3 Results and discussion

Here we show the Moiré patterns in the twisted bilayer graphene. Furthermore, we present the structure and scaling behavior of vortices and line mismatch in TBLG samples. We also describe the out-of-plane buckling behavior as a function of twist angle.

5.3.1 Structure of twisted bilayer graphene

We start with a sample having 1524 atoms in both layers with a mismatch angle of $\theta = 5.09^\circ$ between the layers as shown in Figure 5.1(a). The Moiré patterns

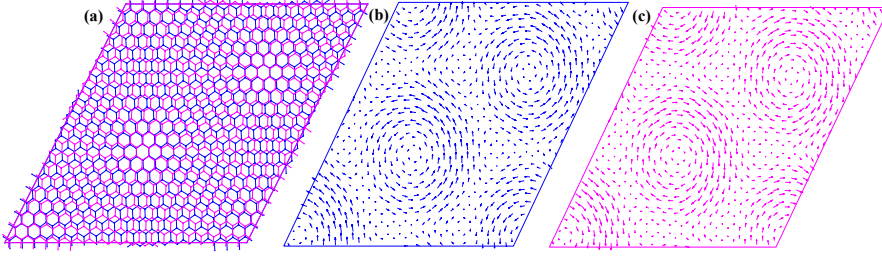


Figure 5.1: Bilayer graphene sample with 1524 atoms and with mismatch angle $\theta = 5.09^\circ$. (a) Sample before relaxation. (b) Effect of relaxation in the bottom layer where atoms rotate counterclockwise near the vortex to minimize the total energy. (c) Effect of relaxation in the top layer where atoms rotate clockwise near the vortex in order to minimize the total energy. For visibility, the displacement arrows are enlarged by a factor of 20.

are clearly visible in the sample along the diagonal. This sample is relaxed with the above described combination of potentials, and its effect on atomic relaxation in bottom and top layers is shown in Figure 5.1(b) and Figure 5.1(c), respectively. The arrows in the figure describe the relative atomic displacement after the relaxation with respect to the unrelaxed positions (i.e. the positions in top and bottom layer in the crystalline state of the individual graphene layers). Atoms near the center of AA stacking rotate to minimize the total energy and show a Moiré pattern of displacement vectors with respect to their initial positions in the form of vortices. In this case atoms in the bottom layer rotate in the counterclockwise direction whereas atoms in top layer rotate clockwise, since the center of mass of the system is unaltered. During the process of relaxation the AA-stacked area becomes smaller while AB-stacked area grows, since the energy of AB-stacking is lower compared to AA-stacking. This result is in agreement with previous studies on TBLG.^{190,194} Relaxed bilayers have the intrinsic ripples in the structure and the equilibrium separation between the layers is 3.46 Å .

To study the effect of relaxation qualitatively, we generate a sample having 15132 atoms with a mismatch angle of 1.61° . The local energy profile of the sample before and after the relaxation is shown in Figure 5.2(a) and Figure 5.2(b), respectively. The binding energy of AA and AB stacking after the minimization is 11.8 meV/atom and 17.5 meV/atom respectively which is in very good agreement with reported values by Mostaani *et al.* calculated using quantum Monte Carlo technique.¹⁹⁵ The energy along the diagonal principal axis PQ behaves as a sinusoidal function before and after the relaxation for large values of the mismatch angle, as shown in Figure 5.2. However, this sinusoidal

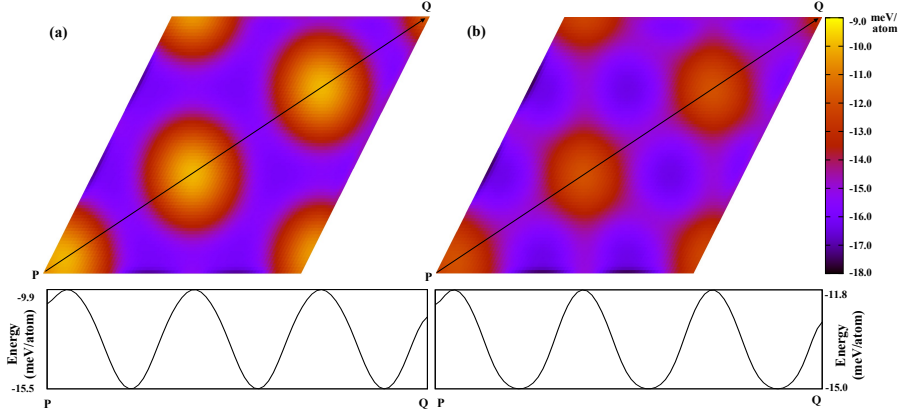


Figure 5.2: Local energy profile of a sample having 15132 atoms with $\theta = 1.61^\circ$. (a) Before the relaxation. (b) After the relaxation. The bottom panel depicts the local energy along the main diagonal axis PQ which shows sinusoidal behavior in this case.

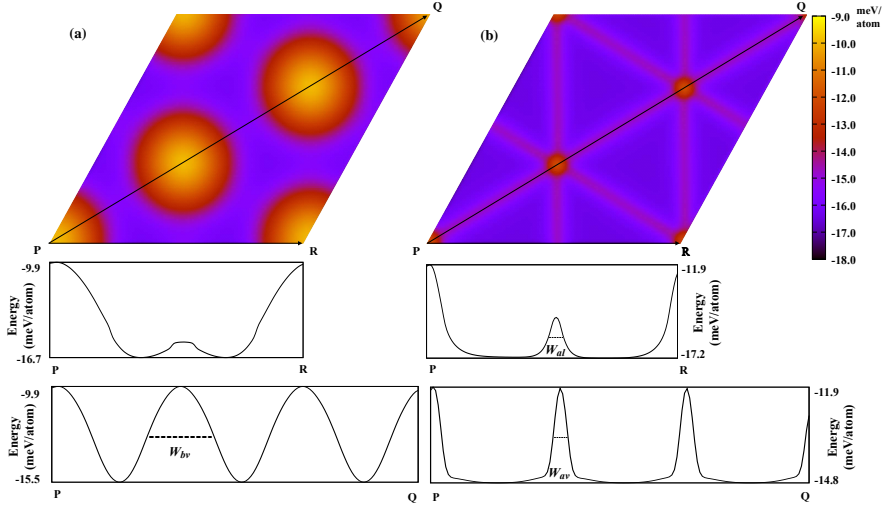


Figure 5.3: Local energy profile of a sample having 321,492 atoms with $\theta = 0.35^\circ$. (a) Before the relaxation. (b) After the relaxation. The bottom panels depict the local energy along the two principal axes of the vortex lattice, horizontal PR and diagonal PQ. This shows that sinusoidal behavior is not present at smaller θ along the PQ direction.

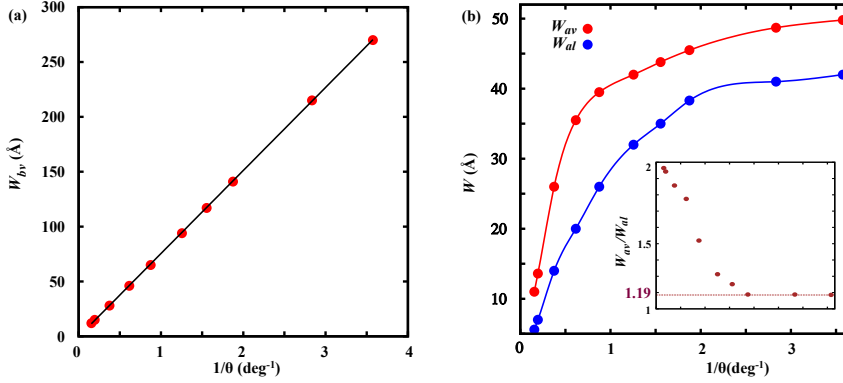


Figure 5.4: Scaling behavior of peak widths corresponding to the size of the vortices as a function of inverse of the mismatch angle ($1/\theta$). We simulate the system sizes from 964 atoms ($\theta = 6.40^\circ$) to 511,228 atoms ($\theta = 0.28^\circ$). (a) W_{bv} (width of vortices peak at half its height, before relaxation) as a function of inverse of the mismatch angle. We observe a linear scaling with $1/\theta$. Since θ scales as inverse of L , W_{bv} scales linearly with system size. (b) W_{av} (width of vortices peak at half its height, after relaxation) and W_{al} (width of line peak at half its height, after relaxation) as a function of inverse of the mismatch angle. At large system's sizes and small mismatch angle ($\theta < 0.6^\circ$) the ratio between these two peak widths becomes constant (inset).

behavior of energy is no longer present for small mismatch angles ($\theta < 1^\circ$), as shown in Figure 5.3. The elastic energy becomes rather concentrated at the well-defined vortices in the displacement field. The local energy profile of the sample having 321,492 atoms with mismatch angle of 0.35° , before and after the relaxation is shown in Figure 5.3(a) and Figure 5.3(b), respectively. Our simulations show that before relaxation the size of the vortex around AA stacking increases linearly with system size $L \sim \sqrt{N} \sim 1/\theta$, with N as the number of atoms. The width of the peak at half maximum height along the diagonal PQ before the relaxation is given as W_{bv} and plotted as a function of $1/\theta$ in Figure 5.4(a). Here, the subscript b stands for 'before relaxation', and the subscript v for 'vortex'. Further on in this manuscript, we will also use subscripts a and l , which stand for 'after relaxation' and 'line', respectively. We calculate the peak width along the diagonal PQ after the minimization (W_{av}) and plot it as a function of $1/\theta$ as shown in Figure 5.4(b). For large system size W_{av} appears to approach a constant value of ~ 50 Å. We also calculate the peak width after the minimization along the line PR, represented as W_{al} . In the local energy profile of relaxed samples, vortices are connected via a line which denotes a configuration with the structure in-between AA and AB stacking as shown in Figure 5.5(b). The binding energy of this kind of stacking is 14.8 meV. We plot

W_{al} as a function of $1/\theta$ and find that at small mismatch angles (large system sizes) it also approaches a constant value of ~ 42 Å. The ratio between W_{av} and W_{al} becomes constant for all the systems with mismatch angle below 0.6° as shown in inset of Figure 5.4(b). We find that the value for the constant ratio is 1.19 in the thermodynamic limit.

The Bernal stacking in BLG has been investigated experimentally via STEM, where it has been shown that regions of AB and BA stacking are separated by nanometer wide rippled boundaries.^{187, 189} In our simulations this is also the case as shown in Figure 5.3 where lines connecting the vortices are separating AB and BA stackings. We present the detailed structures of these vortices, lines and Bernal stackings with displacement fields in Figure 5.5. Recent studies by Dai *et. al.* determining the size of the lines and vortices using the Peierls-Nabarro model^{191, 192} are in very good agreement (within 10%) with our estimate of constant size in the thermodynamic limit. Alden *et. al.* use the Frenkel-Kontorava model¹⁹⁶ and report a size which is significantly larger than experimental observation.¹⁸⁷

With very small mismatch angles and thus very large Moiré patterns, most of the additional energy, ΔE , due to the Moiré pattern comes from the lines connecting the vortices, as these lines grow with decreasing angle, while the vortices do not. The additional energy due to the Moiré pattern is a combination of intralayer and interlayer energy terms. The intralayer energy contribution decreases inversely proportional to the line width w_{al} , while the interlayer energy contribution increases linearly with line width

$$\Delta E = aw_{al}L + b\frac{L}{w_{al}}, \quad (5.1)$$

where the parameter a is determined by the energy difference between the different stackings, and b is determined by the bulk modulus of a graphene layer.

In classical elastic bead spring models with a fixed extension, the extension per spring in the system decreases linearly with the number of the springs. With harmonic springs, the energy per spring scales quadratically with extension, and the total energy thus decreases linearly with the number of springs. Here in eq. (5.1), w_{al} is analogous to the number of the springs. Therefore, the intralayer energy contribution decreases inversely proportional to the line width w_{al} . The interlayer energy simply depends on the mismatched area in the sample and therefore scales linearly with w_{al} .

Minimizing ΔE with respect to the line width results in an L -independent w_{al}

given as

$$w_{al} = \sqrt{b/a}. \quad (5.2)$$

Therefore, in the large samples where the size of vortices becomes constant, the width of the line connecting the vortices also becomes constant since it only depends on the bulk modulus of graphene and the type of stacking between two layers. In our numerical simulations we find the trend which is consistent with this analytical argument. We have calculated the value of interlayer energy constant as $a = 0.0018 \text{ eV}/\text{\AA}^2$ and intralayer energy constant as $b = 3.1750 \text{ eV}$ by fitting our numerical energy data to eq. (5.1). The value of w_{al} obtained by solving eq. (5.2) for these values of constants is in excellent agreement with the value predicted ($\sim 42 \text{ \AA}$) in Figure 5.4(b).

We minimize the samples in all directions for two different boundary conditions: deformation-free (DF) boundary conditions where the periodic box is determined by the crystalline structure of single undeformed graphene layers, and force-free (FF) boundary conditions where changes in the simulation box are allowed:¹⁹⁷ the length of each of the periodicity vectors as well as the angle between them is determined by the constraint of minimal total energy. Our results on energetics of TBLG (Figures 5.2-5.5) are based on DF boundary conditions since structures with DF boundaries allow us to compare atomic coordinates before and after relaxation without complications due to differences in box size. Moreover, we verified that the shrinkage in the box size and the differences in the energies between two different boundary conditions are very small ($< 0.08\%$) and do not alter the results and predictions presented in the paper. But this small decrease in the box size has very significant consequences on the buckling height, which we discuss next.

5.3.2 Buckling in twisted bilayer graphene

We now consider out-of-plane deformations in the TBLG samples. Our samples before the relaxation have completely flat layers separated by 3.4 \AA in the z -direction. The minimized structures have out-of-plane deformations characterized by the type of stacking between the layers. In Figure 5.6(a) we show the structure of ripples in a sample with $N = 15132$ atoms after the complete relaxation. The equilibrium average separation distance is 3.44 \AA in between the layers. The profile of out-of-plane deformations in the top layer is shown in Figure 5.6(b). The buckling height in the individual layer is 0.51 \AA for DF boundaries. For FF boundaries the buckling height is more significant and reaches a value of 1.12 \AA . The out-of-plane deformations along the diagonal PQ direction are plotted

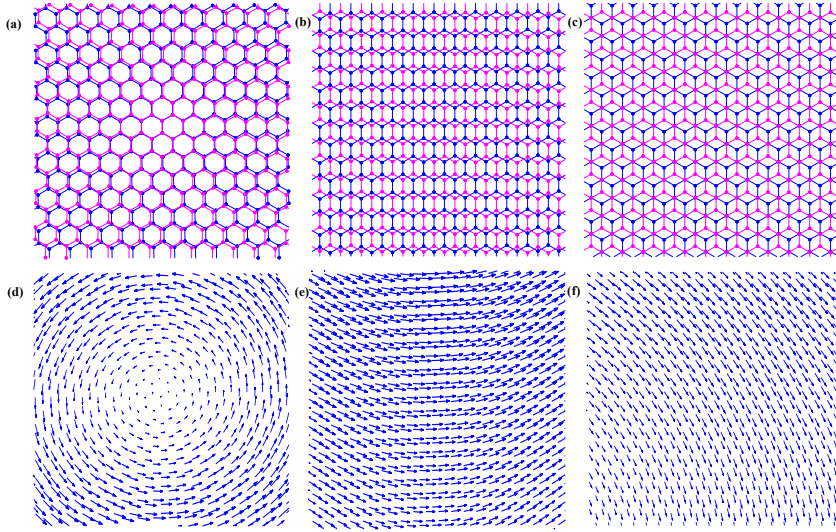


Figure 5.5: Detailed structures and displacement fields around a vortex, line and Bernal stacked (AB/BA) region. (a-c) Atomic structures of a vortex, line and Bernal stacked (AB/BA) region, respectively. Here blue color is used for bottom layer and magenta color is used for top layer. (d-f) Displacement fields around a vortex, line and Bernal stacked (AB/BA) region in bottom layer with respect to their unrelaxed positions, respectively. The area for which the displacement fields are shown is $40\text{\AA} \times 40\text{\AA}$. For visibility, the displacement arrows are enlarged by a factor of 8.

in both top and bottom layer, as shown in Figure 5.6(d). The behavior along the PQ direction is sinusoidal and the separation around AA stacking is 3.62\AA , in good agreement with previously reported values in literature calculated using density functional theory (DFT) calculations.^{194, 198} Most importantly, we observe a Moiré pattern-like feature in the buckling height, see Figures 5.6(b) and 5.7(b).

We now discuss in more detail features of the spatial pattern in the buckling height. As we already pointed out, with increasing system size the vortex in the in-plane displacement around AA stacking shrinks after the minimization and appears to become constant for $\theta < 0.6^\circ$. This feature yielding a characteristic length scale can also be seen in the buckling of a sample having 321,492 atoms ($\theta = 0.35^\circ$), as shown in Figure 5.7. Namely, the characteristic length scale in this case is the equilibrium average separation distance, and its size relative to the system size decreases with increasing system size, since the AB stacked area grows and AA stacked area does not. In this case it has the value of 3.38\AA . The sinusoidal behavior in the buckling, as shown in Figure 5.6(d), disappears for small mismatch angles as shown in Figure 5.7(d). Finally, the buckling height

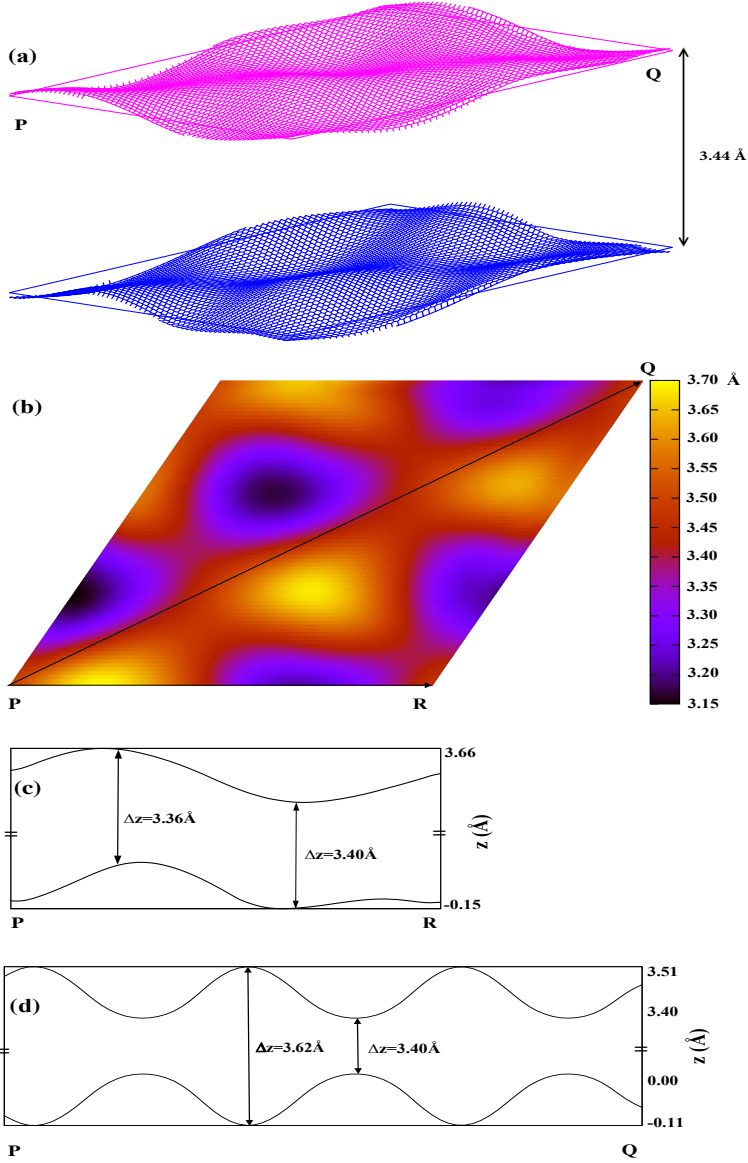


Figure 5.6: Buckling behavior in a sample with 15132 atoms ($\theta = 1.61^\circ$). (a) Ripples in both top and bottom layer. The equilibrium separation between both layers is 3.44 \AA . (b) Buckling profile of the top layer for DF boundary conditions. The buckling height is 0.51 \AA . (c) Buckling along the line PR in both the layers. Around the AB stacked area the separation between the layers is 3.36 \AA . (d) Buckling along the diagonal PQ in both the layers. Around the AA stacked area the separation between the layers is 3.62 \AA .

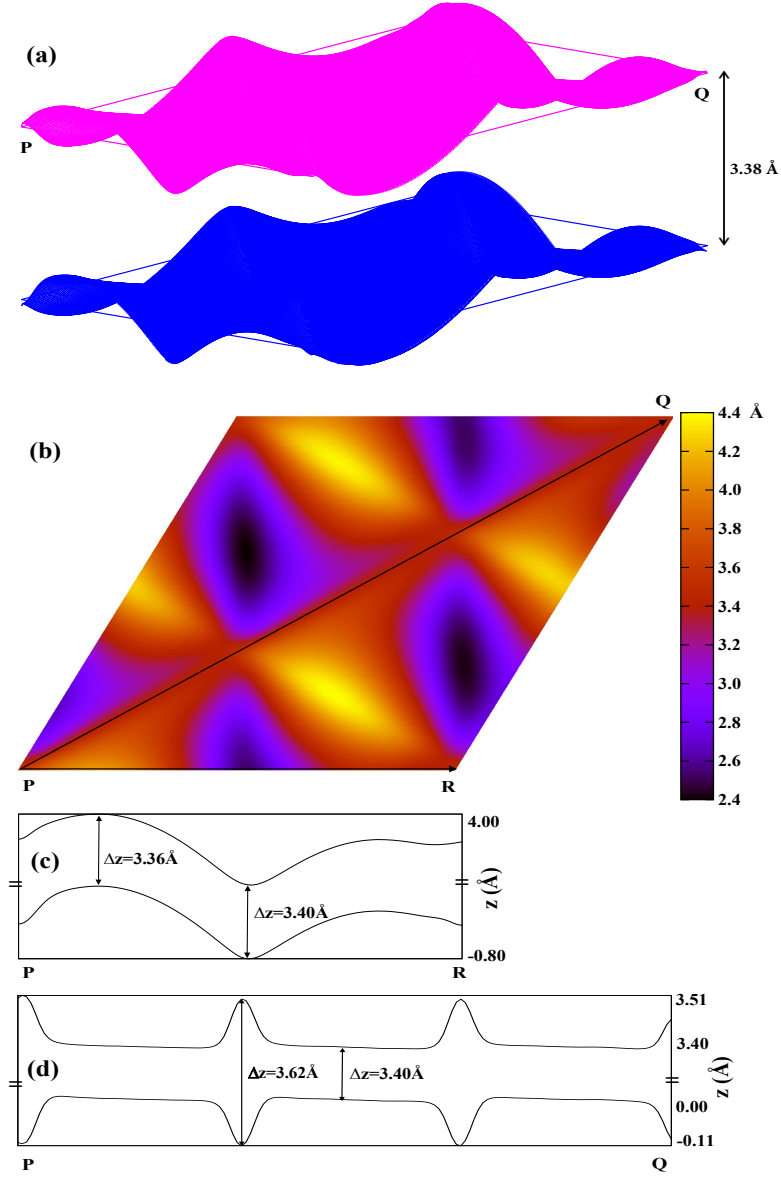


Figure 5.7: Buckling behavior in a sample with 321,492 atoms ($\theta = 0.35^\circ$). (a) Ripples in both top and bottom layer. The equilibrium separation between both layers is 3.38 \AA . (b) Buckling profile of the top layer. The buckling height is 1.74 \AA . (c) Buckling along the line PR in both the layers. Around the AB stacked area the separation between the layers is 3.36 \AA . (d) Buckling along the diagonal PQ in both the layers. Around the AA stacked area the separation between the layers is 3.62 \AA .

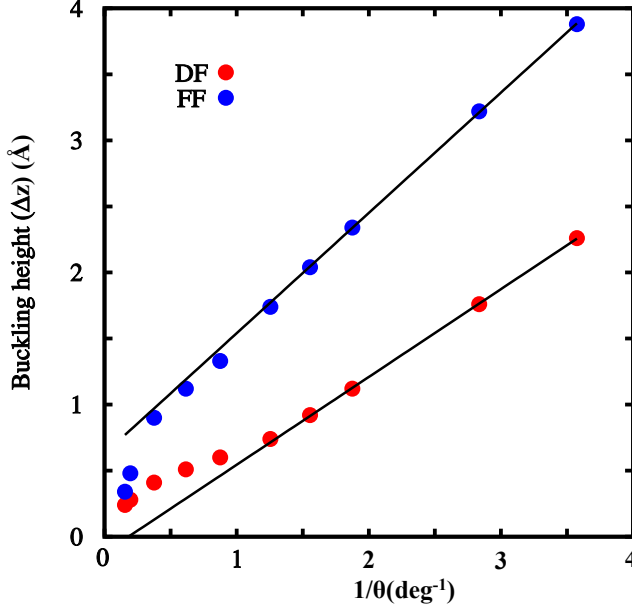


Figure 5.8: Buckling height as a function of inverse of the mismatch angle ($1/\theta$) for both DF and FF boundary conditions. For large system sizes (small θ), the scaling of the buckling height is linear with the system size. Intrinsic ripples are significant and have the values of height 2.3\AA and 3.8\AA for DF and FF boundary conditions, respectively, in a sample with $N = 511,228$ atoms with $\theta = 0.28^\circ$.

increases linearly with system size for both DF and FF boundary conditions, as shown in Figure 5.8. The buckling height for the largest sample ($N = 511,228$ atoms with $\theta = 0.28^\circ$) studied by our simulations for FF boundary conditions is quite significant as the value is 3.78\AA .

For the smallest twist angle under periodic boundary conditions ($\theta \sim 1/L \sim 1/\sqrt{N}$), each “mismatch line” seems to induce a small, constant buckling angle, which causes a buckling height that increases linearly with system size L . Without periodic boundaries, the twist angle is not discretized and can approach zero at any fixed system size; but we only simulated periodic boundaries. It is however clear that if at fixed L the twist angle approaches zero, the buckling height has to approach zero as well, as the system then gradually approaches the perfectly aligned crystal, which is flat.

5.4 Conclusion

Our work demonstrates the crucial importance of having large, well-relaxed samples of twisted bilayer graphene, to study its structural properties. The new combination of intralayer and interlayer potentials uses explicit lists of bonds and is therefore computationally very cheap. This allows us to accurately simulate very large TBLG samples with very small mismatch angles. The simulation results are in very good agreement with reported in the literature. There are sinusoidal modulations in the energy and buckling height for large misorientation angles but this behavior no longer persists at small misorientation angles. We have shown with large scale atomistic simulations that the size of the vortices in the displacement field approaches a constant in the thermodynamic limit. There are significant out-of-plane deformations which increase with increasing system size. The characteristic average separation between the layers also becomes constant in the thermodynamic limit. These structural properties should have direct effect on electronic and optical properties of twisted bilayer graphene. In future work, the same combination of potentials can be modified with different structural parameters to investigate other misaligned two-dimensional materials such as h-BN, MoS₂ and WSe₂.

PROBING THE SHAPE OF A GRAPHENE NANOBUBBLE

Abstract: Gas molecules trapped between graphene and various substrates in the form of bubbles are observed experimentally. The study of these bubbles is useful in determining the elastic and mechanical properties of graphene, adhesion energy between graphene and substrate, and manipulating the electronic properties via strain engineering. In our numerical simulations, we use a simple description of elastic potential and adhesion energy to show that for small gas bubbles (~ 10 nm) the van der Waals pressure is in the order of 1 GPa. These bubbles show universal shape behavior irrespective of their size, as observed in recent experiments. With our results the shape and volume of the trapped gas can be determined via the vibrational density of states (VDOS) using experimental techniques such as inelastic electron tunneling and inelastic neutron scattering. The elastic energy distribution in the graphene layer which traps the nanobubble is homogeneous apart from its edge, but the strain depends on the bubble size thus variation in bubble size allows control of the electronic and optical properties.

6.1 Introduction

Due to remarkable and unusual electronic and mechanical properties,^{2,199} graphene has recently attracted a great deal of attention.^{138,200–202} This is so because graphene has emerged as a very strong material.¹³ Its mechanical properties are also fundamentally and practically interesting when it is in contact with other materials. For instance, due to a strong van der Waals (vdW) force, graphene can build bilayer, twisted bilayer, trilayer and other heterostructures.⁵⁹ These van der Waals heterostructures are useful in nanotechnology and semiconductor industry because of the flexibility to tailor their properties.

Yet another important physical and chemical aspect of graphene is its ability to trap gas molecules under high pressure when placed on different substrates, leading to a formation of bubbles with nanometer to micrometer sizes. Such nanobubbles have been experimentally observed in a graphene membrane placed on top of a SiO₂/Si substrate,^{87,88} epitaxial graphene grown on 4H-SiC,⁸⁹ and in an irradiated graphene sample on Ir.⁹⁰

The vdW pressure inside the bubble has significant impact on the physical and chemical properties of these nanobubbles and thus also on the performance of the devices made up by them. Therefore, there is ample employ for simulations which can accurately predict the structural changes in the samples. Very recently, nanobubbles of different sizes, ranging from a few tens of nanometers to a micrometer, and shapes, such as circular, trapezoidal, and triangular, have been found in van der Waals heterostructures.¹⁰⁷ Importantly, circular bubbles show universal scaling behavior which can be captured by elastic continuum theory.¹⁰⁷ However, it is not known whether this universal behavior extrapolates to the bubbles of smaller sizes down to ~ 10 nm.

In this chapter, we numerically simulate graphene nanobubbles of various sizes, starting with the ones with a radius (R) of ~ 10 nm. We use a computationally cheap and accurate semi-empirical potential to simulate the graphene sheet. The adhesion is modeled by a simple potential that produces essential elastic properties of the bubble, such as universal scaling of the aspect ratio h/R , with h as its height, observed in large circular bubbles. Furthermore, we find that the pressure of trapped ideal gas for the smallest bubbles of size ~ 10 nm shows scaling with the aspect ratio as the elastic continuum theory predicts. The van der Waals pressure for these bubbles is in the order of 1 GPa. We find that the vibrational density of states (VDOS) can be used as an independent tool to detect the volume of gas trapped inside the bubble. It is interesting to notice

that many soft vibrational modes appear in the VDOS because of the formation of bubbles. Finally, we map out the profile of elastic energy, as this can be used to extract the strain distribution of the bubble.

6.2 Method

To simulate the monolayer graphene, we use a recently developed effective semiempirical elastic potential described in Chapter 2, eq. (2.2).¹⁴⁹ Additionally, the interaction between substrate and graphene layer is described by an extra harmonic term

$$E_S = K \sum_i \frac{z_i^2}{1 + (z_i/z_0)^2}, \quad (6.1)$$

where K is the effective elastic constant for the graphene-substrate interaction which determines the strength of the adhesion of graphene to the substrate, z_0 is a constant which sets the range of the harmonic regime of the energy term, and z_i is the distance of carbon atom i from the graphene plane. The theoretical prediction of adhesion energy for various substrates is $\sim 0.01 - 0.02$ eV/Å²,^{203,204} and therefore in our numerical simulations we use the values of elastic constant $K = 0.01$ eV/Å² and $z_0 = 2$ Å to capture the effects of various substrates.

In our numerical simulations, a cone shaped initial void is created by pulling some carbon atoms out of the graphene plane and a fixed number of ideal gas molecules (N) are placed in the void. The whole system is then relaxed by the potential (eq. (2.2)) combined with the substrate potential (E_S) (eq. (6.1)) and the ideal gas law. We use deformation free (DF) periodic boundary conditions in our simulations.¹⁹⁷ The resulting structure has the well relaxed round shaped bubble filled with gas molecules as shown in Figure 6.1. The vibrational spectrum is obtained by diagonalising the hessian matrix generated from above potential.²⁰⁵ In our plot, the VDOS is convoluted with a Gaussian function with a width of $\sigma = 14$ cm⁻¹.

6.3 Results and discussion

We have studied the small ~ 10 nm and big ~ 100 nm graphene gas bubbles. These bubbles have shown universal shape behavior and the vdW pressure inside

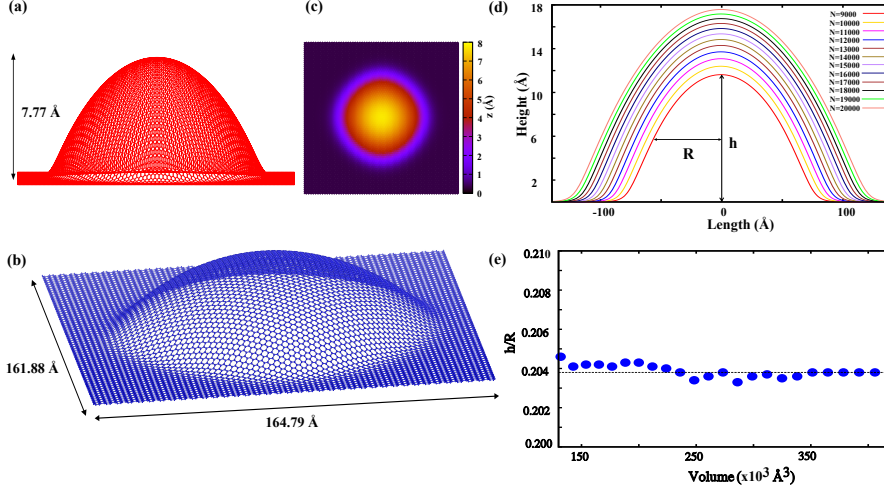


Figure 6.1: Shape and profile of a gas bubble at the interface between graphene and a substrate. (a) Side view of a bubble trapped in a graphene layer with 10184 carbon atoms. The height (h) of the bubble is 7.77 Å . For better visibility the height scale is increased. (b) Top view of the same bubble with its lateral dimensions. (c) Height profile of the same bubble. (d) 2D profile of the bubbles with varying number of the ideal gas molecules (N) trapped under a graphene layer with 34160 carbon atoms. The radius (R) of the bubble is measured at half of the bubble's maximum height. (e) Measured aspect ratios (h/R) as a function of volume show the constant behavior implying the universal shape of the bubble.

the small bubble is in the order of 1 GPa. Furthermore, we calculate the VDOS of a gas nanobubble. We also map out the local energy distribution in a graphene nanobubble.

6.3.1 Structure of graphene nanobubble

The graphene bubble we obtain using numerical simulations is shown in Figures 6.1(a) (side view) and 6.1(b) (top view). The round-like shape of the bubble results from the competition of the forces arising from pressure exerted by the ideal gas on the membrane and the elastic forces of graphene and substrate encoded in the semiempirical potential eq. (2.2) in our simulations. The height of the bubble, shown in Figure 6.1(c), varies with the radius of the bubble, see Figure 6.1(d). The aspect ratio $h/R \simeq 0.204$ remains constant as the volume of the bubble changes with the number of the trapped molecules of the ideal gas,

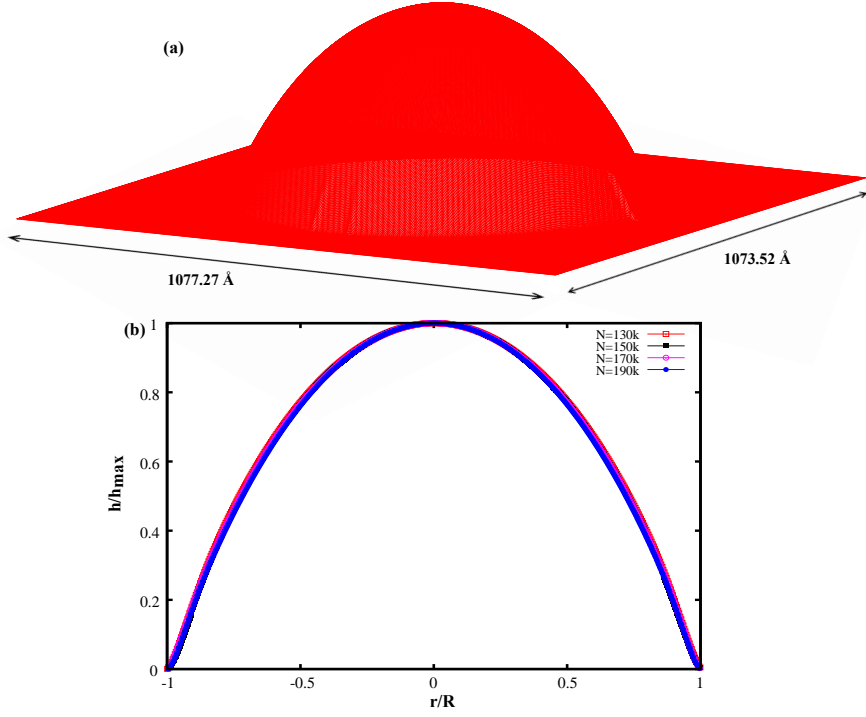


Figure 6.2: Profile of a large graphene bubble. (a) A gas bubble trapped between a graphene sheet with 441504 carbon atoms and a substrate. (b) The excellent collapse of the data of bubble's profile with varying sizes shows the universal shape of the bubble.

as shown in Figure 6.1(e). This ratio only depends on the elastic properties of graphene and van der Waals attraction between graphene and substrate, and is therefore independent of the properties of the trapped substance. This result is in excellent agreement with the prediction from the elastic continuum theory¹⁰⁷ and continuum membrane plate theory.^{206,207} Furthermore, it demonstrates that the elastic continuum can be used for the description of bubbles of much smaller sizes than the ones experimentally studied by Khestanova *et. al.*¹⁰⁷ On the other hand, this implies that the deviations from this universal ratio are caused by external effects (i.e., residual strains in the samples, experimental conditions), which provides a possible route for the control of the shape of the bubble. We also study the universal shape behavior in much bigger gas bubbles trapped in a graphene sheet in simulations with 441504 carbon atoms as shown in Figure 6.2.

To further theoretically demonstrate the predicted universal properties of the

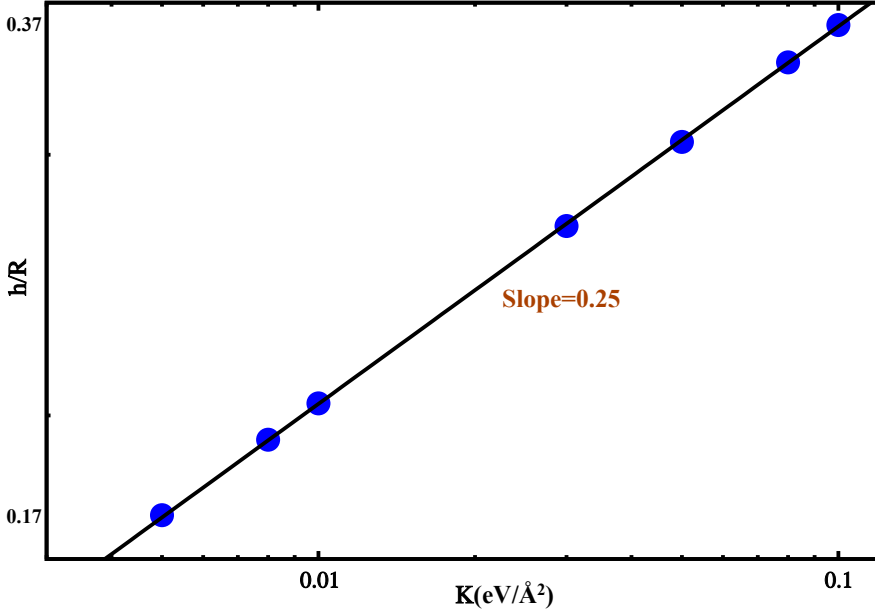


Figure 6.3: Log-log plot between aspect ratio h/R and the intensity K of the substrate potential in eq. (6.1). The numerical data points (blue) are fitted with a straight line with a slope of 0.25. This shows that the aspect ratio scales as $h/R \sim K^{1/4}$.

graphene bubble, we study the dependence of the aspect ratio on the strength of the substrate potential, K , which in our simulations plays the role of the adhesion energy in the experiments. Here, we vary the strength of this potential, which is not possible in experiments without changing substrates, and allow the bubble to relax. We observe the scaling of the aspect ratio with the strength of the substrate potential, $h/R \sim K^{1/4}$, as shown in Figure 6.3, and in agreement with theoretical prediction by Khestanova *et. al.*¹⁰⁷ The obtained scaling in fact independently confirms the mechanism of the bubble formation through the interplay between the vdW and elastic forces. On the other hand, it shows that this rather simple effective substrate potential (E_S) can be used to effectively describe the adhesion at the interface between a graphene sheet and a substrate.

Ideal gas is trapped inside the graphene bubble and in Figure 6.4(a) we show its equation of state corresponding to temperature $T \simeq 300$ K. From continuum elastic theory the pressure of the trapped ideal gas is predicted to scale as $P \sim V^{-1/3}$. This behavior is indeed observed in our numerical calculations, as shown in Figure 6.4(b), which further corroborates the validity of this relatively

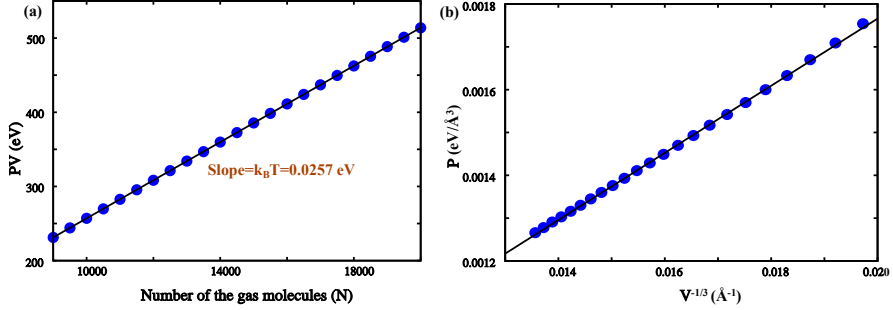


Figure 6.4: Behavior of pressure (P) and volume (V) of the ideal gas trapped inside the bubble. (a) PV versus number of gas molecules N . According to the ideal gas law $PV = NK_B T$; at room temperature the slope of the line is $K_B T = 0.0257$ eV. (b) Plot of P versus $V^{-1/3}$. Data points (blue) are fitted with a straight line, showing $P \sim V^{-1/3}$.

simple theoretical approach for addressing the problem. The vdW pressure inside the bubble is of the order of 1 GPa and therefore has direct experimental consequences on the properties of the trapped materials.^{97–101}

6.3.2 VDOS of graphene nanobubble

We now study an independent method for probing a graphene bubble via its characteristic "drumming" modes. More precisely, we here calculate the vibrational density of states (VDOS) of characteristic phonon modes of the graphene bubble. Out of all possible vibrational modes, most prominent are the out-of-plane L and L' modes,²⁰⁵ shown in Figure 6.5(a). The presence of the bubble gives rise to a systematic shift in the position of the peaks in the VDOS corresponding to these two modes. As we can observe in Figure 6.5(b), as volume of the bubble increases (pressure inside the bubble decreases) the frequency of both L and L' modes shifts towards higher values (blue shift). At the same time, this shift is correlated with a decrease of the intensity of these modes, as shown in Figures 6.5(c) and 6.5(d). For a relative increase of the volume of the bubble by $\sim 50\%$, the relative decrease in the intensity of both modes is $\sim 5\%$, while the frequency of the L mode increases by $\sim 5\%$ and that of L' by $\sim 10\%$. These changes in the intensity and the frequency of these characteristic modes are therefore significant, and may be used as independent

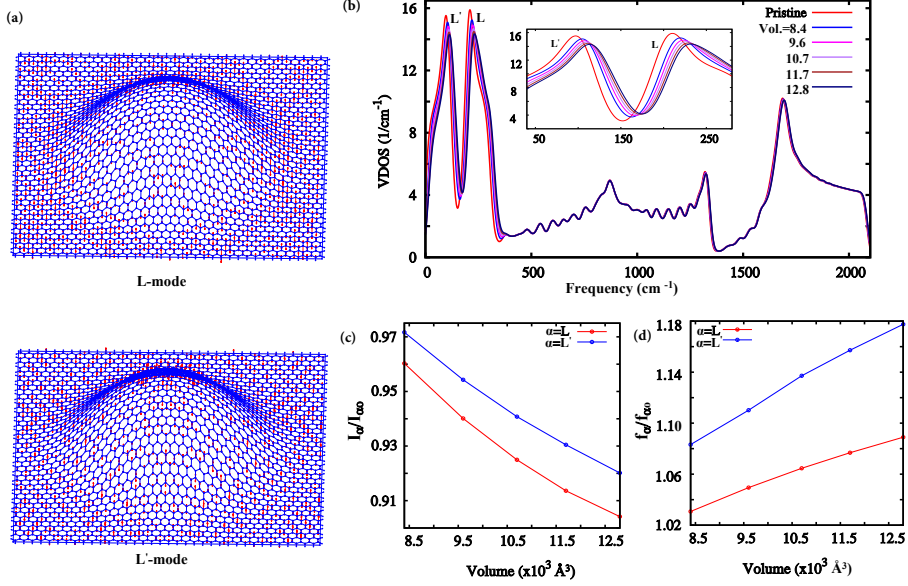


Figure 6.5: Vibrational density of states (VDOS) and the profile of the prominent modes in the graphene nanobubble. (a) Profile of vibrational modes corresponding to L and L' peaks, respectively. (b) VDOS of pristine graphene and samples with varying volume (in 10^3 \AA^3) of the ideal gas trapped in the bubble. Inset: Low-frequency peaks (L and L') in VDOS zoomed in. (c) Relative decrease in the intensity of L and L' modes at different volumes of the bubble. (d) Relative increase (blue shift) in the frequency of L and L' modes at different volumes of the bubble.

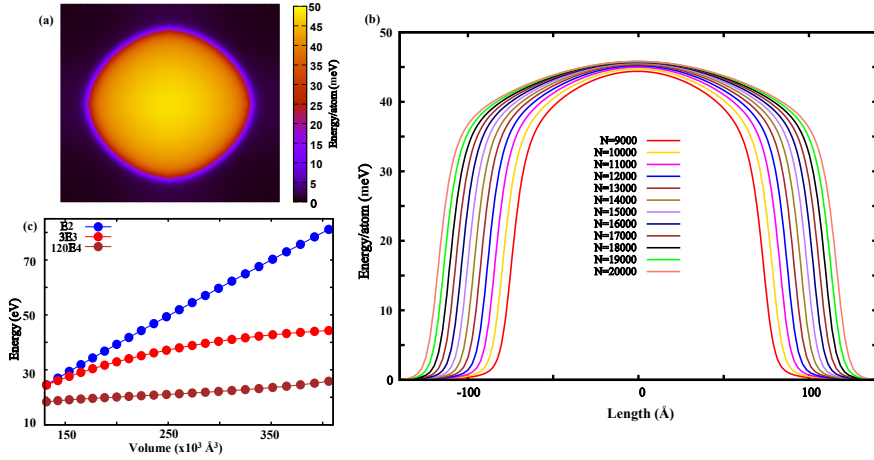


Figure 6.6: Behavior of the elastic energy of a graphene layer with a trapped gas bubble. (a) Local energy plot of a sample with gas bubble ($N = 18000$). (b) Profile of the energy distribution in the graphene layer as a function of the distance from the center of the bubble for different number of gas molecules trapped inside it. The center is determined by projecting the point of the maximum height onto the flat graphene plane. (c) Behavior of different elastic energy terms in eq. (2.2) as a function of the bubble's volume: bond stretching (E_2), bond bending (E_3) and out-of-plane (E_4).

probes to measure shape and gas volume trapped in the nanobubbles in the inelastic electron tunneling and inelastic neutron spectroscopy.

6.3.3 Elastic energy distribution in nanobubble

We next study the elastic energy distribution of the graphene bubble. Elastic energy is directly related to strain, which is in turn important for strain engineering. We compute the elastic energy per atom using the combination of semi-empirical elastic potential eq. (2.2) and adhesion energy (E_S) in eq. (6.1). In our samples we define a local energy per atom as follows: contributions due to two-body interactions are equally divided over the two interacting atoms, and contributions due to the three-body (angular) interactions are attributed to the central atom.²⁰⁸ Thus, the sum of the local energy over all atoms equals the total energy. This definition of local energy helps us to visualize the local degree of mechanical relaxation in the sample. The obtained profile of the local energy is shown in Figure 6.6(a). Most of the elastic energy is concentrated on

top of the bubble, and the energy is gradually decreasing as the edge of the bubble is approached. The shape of the energy profile in the radial direction does not completely follow the form of the bubble, as shown in Figure 6.6(b), which may be important when engineering the strain-induced pseudo-magnetic fields.⁹⁴ In particular, the energy and therefore strain at the top of the bubble remains rather constant when the number of trapped molecules increases from $N = 9 \times 10^3$ to $N = 20 \times 10^3$. On the other hand, the distribution of the strain becomes more homogeneous as the number of trapped molecules increases, which results in less homogeneous pseudo-magnetic fields. In Figure 6.6(c) we observe that as the volume of the bubble increases, the bond stretching terms contribute most to the total elastic energy of the bubble, and the strain arising from this type of elastic deformation is therefore dominant. Actually, when estimating the strain, the contribution coming from shearing and out-of-plane deformation can be, in a very good approximation, neglected, which should therefore simplify the calculations related to the pseudo-magnetic fields.

6.4 Conclusion ---

In conclusion, we have shown that a simple elastic semi-empirical potential combined with an effective substrate potential can accurately predict the universal shape of a gas bubble trapped between graphene and a substrate. With the help of numerical simulations we have shown that this universal behavior holds in small sized bubbles (~ 10 nm) with the van der Waals pressure ~ 1 GPa. We find that the ratio of height and radius of a bubble scales as power law of the adhesion energy ($\sim K^{1/4}$). Furthermore, we have argued that the vibrational spectrum can be used as an independent probe of the shape of a trapped gas bubble. The obtained elastic energy distribution in the bubble shows that by manipulating the bond stretching and shearing, one can control strain engineering of the bubbles which is important for manipulating graphene's electronic, mechanical, adhesive and optical properties. The confinement pressure (vdW) and its effect should be taken into account in studies of various van der Waals heterostructures and can also be used to manipulate and modify the properties of trapped materials at the interfaces. In future, this computational approach can be useful to simulate other van der Waals heterostructures such as h-BN, Mo₂S, and WSe₂.

SUMMARY

The discovery of graphene has provoked a revolution in nanotechnology, as the structural, thermal, and electronic properties of graphene make it a very useful component for a large variety of devices. Structural defects in graphene can have a significant impact on the physical properties of graphene. Defects cause effects that have a long range, therefore, there was a need for an empirical potential which can accurately predict the long-range structural relaxations in graphene that originate from different kinds of intrinsic defects. With the help of numerical simulations we study the long-range buckling effect in graphene and bilayer graphene.

In Chapter 2, we discuss a new semiempirical potential for graphene that allows out-of-plane relaxations. We have fitted the parameters to density functional theory (DFT) calculations performed on simulation cells with a small number of atoms, but the semiempirical potential can be used for configurations with millions of atoms. Using this potential, we analyze the effect of different kinds of defects (SW defect, line dislocations, and grain boundaries) on the out-of-plane buckling in graphene. When out-of-plane relaxation is allowed, there is an effective long-range structural relaxation which drastically decreases the defect formation energies i.e by a factor of 2 or 3. Another important result concerns a long-standing paradox of the divergence in the energy of a separating SW defect. A separating pair of dislocations costs an energy which increases logarithmically with distance, as theoretically expected, but only if the sample is constrained to two dimensions. When relaxation in the third dimension is allowed, the energy does not diverge logarithmically. Moreover, in the 2D confined case a separating pair of dislocations feels an attractive interaction, while in the free-floating graphene with relaxation in the out-of-plane direction, the interaction becomes repulsive.

In Chapter 3, we show using computer simulations how the crystallinity of the graphene samples can be characterized by their vibrational spectrum. In particular, we find that the density of vibrational modes can be used to identify the presence of the structural lattice defects, both point and line defects, in both 2D and buckled samples. We show that these defects in flat graphene give rise to distinct features in the VDOS at high-frequencies, whereas the VDOS in the defected buckled graphene shows prominent features in the low-frequency region. Specifically, for grain boundaries made of pentagon-heptagon pairs, we show that they lead to a shift of the characteristic vibrational D mode towards higher frequency; this distinguishes these line defects from the point SW defects, which do not lead to such a shift.

Lattice defects are inevitably present in two-dimensional crystalline materials with direct implications on their physical and chemical properties. The main characteristic of the lattice defects is their formation energy and in Chapter 4, we show that contrary to the standard belief, different boundary conditions yield different formation energies for lattice defects in buckled 2D materials. On top of an energetic difference in the thermodynamic limit, buckled 2D materials also have finite-size corrections which scale inversely proportional to the logarithm of system size, instead of the common power-law corrections in ordinary 1D, 2D and 3D materials. We show this unusual behavior first in simple, analytically tractable string and membrane models embedded in a higher-dimensional space. We further demonstrate this effect by numerically studying buckled graphene.

In Chapter 5, we present an effective combination of elastic potentials to study large bilayer graphene samples. We combine a recently developed semiempirical potential for single-layer graphene with a new out-of-plane deformation term and an often-used registry-dependent interlayer graphitic Kolmogorov-Crespi potential to simulate twisted bilayer graphene (TBLG) samples with very small mismatch angles. This novel combination of potentials is computationally very cheap but accurate and precise at the same time, allowing us to study very large samples, which is necessary to reach very small mismatch angles in periodic samples. These large samples show properties different from smaller ones. Our study shows that vortices appearing in the Moiré patterns in the TBLG samples converge to a constant size in the thermodynamic limit. Furthermore, the well-known sinusoidal behavior of energy and buckling no longer persists once the misorientation angle becomes very small. We also show that there is a significant buckling after the relaxation in the samples, with the buckling height proportional to the system size. The characteristic average separation between the layers also becomes constant in the thermodynamic limit.

In Chapter 6, we use our semiempirical potential for single-layer graphene combined with a relatively simple and effective model to simulate adhesion between graphene and substrate. This novel combination of potentials is accurate and precise to study small nanobubbles (~ 10 nm). With our numerical simulations, we show that the graphene nanobubbles exhibit a universal shape behavior irrespective of their sizes. In small sized bubbles (~ 10 nm) the vdW pressure is in the order of 1 GPa which can have direct consequence on the properties of trapped materials. We find that the ratio of height and radius of a bubble scales as a power-law of the adhesion energy. Furthermore, we show that the vibrational spectrum can be used as an independent probe of the volume and shape of the trapped gas bubble. We also show that variations of the volume of the trapped gas lead to variations in the bond stretching, shearing, and adhesion; one can thus control strain engineering of the bubbles which is very important for manipulating graphene's mechanical and electronic properties.

SAMENVATTING

De ontdekking van grafeen heeft een revolutie in de nanotechnologie veroorzaakt, doordat de structurele, thermische en elektronische eigenschappen van grafeen het een zeer geschikt materiaal maken voor een grote verscheidenheid aan toepassingen. Structurele defecten in grafeen kunnen een grote invloed op de fysische eigenschappen hebben, en zijn daarom een belangrijk onderzoeksonderwerp. Omdat de effecten van structurele defecten van lange dracht zijn, zijn grote simulatiecellen nodig om ze te bestuderen. Voor deze simulaties is er behoefte aan een empirische potentiaal die nauwkeurig de grootschalige structurele relaxatie van grafeen met defecten kan voorspellen. In deze scriptie ontwikkelen we een dergelijke potentiaal en gebruiken we hem om met behulp van numerieke simulaties de grootschalige kromming in enkel- en dubbel-laags grafeen te bestuderen.

In Hoofdstuk 2 presenteren we een nieuwe semi-empirische potentiaal die geschikt is voor de simulatie van grafeen met kromming. De parameters in deze potentiaal zijn afkomstig van dichtheidsfunctionaaltheorie (DFT) berekeningen aan simulatiecellen met een klein aantal atomen, maar de semi-empirische potentiaal kan worden gebruikt voor simulaties met miljoenen atomen. Met behulp van deze potentiaal analyseren we de kromming die verschillende soorten defecten (Stone-Wales (SW) defecten, lijndislocaties en domeingrenzen) veroorzaken in grafeen. Door de relaxatie uit het platte vlak is er een effectieve lange-afstands structurele relaxatie die de formatie-energie vermindert met maar liefst een factor 2 tot 3. Een ander belangrijk resultaat betreft de aloude paradox van de divergentie in de energie behorend bij het opbreken van een SW defect in twee dislocaties. Deze scheiding kost een energie die logaritmisch toeneemt met de afstand, zoals theoretisch verwacht, maar alleen als het grafeen ingebed is in het tweedimensionale (2D) platte vlak. Bij relaxatie in de derde dimensie, dus als kromming toegestaan is, divergeert de energie niet langer logaritmisch. Sterker nog, waar in het 2D geval een paar scheidende dislocaties een aantrekkende interactie voelt, is deze interactie afstotend in vrij-zwevend grafeen met relaxatie uit het vlak.

In Hoofdstuk 3 tonen wij met computersimulaties aan hoe de kristalliniteit van stukjes grafeen kan worden bepaald uit het vibratiespectrum (VDOS). In het bijzonder vinden we dat de dichtheid van trillingsmodes kan worden gebruikt om de aanwezigheid van punt- en lijndefecten te identificeren, zowel in 2D als in gekromde monsters. We laten zien dat deze defecten in plat grafeen aanleiding geven tot verschillende eigenschappen in de VDOS in het hoogfrequente gebied, terwijl de VDOS in het kromgetrokken grafeen opvallende kenmerken toont in het laagfrequente gebied. Specifiek voor domeingrenzen van pentagon-heptagon

paren laten we zien dat deze leiden tot een verschuiving van de karakteristieke vibrationele D-mode in de richting van een hogere frequentie; dit onderscheidt deze lijn-defecten van punt-defecten (SW), die niet leiden tot een dergelijke verschuiving.

Roosterdefecten zijn onvermijdelijk aanwezig in tweedimensionale kristallijne materialen, en hebben directe gevolgen voor de fysische en chemische eigenschappen. Het belangrijkste kenmerk van roosterdefecten is hun formatie-energie. In Hoofdstuk 4 laten we zien dat, in tegenstelling tot de standaard aanname, in gekromde 2D materialen verschillende randvoorwaarden leiden tot verschillende formatie-energieën van roosterdefecten. Bovenop dit energetische verschil in de thermodynamische limiet, verschillen de gekromde 2D materialen ook in de correcties voor eindige afmetingen, die omgekeerd evenredig zijn met de logaritme van de systeemgrootte, in tegenstelling tot de gebruikelijke machtswet-correcties in 1D, 2D en 3D materialen. We tonen dit ongewoon gedrag eerst aan in eenvoudige, analytisch behandelbare snaar- en membraan-modellen ingebed in een hoger dimensionale ruimte. Vervolgens demonstreren we dit effect in numerieke simulaties van grafeen.

In Hoofdstuk 5 presenteren wij een effectieve combinatie van elastische potentialen om grote dubbel-laags grafeen configuraties met zeer kleine onderlinge verdraaiingshoek (TBLG) te bestuderen. Hiervoor combineren een recent ontwikkelde semi-empirische potentiaal voor enkel-laags grafeen met een nieuwe term voor kromming, en met een veelgebruikte potentiaal voor de interactie tussen de grafeenlagen ontwikkeld door Kolmogorov en Crespi. Deze nieuwe combinatie van potentialen is tegelijkertijd nauwkeurig en zeer efficiënt, waardoor we zeer grote simulatiecellen met periodieke randvoorwaarden kunnen bestuderen, die noodzakelijk zijn voor zeer kleine draaiingshoeken. Deze grote simulatiecellen blijken andere eigenschappen te tonen dan kleinere. Onze studie toont aan dat er wervels te zien zijn in de Moiré patronen in de TBLG monsters, en dat deze wervels convergeren naar een constante grootte in de thermodynamische limiet. Bovendien houdt het bekende sinusoidale gedrag van energie en kromming niet langer stand bij zeer kleine draaiingshoeken. We laten ook zien dat er een aanzienlijke kromtrekking is na relaxatie, met een krommingsamplitude die evenredig is met de systeemgrootte. De kenmerkende gemiddelde afstand tussen de lagen wordt constant in de thermodynamische limiet.

In Hoofdstuk 6 gebruiken wij de semi-empirische potentiaal voor enkel-laags grafeen in een relatief eenvoudig en effectief model om de interactie tussen substraat en grafeen te simuleren. Hiermee bestuderen wij nanobubbels, kleine gasbelletjes ingevangen tussen grafeen en substraat (~ 10 nm). Met onze numerieke simulaties wordt aangetoond dat deze nanobubbels een universele vorm aannemen, ongeacht hun grootte. In kleine bubbels (~ 10 nm) is de

gasdruk in de orde van 1 GPa, wat grote gevolgen heeft voor de eigenschappen van de ingevangen gassen. We zien dat de verhouding van lengte en straal van een bubbel schaalt als een machtswet van de bindingsenergie. Verder laten we zien dat het vibratiespectrum kan worden gebruikt om de omvang van het ingevangen gasbelletje te bepalen. Ook leiden variaties van het volume van het ingesloten gas tot variaties in de uitrekking van koolstofbindingen, en in lokale afschuiving ("shear"); men kan dus door variatie in de gasbelletjes de mechanische en elektronische eigenschappen van het grafeen manipuleren.

BIBLIOGRAPHY

- [1] D. D. L. Chung. Review graphite. *J. Mater. Sci.*, 37:1475, 2002.
- [2] A. K. Geim. Graphene: Status and prospects. *Science*, 324:1530, 2009.
- [3] R. Saito, G. Dresselhaus, and M. S. Dresselhaus. *Physical Properties of Carbon Nanotubes*. Imperial College Press, London, 1998.
- [4] J.-Christophe Charlier, X. Blase, and S. Roche. Electronic and transport properties of nanotubes. *Rev. Mod. Phys.*, 79:677, 2007.
- [5] W. Andreoni. The physics of fullerene-based and fullerene-related materials. *Physics and Chemistry of Materials with Low-Dimensional Structures*, 2000.
- [6] K. S. Novoselov, A. K. Geim, S. V. Morozov, D. Jiang, Y. Zhang, S. V. Dubonos, I. V. Grigorieva, and A. A. Firsov. Electric field effect in atomically thin carbon films. *Science*, 306:666, 2004.
- [7] N. D. Mermin and H. Wagner. Absence of ferromagnetism or antiferromagnetism in one- or two-dimensional isotropic Heisenberg models. *Phys. Rev. Lett.*, 17:1133, 1966.
- [8] N. D. Mermin. Crystalline order in two dimensions. *Phys. Rev.*, 176:250, 1968.
- [9] K. S. Novoselov, A. K. Geim, S. V. Morozov, D. Jiang, M. I. Katsnelson, I. V. Grigorieva, S. V. Dubonos, and A. A. Firsov. Two-dimensional gas of massless Dirac fermions in graphene. *Nature*, 438:197, 2005.
- [10] A. A. Balandin, S. Ghosh, W. Bao, I. Calizo, D. Teweldebrhan, F. Miao, and C. N. Lau. Superior thermal conductivity of single-layer graphene. *Nano Lett.*, 8:902, 2008.
- [11] A. H. Castro Neto, F. Guinea, N. M. R. Peres, K. S. Novoselov, and A. K. Geim. The electronic properties of graphene. *Rev. Mod. Phys.*, 81:109, 2009.
- [12] C. Soldano, A. Mahmood, and E. Dujardin. Production, properties and potential of graphene. *Carbon*, 48:2127, 2010.
- [13] C. Lee, X. Wei, J. W. Kysar, and J. Hone. Measurement of the elastic properties and intrinsic strength of monolayer graphene. *Science*, 321:385, 2008.
- [14] Y. Liu, B. Xie, Z. Zhang, Q. Zheng, and Z. Xu. Mechanical properties of graphene papers. *J. Mech. Phys. Solids*, 60:591, 2012.
- [15] S. Li, Q. Li, R. W. Carpick, P. Gumbsch, X. Z. Liu, X. Ding, J. Sun, and J. Li. The evolving quality of frictional contact with graphene. *Nature*, 539:541, 2016.
- [16] W. A. de Heer, C. Berger, X. Wu, M. Sprinkle, Y. Hu, M. Ruan, J. A. Stroscio, P. N. First, R. Haddon, B. Piot, and et al. Epitaxial graphene electronic structure and transport. *J. Phys. D: Appl. Phys.*, 43:374007, 2010.
- [17] J.-H. Lee, E. K. Lee, W.-J. Joo, Y. Jang, B.-S. Kim, J. Y. Lim, S.-H. Choi, S. J. Ahn, J. R. Ahn, M.-H. Park, and et al. Wafer-scale growth of single-crystal monolayer graphene on reusable hydrogen-terminated germanium. *Science*, 344:286, 2014.
- [18] Y. Zhang, L. Zhang, and C. Zhou. Review of chemical vapor deposition of graphene and related applications. *Acc. Chem. Res.*, 46:2329, 2013.

- [19] I. Pletikosic, M. Kralj, P. Pervan, R. Brako, J. Coraux, A. T. N'Diaye, C. Busse, and T. Michely. Dirac cones and minigaps for graphene on ir(111). *Phys. Rev. Lett.*, 102:056808, 2009.
- [20] A. Fasolino, J. H. Los, and M. I. Katsnelson. Intrinsic ripples in graphene. *Nat. Mat.*, 6:858, 2007.
- [21] H.-Shen Shen, Y.-Mou Xu, and C.-Li Zhang. Graphene: Why buckling occurs? *Appl. Phys. Lett.*, 102:131905, 2013.
- [22] J. C. Meyer, C. Kisielowski, R. Erni, Marta D. Rossell, M. F. Crommie, and A. Zettl. Direct imaging of lattice atoms and topological defects in graphene membranes. *Nano Lett.*, 8:3582, 2008.
- [23] F. Banhart, J. Kotakoski, and A. V. Krashenninnikov. Structural defects in graphene. *ACS Nano*, 5:26, 2011.
- [24] O. V. Yazyev and Y. P. Chen. Polycrystalline graphene and other two-dimensional materials. *Nat. Nanotechnol.*, 9:755, 2014.
- [25] H. I. Rasool, C. Ophus, Z. Zhang, M. F. Crommie, B. I. Yakobson, and A. Zettl. Conserved atomic bonding sequences and strain organization of graphene grain boundaries. *Nano Lett.*, 14:7057, 2014.
- [26] Y. Tison, J. Lagoute, V. Repain, C. Chacon, Y. Girard, F. Joucken, R. Sporken, F. Gargiulo, O. V. Yazyev, and S. Rousset. Grain boundaries in graphene on SiC(0001) substrate. *Nano Lett.*, 14:6382, 2014.
- [27] A.J. Stone and D.J. Wales. Theoretical studies of icosahedral C₆₀ and some related species. *Chem. Phys. Lett.*, 128:501, 1986.
- [28] M. M. Ugeda, I. Brihuega, F. Guinea, and J. M. Gomez-Rodriguez. Missing atom as a source of carbon magnetism. *Phys. Rev. Lett.*, 104:096804, 2010.
- [29] E. Y. Andrei, G. Li, and X. Du. Electronic properties of graphene: A perspective from scanning tunneling microscopy and magnetotransport. *Rep. Prog. Phys.*, 75:056501, 2012.
- [30] A. Hashimoto, K. Suenaga, A. Gloter, K. Urita, and S. Iijima. Direct evidence for atomic defects in graphene layers. *Nature*, 430:870, 2004.
- [31] M. P. Boneschanscher, S. K. Hamalainen, P. Liljeroth, and I. Swart. Sample corrugation affects the apparent bond lengths in atomic force microscopy. *ACS Nano*, 8:3006, 2014.
- [32] Y. Dedkov and E. Voloshina. Multichannel scanning probe microscopy and spectroscopy of graphene Moire structures. *Phys. Chem. Chem. Phys.*, 16:3894, 2014.
- [33] K. N. Kudin, B. Ozbas, H. C. Schniepp, R. K. Prudhomme, I. A. Aksay, and R. Car. Raman spectra of graphite oxide and functionalized graphene sheets. *Nano Lett.*, 8:36, 2008.
- [34] A. C. Ferrari and D. M. Basko. Raman spectroscopy as a versatile tool for studying the properties of graphene. *Nat. Nanotechnol.*, 8:235, 2013.
- [35] D. L. Matz, H. Sojoudi, S. Graham, and J. E. Pemberton. Signature vibrational bands for defects in CVD single-layer graphene by surface-enhanced raman spectroscopy. *J. Phys. Chem. Lett.*, 6:964, 2015.

- [36] V. Lee, C. Park, C. Jaye, D. A. Fischer, Q. Yu, W. Wu, Z. Liu, J. Bao, S.-Shem Pei, C. Smith, and et al. Substrate hybridization and rippling of graphene evidenced by near-edge X-ray absorption fine structure spectroscopy. *J. Phys. Chem. Lett.*, 1:1247, 2010.
- [37] L. R. De Jesus, R. V. Dennis, S. W. Depner, C. Jaye, D. A. Fischer, and S. Banerjee. Inside and outside: X-ray absorption spectroscopy mapping of chemical domains in graphene oxide. *J. Phys. Chem. Lett.*, 4:3144, 2013.
- [38] M. Mohr, J. Maultzsch, E. Dobardzic, S. Reich, I. Milosevic, M. Damnjanvic, A. Bosak, M. Krisch, and C. Thomsen. Phonon dispersion of graphite by inelastic X-Ray scattering. *Phys. Rev. B*, 76:035439, 2007.
- [39] L. Vitali, M. A. Schneider, K. Kern, L. Wirtz, and A. Rubio. Phonon and plasmon excitation in inelastic electron tunneling spectroscopy of graphite. *Phys. Rev. B*, 69:121414(R), 2004.
- [40] J. Cervenka, K. van de Ruit, and C. F. J. Flipse. Giant inelastic tunneling in epitaxial graphene mediated by localized states. *Phys. Rev. B*, 81:205403, 2010.
- [41] M. L. N. Palsgaard, N. P. Andersen, and M. Brandbyge. Unravelling the role of inelastic tunneling into pristine and defected graphene. *Phys. Rev. B*, 91:121403(R), 2015.
- [42] S. Rols, Z. Benes, E. Anglaret, J. L. Sauvajol, P. Papanek, J. E. Fischer, G. Coddens, H. Schober, and A. J. Dianoux. Phonon density of states of single-wall carbon nanotubes. *Phys. Rev. Lett.*, 85:5222, 2000.
- [43] C. Cavallari, D. Pontiroli, M. Jimanez-Ruiz, A. Ivanov, M. Mazzani, M. Gaboardi, M. Aramini, M. Brunelli, M. Ricce, and S. Rols. Hydrogen on graphene investigated by inelastic neutron scattering. *J. Phys.:Conf. Ser.*, 554:012009, 2014.
- [44] G. G. Samsonidze, G. G. Samsonidze, and B. I. Yakobson. Kinetic theory of symmetry-dependent strength in carbon nanotubes. *Phys. Rev. Lett.*, 88:065501, 2002.
- [45] M. Buongiorno Nardelli, B. I. Yakobson, and J. Bernholc. Mechanism of strain release in carbon nanotubes. *Phys. Rev. B*, 57:R4277, 1998.
- [46] L. Li, S. Reich, and J. Robertson. Defect energies of graphite: Density-functional calculations. *Phys. Rev. B*, 72:184109, 2005.
- [47] J. Ma, D. Alfe, A. Michaelides, and E. Wang. Stone-Wales defects in graphene and other planar sp^2 -bonded materials. *Phys. Rev. B*, 80:033407, 2009.
- [48] L. G. Zhou and S.-Qiang Shi. Formation energy of Stone-Wales defects in carbon nanotubes. *Appl. Phys. Lett.*, 83:1222, 2003.
- [49] D. W. Brenner, O. A. Shenderova, J. A. Harrison, S. J. Stuart, B. Ni, and S. B. Sinnott. A second-generation reactive empirical bond order (rebo) potential energy expression for hydrocarbons. *J. Phys. Condens. Matter*, 14:783, 2002.
- [50] D. W. Brenner. Empirical potential for hydrocarbons for use in simulating the chemical vapor deposition of diamond films. *Phys. Rev. B*, 42:9458, 1990.
- [51] J. Tersoff. New empirical approach for the structure and energy of covalent systems. *Phys. Rev. B*, 37:6991, 1988.
- [52] A. C. T. van Duin, S. Dasgupta, F. Lorant, and W. A. Goddard. Reaxff: A reactive force field for hydrocarbons. *J. Phys. Chem. A*, 105:9396, 2001.

- [53] J. G. Kirkwood. The skeletal modes of vibration of long chain molecules. *J. Chem. Phys.*, 7:506, 1939.
- [54] P. N. Keating. Effect of invariance requirements on the elastic strain energy of crystals with application to the diamond structure. *Phys. Rev.*, 145:637, 1966.
- [55] F. Wooten, K. Winer, and D. Weaire. Computer generation of structural models of amorphous Si and Ge. *Phys. Rev. Lett.*, 54:1392, 1985.
- [56] G. T. Barkema and N. Mousseau. High-quality continuous random networks. *Phys. Rev. B*, 62:4985, 2000.
- [57] T. Ohta, A. Bostwick, T. Seyller, K. Horn, and E. Rotenberg. Controlling the electronic structure of bilayer graphene. *Science*, 313:951, 2006.
- [58] A. Reina, X. Jia, J. Ho, D. Nezich, H. Son, V. Bulovic, M. S. Dresselhaus, and J. Kong. Large area, few-layer graphene films on arbitrary substrates by chemical vapor deposition. *Nano Lett.*, 9:30, 2009.
- [59] A. K. Geim and I. V. Grigorieva. Van der Waals heterostructures. *Nature*, 499:419, 2013.
- [60] C.-Chieh Lu, Y.-Chang Lin, Z. Liu, C.-Hui Yeh, K. Suenaga, and P.-Wen Chiu. Twisting bilayer graphene superlattices. *ACS Nano*, 7:2587, 2013.
- [61] C. R. Woods, L. Britnell, A. Eckmann, R. S. Ma, J. C. Lu, H. M. Guo, X. Lin, G. L. Yu, Y. Cao, R.A. V. Gorbachev, and et al. Commensurate-incommensurate transition in graphene on hexagonal boron nitride. *Nat. Phys.*, 10:451, 2014.
- [62] M. Neek-Amal, P. Xu, D. Qi, P. M. Thibado, L. O. Nyakiti, V. D. Wheeler, R. L. Myers-Ward, C. R. Eddy, D. K. Gaskill, and F. M. Peeters. Membrane amplitude and triaxial stress in twisted bilayer graphene deciphered using first-principles directed elasticity theory and scanning tunneling microscopy. *Phys. Rev. B*, 90:064101, 2014.
- [63] M. Neek-Amal and F. M. Peeters. Graphene on boron-nitride: Moiré pattern in the van der Waals energy. *Appl. Phys. Lett.*, 104:041909, 2014.
- [64] E. J. Mele. Commensuration and interlayer coherence in twisted bilayer graphene. *Phys. Rev. B*, 81:161405, 2010.
- [65] J. M. B. Lopes de Santos, N. M. R. Peres, and A. H. Castro Neto. Graphene bilayer with a twist: Electronic structure. *Phys. Rev. Lett.*, 99:256802, 2007.
- [66] S. Shallcross, S. Sharma, and O. A. Pankratov. Quantum interference at the twist boundary in graphene. *Phys. Rev. Lett.*, 101:056803, 2008.
- [67] R. de Gail, M. O. Goerbig, F. Guinea, G. Montambaux, and A. H. Castro Neto. Topologically protected zero modes in twisted bilayer graphene. *Phys. Rev. B*, 84:045436, 2011.
- [68] R. Bistritzer and A. H. MacDonald. Moire butterflies in twisted bilayer graphene. *Phys. Rev. B*, 84:035440, 2011.
- [69] E. Suarez Morell, P. Vargas, L. Chico, and L. Brey. Charge redistribution and interlayer coupling in twisted bilayer graphene under electric fields. *Phys. Rev. B*, 84:195421, 2011.
- [70] D.-Hun Chae, D. Zhang, X. Huang, and K. von Klitzing. Electronic transport in two stacked graphene monolayers. *Nano Lett.*, 12:3905, 2012.

- [71] B. Roy and K. Yang. Bilayer graphene with parallel magnetic field and twisting: Phases and phase transitions in a highly tunable Dirac system. *Phys. Rev. B*, 88:241107(R), 2013.
- [72] M. Pelc, E. S. Morell, L. Brey, and L. Chico. Electronic conductance of twisted bilayer nanoribbon flakes. *J. Phys. Chem. C*, 119:10076, 2015.
- [73] P. Moon and M. Koshino. Optical absorption in twisted bilayer graphene. *Phys. Rev. B*, 87:205404, 2013.
- [74] C. J. Tabert and E. J. Nicol. Optical conductivity of twisted bilayer graphene. *Phys. Rev. B*, 87:121402, 2013.
- [75] M. De Corato, C. Cocchi, D. Prezzi, M. J. Caldas, E. Molinari, and A. Ruini. Optical properties of bilayer graphene nanoflakes. *J. Phys. Chem. C*, 118:23219, 2014.
- [76] Long-Jing Yin, Jia-Bin Qiao, Wen-Xiao Wang, Wei-Jie Zuo, Wei Yan, Rui Xu, Rui-Fen Dou, Jia-Cai Nie, and Lin He. Landau quantization and fermi velocity renormalization in twisted graphene bilayers. *Phys. Rev. B*, 92:201408(R), 2015.
- [77] E. Suarez Morell, J. D. Correa, P. Vargas, M. Pacheco, and Z. Barticevic. Flat bands in slightly twisted bilayer graphene: Tight-binding calculations. *Phys. Rev. B*, 82:121407(R), 2010.
- [78] L. Xian, Z. F. Wang, and M. Y. Chou. Coupled dirac fermions and neutrino-like oscillations in twisted bilayer graphene. *Nano Lett.*, 13:5159, 2013.
- [79] G. Trambly de Laissardiere, D. Mayou, and L. Magaud. Localization of dirac electrons in rotated graphene bilayers. *Nano Lett.*, 10:804, 2010.
- [80] Z. F. Wang, Feng Liu, and M. Y. Chou. Fractal landau-level spectra in twisted bilayer graphene. *Nano Lett.*, 12:3833, 2012.
- [81] J. Hass, F. Varchon, J. E. Millan-Otoya, M. Sprinkle, N. Sharma, W. A. de Heer, C. Berger, P. N. First, L. Magaud, and E. H. Conrad. Why multilayer graphene on 4h-SiC (0001) behaves like a single sheet of graphene. *Phys. Rev. Lett.*, 100:125504, 2008.
- [82] A. Luican, G. Li, A. Reina, J. Kong, R. R. Nair, K. S. Novoselov, A. K. Geim, and E. Y. Andrei. Single-layer behavior and its breakdown in twisted graphene layers. *Phys. Rev. Lett.*, 106:126802, 2011.
- [83] J.-Bo Liu, P.-Jian Li, Y.-Fu Chen, Z.-Gao Wang, F. Qi, J.-Rui He, B.-Jie Zheng, J.-Hao Zhou, W.-Li Zhang, L. Gu, and et al. Observation of tunable electrical bandgap in large-area twisted bilayer graphene synthesized by chemical vapor deposition. *Sci. Reports*, 5:15285, 2015.
- [84] D. S. Lee, C. Riedl, T. Beringer, A. H. Castro Neto, K. von Klitzing, U. Starke, and J. H. Smet. Quantum hall effect in twisted bilayer graphene. *Phys. Rev. Lett.*, 107:216602, 2011.
- [85] Y. Kim, H. Yun, S.-Geol Nam, M. Son, D. S. Lee, D. C.l Kim, S. Seo, H. C. Choi, H.-Jong Lee, S. W. Lee, and et al. Breakdown of the interlayer coherence in twisted bilayer graphene. *Phys. Rev. Lett.*, 110:096602, 2013.
- [86] Karolina Z. Milowska, Magdalena Woiska, and Malgorzata Wierzbowska. Contrasting elastic properties of heavily B- and N-doped graphene with random impurity distributions including aggregates. *J. Phys. Chem. C*, 117:20229, 2013.

- [87] E. Stolyarova, D. Stolyarov, K. Bolotin, S. Ryu, L. Liu, K. T. Rim, M. Klima, M. Hybertsen, I. Pogorelsky, I. Pavlishin, and et al. Observation of graphene bubbles and effective mass transport under graphene films. *Nano Lett.*, 9:332, 2009.
- [88] T. Georgiou, L. Britnell, P. Blake, R. V. Gorbachev, A. Gholinia, A. K. Geim, C. Casiraghi, and K. S. Novoselov. Graphene bubbles with controllable curvature. *Applied Physics Letters*, 99:093103, 2011.
- [89] A. Ben Gouider Trabelsi, F. V. Kusmartsev, B. J. Robinson, A. Ouerghi, O. E. Kusmartseva, O. V. Kolosov, R. Mazzocco, M. B. Gaifullin, and M. Oueslati. Charged nano-domes and bubbles in epitaxial graphene. *Nanotechnology*, 25:165704, 2014.
- [90] G. Zamborlini, M. Imam, L. L. Patera, T. O. Montes, N. Stojic, C. Africh, A. Sala, N. Binggeli, G. Comelli, and A. Locatelli. Nanobubbles at GPa pressure under graphene. *Nano Lett.*, 15:6162, 2015.
- [91] S. J. Haigh, A. Gholinia, R. Jalil, S. Romani, L. Britnell, D. C. Elias, K. S. Novoselov, L. A. Ponomarenko, A. K. Geim, and R. Gorbachev. Cross-sectional imaging of individual layers and buried interfaces of graphene-based heterostructures and superlattices. *Nat. Mater.*, 11:764, 2012.
- [92] A. V. Kretinin, Y. Cao, J. S. Tu, G. L. Yu, R. Jalil, K. S. Novoselov, S. J. Haigh, A. Gholinia, A. Mishchenko, M. Lozada, and et al. Electronic properties of graphene encapsulated with different two-dimensional atomic crystals. *Nano Lett.*, 14:3270, 2014.
- [93] J. Zabel, R. R. Nair, A. Ott, T. Georgiou, A. K. Geim, K. S. Novoselov, and C. Casiraghi. Raman spectroscopy of graphene and bilayer under biaxial strain: Bubbles and balloons. *Nano Lett.*, 12:617, 2012.
- [94] N. Levy, S. A. Burke, K. L. Meaker, M. Panlasigui, A. Zettl, F. Guinea, A. H. C. Neto, and M. F. Crommie. Strain-induced pseudo-magnetic fields greater than 300 Tesla in graphene nanobubbles. *Science*, 329:544, 2010.
- [95] K. S. Vasu, E. Prestat, J. Abraham, J. Dix, R. J. Kashtiban, J. Beheshtian, J. Sloan, P. Carbone, M. Neek-Amal, S. J. Haigh, and et al. Van der Waals pressure and its effect on trapped interlayer molecules. *Nat. Commun.*, 7:12168, 2016.
- [96] S. Jiao, C. Duan, and Z. Xu. Water under the cover: Structures and thermodynamics of water encapsulated by graphene. *arXiv preprint arXiv:1509.07215*, 2016.
- [97] K. Xu, P. Cao, and J. R. Heath. Graphene visualizes the first water adlayers on mica at ambient conditions. *Science*, 329:1188, 2010.
- [98] G. Algara-Siller, O. Lehtinen, F. C. Wang, R. R. Nair, U. Kaiser, H. A. Wu, A. K. Geim, and I. V. Grigorieva. Square ice in graphene nanocapillaries. *Nature*, 519:443, 2015.
- [99] J. M. Yuk, J. Park, P. Ercius, K. Kim, D. J. Hellebusch, M. F. Crommie, J. Y. Lee, A. Zettl, and A. P. Alivisatos. High-resolution EM of colloidal nanocrystal growth using graphene liquid cells. *Science*, 336:61, 2012.
- [100] J. Park, H. Park, P. Ercius, A. F. Pegoraro, C. Xu, J. W. Kim, S. H. Han, and D. A. Weitz. Direct observation of wet biological samples by graphene liquid cell transmission electron microscopy. *Nano Lett.*, 15:4737, 2015.
- [101] M. Wojcik, M. Hauser, W. Li, S. Moon, and K. Xu. Graphene-enabled electron microscopy and correlated super-resolution microscopy of wet cells. *Nat. Commun.*, 6:7384, 2015.

- [102] J. Lu, A.H. Castro Neto, and K. P. Loh. Transforming moire blisters into geometric graphene nano-bubbles. *Nat. Commun.*, 3:823, 2012.
- [103] M. Neek-Amal and F. M. Peeters. Strain-engineered graphene through a nanostructured substrate. i. deformations. *Phys. Rev. B*, 85:195445, 2012.
- [104] J. S. Bunch, S. S. Verbridge, J. S. Alden, A. M. van der Zande, J. M. Parpia, H. G. Craighead, and P. L. McEuen. Impermeable atomic membranes from graphene sheets. *Nano Lett.*, 8:2458, 2008.
- [105] O. Leenaerts, B. Partoens, and F. M. Peeters. Graphene: A perfect nanoballoon. *Appl. Phys. Lett.*, 93:193107, 2008.
- [106] S. P. Koenig, N. G. Boddeti, M. L. Dunn, and J. S. Bunch. Ultrastrong adhesion of graphene membranes. *Nat. Nanotech.*, 6:543, 2011.
- [107] E. Khestanova, F. Guinea, L. Fumagalli, A. K. Geim, and I. V. Grigorieva. Universal shape and pressure inside bubbles appearing in van der Waals heterostructures. *Nat. Commun.*, 7:12587, 2016.
- [108] Y. Zhang, Y.-Wen Tan, H. L. Stormer, and P. Kim. Experimental observation of the quantum hall effect and Berry's phase in graphene. *Nature*, 438:201, 2005.
- [109] A. K. Geim and K. S. Novoselov. The rise of graphene. *Nat. Mater.*, 6:183, 2007.
- [110] A. Mesaros, D. Sadri, and J. Zaanen. Berry phase of dislocations in graphene and valley conserving decoherence. *Phys. Rev. B*, 79:155111, 2009.
- [111] J.-Hao Chen, L. Li, W. G. Cullen, E. D. Williams, and M. S. Fuhrer. Tunable kondo effect in graphene with defects. *Nat. Phys.*, 7:535, 2011.
- [112] M.I. Katsnelson and A.K. Geim. Electron scattering on microscopic corrugations in graphene. *Philos. Trans. R. Soc.*, 366:195, 2008.
- [113] S. Bhowmick and U. V. Waghmare. Anisotropy of the Stone-Wales defect and warping of graphene nanoribbons: A first-principles analysis. *Phys. Rev. B*, 81:155416, 2010.
- [114] T. Zhang, X. Li, and H. Gao. Defects controlled wrinkling and topological design in graphene. *J. Mech. and Phys. Solids*, 67:2, 2014.
- [115] C. G. Wang, L. Lan, Y. P. Liu, and H. F. Tan. Defect-guided wrinkling in graphene. *Comput. Mater. Sci.*, 77:250, 2013.
- [116] O. V. Yazyev and S. G. Louie. Topological defects in graphene: Dislocations and grain boundaries. *Phys. Rev. B*, 81:195420, 2010.
- [117] S. N. Shirodkar and U. V. Waghmare. Electronic and vibrational signatures of Stone-Wales defects in graphene: First-principles analysis. *Phys. Rev. B*, 86:165401, 2012.
- [118] G. G. Samsonidze, G. G. Samsonidze, and B. I. Yakobson. Energetics of Stone-Wales defects in deformations of monoatomic hexagonal layers. *Comput. Mater. Sci.*, 23:62, 2002.
- [119] J. H. Warner, E. R. Margine, M. Mukai, A. W. Robertson, F. Giustino, and A. I. Kirkland. Dislocation-driven deformations in graphene. *Science*, 337:209, 2012.
- [120] J. H. Warner, Y. Fan, A. W. Robertson, K. He, E. Yoon, and G. D. Lee. Rippling graphene at the nanoscale through dislocation addition. *Nano Lett.*, 13:4937, 2013.

- [121] O. Lehtinen, S. Kurasch, A.V. Krashennnikov, and U. Kaiser. Atomic scale study of the life cycle of a dislocation in graphene from birth to annihilation. *Nat. Commun.*, 4:2098, 2013.
- [122] F. H. Stillinger and T. A. Weber. Computer simulation of local order in condensed phases of silicon. *Phys. Rev. B*, 31:5262, 1985.
- [123] N. Mousseau and M. F. Thorpe. Length mismatch in random semiconductor alloys. III. crystalline and amorphous SiGe. *Phys. Rev. B*, 46:15887, 1992.
- [124] G. Kresse and J. Hafner. Ab initio molecular dynamics for liquid metals. *Phys. Rev. B*, 47:558, 1993.
- [125] G. Kresse and J. Furthmuller. Efficient iterative schemes for ab initio total-energy calculations using a plane-wave basis set. *Phys. Rev. B*, 54:11169, 1996.
- [126] J. Klimes, D. R. Bowler, and A. Michaelides. Chemical accuracy for the Van der Waals density functional. *J. Phys.: Condens. Matter*, 22:022201, 2009.
- [127] J. Klimes, D. R. Bowler, and A. Michaelides. Van der Waals density functionals applied to solids. *Phys. Rev. B*, 83:195131, 2011.
- [128] M. Dion, H. Rydberg, E. Schröder, D. C. Langreth, and B. I. Lundqvist. Van der Waals density functional for general geometries. *Phys. Rev. Lett.*, 92:246401, 2004.
- [129] H. J. Monkhorst and J. D. Pack. Special points for brillouin-zone integrations. *Phys. Rev. B*, 13:5188, 1976.
- [130] A. Kumar, M. Wilson, and M. F. Thorpe. Amorphous graphene: A realization of Zachariasen’s glass. *J. Phys.: Condens. Matter*, 24:485003, 2012.
- [131] J. M. Kosterlitz and D. J. Thouless. Ordering, metastability and phase transitions in two-dimensional systems. *J. Phys. C: Solid State Phys.*, 6:1181, 1973.
- [132] D. R. Nelson and B. I. Halperin. Dislocation-mediated melting in two dimensions. *Phys. Rev. B*, 19:2457, 1979.
- [133] A. P. Young. Melting and the vector coulomb gas in two dimensions. *Phys. Rev. B*, 19:1855, 1979.
- [134] G. Voronoi. Nouvelles applications des parames continus thie des formes quadratiques. *Angew. Math.*, 1908:97, 1908.
- [135] S. Kurasch, J. Kotakoski, O. Lehtinen, V. Skakalova, J. Smet, C.E. Krill, A. V. Krashennnikov, and U. Kaiser. Atom-by-atom observation of grain boundary migration in graphene. *Nano Lett.*, 12:3168, 2012.
- [136] X. Du, I. Skachko, A. Barker, and E. Y. Andrei. Approaching ballistic transport in suspended graphene. *Nat. Nanotechnol.*, 3:491, 2008.
- [137] K. I. Bolotin, K. J. Sikes, Z. Jiang, M. Klima, G. Fudenberg, J. Hone, P. Kim, and H. L. Stormer. Ultrahigh electron mobility in suspended graphene. *Solid State Commun.*, 146:351, 2008.
- [138] R. R. Nair, H. A. Wu, P. N. Jayaram, I. V. Grigorieva, and A. K. Geim. Unimpeded permeation of water through helium-leak-tight graphene-based membranes. *Science*, 335:442, 2012.

- [139] P. T. Araujo, M. Terrones, and M. S. Dresselhaus. Defects and impurities in graphene-like materials. *Mater. Today*, 15:98, 2012.
- [140] J. Lu, Y. Bao, C. L. Su, and K. P. Loh. Properties of strained structures and topological defects in graphene. *ACS Nano*, 7:8350, 2013.
- [141] L. Liu, M. Qing, Y. Wang, and S. Chen. Defects in graphene: Generation, healing, and their effects on the properties of graphene: A review. *J. Mater. Sci. Technol.*, 31:599, 2015.
- [142] S. Gruyel, B. Hajgata, Y. Dauphin, J.-Marie Blairon, H. Edouard Miltner, F. De Proft, P. Geerlings, and G. Van Lier. Effect of structural defects and chemical functionalisation on the intrinsic mechanical properties of graphene. *Phys. Chem. Chem. Phys.*, 15:659, 2013.
- [143] L. Vicarelli, S. J. Heerema, C. Dekker, and H. W. Zandbergen. Controlling defects in graphene for optimizing the electrical properties of graphene nanodevices. *ACS Nano*, 9:3428, 2015.
- [144] A. Hashimoto, K. Suenaga, A. Gloter, K. Urita, and S. Iijima. Direct evidence for atomic defects in graphene layers. *Nature*, 430:870, 2004.
- [145] J. Kotakoski, A. V. Krashenninnikov, U. Kaiser, and J. C. Meyer. From point defects in graphene to two-dimensional amorphous carbon. *Phys. Rev. Lett.*, 106:105505, 2011.
- [146] A. C. Ferrari, J. C. Meyer, V. Scardaci, C. Casiraghi, M. Lazzeri, F. Mauri, S. Piscanec, D. Jiang, K. S. Novoselov, S. Roth, and et al. Raman spectrum of graphene and graphene layers. *Phys. Rev. Lett.*, 97:187401, 2006.
- [147] A. Jorio, M.S. Dresselhaus, R. Saito, and G. Dresselhaus. *Raman Spectroscopy in Graphene Related Systems*. Wiley VCH, Weinheim, Germany, 2011.
- [148] F. D. Natterer, Y. Zhao, J. Wyrick, Y.-Hao Chan, W.-Ying Ruan, M.-Yin Chou, K. Watanabe, T. Taniguchi, N. B. Zhitenev, and J. A. Stroscio. Strong asymmetric charge carrier dependence in inelastic electron tunneling spectroscopy of graphene phonons. *Phys. Rev. Lett.*, 114:245502, 2015.
- [149] S. K. Jain, G. T. Barkema, N. Mousseau, C.-Ming Fang, and M. A. van Huis. Strong long-range relaxations of structural defects in graphene simulated using a new semiempirical potential. *J. Phys. Chem. C*, 119:9646, 2015.
- [150] Y.-Ying Wang, Z.H. Ni, T. Yu, Z. X. Shen, H.M. Wang, W. Wu, Y.H. and Chen, and Andrew T. Shen W. Raman studies of monolayer graphene: The substrate effect. *J. Phys. Chem. C*, 112:10637, 2008.
- [151] J. D. Wood, S. W. Schmucker, A. S. Lyons, E. Pop, and J. W. Lyding. Effects of polycrystalline Cu substrate on graphene growth by chemical vapor deposition. *Nano Lett.*, 11:4547, 2011.
- [152] S. Malola, H. Hakkinen, and P. Koskinen. Comparison of raman spectra and vibrational density of states between graphene nanoribbons with different edges. *Eur. Phys. J. D*, 52:71, 2009.
- [153] F. Mazzamuto, J. Saint-Martin, A. Valentin, C. Chassat, and P. Dollfus. Edge shape effect on vibrational modes in graphene nanoribbons: A numerical study. *J. Appl. Phys.*, 109:064516, 2011.

- [154] C. Mapelli, C. Castiglioni, G. Zerbi, and K. Mullen. Common force field for graphite and polycyclic aromatic hydrocarbons. *Phys. Rev. B*, 60:12710, 1999.
- [155] A. M. Rao, E. Richter, S. Bandow, B. Chase, P. C. Eklund, K. A. Williams, S. Fang, K. R. Subbaswamy, M. Menon, A. Thess, and et. al. Diameter-selective raman scattering from vibrational modes in carbon nanotubes. *Science*, 275:187, 1997.
- [156] D. M. Basko. Theory of resonant multiphonon raman scattering in graphene. *Phys. Rev. B*, 78:125418, 2008.
- [157] L. N. Bourgeois and L. A. Bursill. High-resolution transmission electron microscopic study of nanoporous carbon consisting of curved single graphitic sheets. *Philos. Mag. A*, 76:753, 1997.
- [158] M. A. Smith, H. C. Foley, and R. F. Lobo. A simple model describes the PDF of a non-graphitizing carbon. *Carbon*, 42:2041, 2004.
- [159] A. Pekker, A. Botos, A. Rusznyak, J. Koltai, J. Kurti, and K. Kamaras. Vibrational signatures in the infrared spectra of single- and double-walled carbon nanotubes and their diameter dependence. *J. Phys. Chem. Lett.*, 2:2079, 2011.
- [160] M. Xin, F. Wang, Y. Meng, C. Tian, M. Jin, Z. Wang, and R. Zhang. Characteristic vibrational modes and electronic structures of carbon nanotubes containing defects. *J. Phys. Chem. C*, 116:292, 2012.
- [161] F. OuYang, B. Huang, Z. Li, J. Xiao, H. Wang, and H. Xu. Chemical functionalization of graphene nanoribbons by carboxyl groups on Stone-Wales defects. *J. Phys. Chem. C*, 112:12003, 2008.
- [162] E. C. Mattson, J. E. Johns, K. Pande, R. A. Bosch, S. Cui, M. Gajdardziska-Josifovska, M. Weinert, J. H. Chen, M. C. Hersam, and C. J. Hirschmugl. Vibrational excitations and low-energy electronic structure of epoxide-decorated graphene. *J. Phys. Chem. Lett.*, 5:212, 2014.
- [163] J.-Hao Chen, W. G. Cullen, C. Jang, M. S. Fuhrer, and E. D. Williams. Defect scattering in graphene. *Phys. Rev. Lett.*, 102:236805, 2009.
- [164] A. Zandiatashbar, G.-Hyoung Lee, S. J. An, S. Lee, N. Mathew, M. Terrones, T. Hayashi, C. R. Picu, J. Hone, and N. Koratkar. Effect of defects on the intrinsic strength and stiffness of graphene. *Nat. Commun.*, 5:3186, 2014.
- [165] C. Lopez-Polin, G. and Gomez-Navarro, V. Parente, F. Guinea, M.I. Katsnelson, F. Porez-Murano, and J. Gomez-Herrero. Increasing the elastic modulus of graphene by controlled defect creation. *Nat. Phys.*, 11:26, 2014.
- [166] R. Grantab, V. B. Shenoy, and R. S. Ruoff. Anomalous strength characteristics of tilt grain boundaries in graphene. *Science*, 330:946, 2010.
- [167] S. T. Skowron, I. V. Lebedeva, A. M. Popov, and E. Bichoutskaia. Energetics of atomic scale structure changes in graphene. *Chem. Soc. Rev.*, 44:3143, 2015.
- [168] J. H. Los, K. V. Zakharchenko, M. I. Katsnelson, and A. Fasolino. Melting temperature of graphene. *Phys. Rev. B*, 91:045415, 2015.
- [169] K. V. Zakharchenko, A. Fasolino, J. H. Los, and M. I. Katsnelson. Melting of graphene: from two to one dimension. *J. Phys. Condens. Matter*, 23:202202, 2011.

- [170] H. S. Seung and David R. Nelson. Defects in flexible membranes with crystalline order. *Phys. Rev. A*, 38:1005, 1988.
- [171] J. M. Carlsson, L. M. Ghiringhelli, and A. Fasolino. Theory and hierarchical calculations of the structure and energetics of [0001] tilt grain boundaries in graphene. *Phys. Rev. B*, 84:165423, 2011.
- [172] E. Ertekin, D. C. Chrzan, and M. S. Daw. Topological description of the Stone-Wales defect formation energy in carbon nanotubes and graphene. *Phys. Rev. B*, 79:155421, 2009.
- [173] J. Kotakoski, A. V. Krashenninnikov, U. Kaiser, and J. C. Meyer. From point defects in graphene to two-dimensional amorphous carbon. *Phys. Rev. Lett.*, 106:105505, 2011.
- [174] P. Y. Huang, C. S. Ruiz-Vargas, A. M. van der Zande, W. S. Whitney, M. P. Levendof, J. W. Kevek, J. S. Garg, S. and Alden, C. J. Hustedt, Y. Zhu, and et al. Grains and grain boundaries in single-layer graphene atomic patchwork quilts. *Nature*, 469:389, 2011.
- [175] A. W. Tsen, L. Brown, R. W. Havener, and J. Park. Polycrystallinity and stacking in CVD graphene. *Acc. Chem. Res.*, 46:2286, 2013.
- [176] C. Xu, L. Wang, Z. Liu, L. Chen, J. Guo, N. Kang, X.-Liang Ma, H.-Ming Cheng, and W. Ren. Large-area high-quality 2D ultrathin Mo_2C superconducting crystals. *Nat. Mater.*, 14:1135, 2015.
- [177] P. Vogt, P. De Padova, C. Quaresima, J. Avila, E. Frantzeskakis, M. C. Asensio, A. Resta, B. Ealet, and G. Le Lay. Silicene: Compelling experimental evidence for graphenelike two-dimensional silicon. *Phys. Rev. Lett.*, 108:155501, 2012.
- [178] B. Feng, Z. Ding, S. Meng, Y. Yao, X. He, P. Cheng, L. Chen, and K. Wu. Evidence of silicene in honeycomb structures of silicon on Ag(111). *Nano Lett.*, 12:3507, 2012.
- [179] E. Bianco, S. Butler, S. Jiang, O. D. Restrepo, W. Windl, and J. E. Goldberger. Stability and exfoliation of germanane: A germanium graphane analogue. *ACS Nano*, 7:4414, 2013.
- [180] F.-feng Zhu, W.-jiong Chen, Y. Xu, C.-lei Gao, D.-dan Guan, C.-hua Liu, D. Qian, S.-Cheng Zhang, and J.-feng Jia. Epitaxial growth of two-dimensional stanene. *Nat. Mater.*, 14:1020, 2015.
- [181] S. Chen and D. C. Chrzan. Continuum theory of dislocations and buckling in graphene. *Phys. Rev. B*, 84:214103, 2011.
- [182] J. C. Meyer, A. K. Geim, M. I. Katsnelson, K. S. Novoselov, T. J. Booth, and S. Roth. The structure of suspended graphene sheets. *Nature*, 446:60, 2007.
- [183] M. Ishigami, J. H. Chen, W. G. Cullen, M. S. Fuhrer, and E. D. Williams. Atomic structure of graphene on SiO_2 . *Nano Letter*, 7:1643, 2007.
- [184] E. Stolyarova, K. T. Rim, S. Ryu, J. Maultzsch, P. Kim, L. E. Brus, T. F. Heinz, M. S. Hybertsen, and G. W. Flynn. High-resolution scanning tunneling microscopy imaging of mesoscopic graphene sheets on an insulating surface. *Proc. Natl. Acad. Sci.*, 104:9209, 2007.
- [185] A. Capasso, E. Placidi, H.F. Zhan, E. Perfetto, J.M. Bell, Y.T. Gu, and N. Motta. Graphene ripples generated by grain boundaries in highly ordered pyrolytic graphite. *Carbon*, 68:330, 2014.

- [186] M. L. Ackerman, P. Kumar, M. Neek-Amal, P. M. Thibado, F. M. Peeters, and S. Singh. Anomalous dynamical behavior of freestanding graphene membranes. *Phys. Rev. Lett.*, 117:126801, 2016.
- [187] B. Butz, C. Dolle, F. Niekel, K. Weber, D. Waldmann, H. B. Weber, B. Meyer, and E. Spiecker. Dislocations in bilayer graphene. *Nature*, 505:533, 2014.
- [188] J. C. Meyer, A. K. Geim, M. I. Katsnelson, K. S. Novoselov, D. Obergfell, S. Roth, C. Girit, and A. Zettl. On the roughness of single- and bi-layer graphene membranes. *Solid State Commun.*, 143:101, 2007. Exploring grapheneRecent research advances.
- [189] J. Lin, W. Fang, W. Zhou, A. R. Lupini, J. C. Idrobo, J. Kong, S. J. Pennycook, and S. T. Pantelides. AC/AB stacking boundaries in bilayer graphene. *Nano Letters*, 13:3262, 2013.
- [190] M. M. van Wijk, A. Schuring, M. I. Katsnelson, and A. Fasolino. Relaxation of moire patterns for slightly misaligned identical lattices: Graphene on graphite. *2D Materials*, 2:034010, 2015.
- [191] S. Dai, Y. Xiang, and D. J. Srolovitz. Structure and energetics of interlayer dislocations in bilayer graphene. *Phys. Rev. B*, 93:085410, 2016.
- [192] S. Dai, Y. Xiang, and D. J. Srolovitz. Twisted bilayer graphene: Moiré a twist. *Nano Letters*, 16:5923, 2016.
- [193] A. N. Kolmogorov and V. H. Crespi. Registry-dependent interlayer potential for graphitic systems. *Phys. Rev. B*, 71:235415, 2005.
- [194] K. Uchida, S. Furuya, J.-Ichi Iwata, and A. Oshiyama. Atomic corrugation and electron localization due to moire patterns in twisted bilayer graphenes. *Phys. Rev. B*, 90:155451, 2014.
- [195] E. Mostaani, N. D. Drummond, and V. I. Falko. Quantum monte carlo calculation of the binding energy of bilayer graphene. *Phys. Rev. Lett.*, 115:115501, 2015.
- [196] J. S. Alden, A. W. Tsen, P. Y. Huang, R. Hovden, L. Brown, J. Park, D. A. Muller, and P. L. McEuen. Strain solitons and topological defects in bilayer graphene. *Proc. Natl. Acad. Sci.*, 110:11256, 2013.
- [197] S. K. Jain, V. Juricic, and G. T. Barkema. Boundaries determine the formation energies of lattice defects in two-dimensional buckled materials. *Phys. Rev. B*, 94:020102(R), 2016.
- [198] J. M. Campanera, G. Savini, I. Suarez-Martinez, and M. I. Heggge. Density functional calculations on the intricacies of moire patterns on graphite. *Phys. Rev. B*, 75:235449, 2007.
- [199] A. H. Castro Neto, F. Guinea, N. M. R. Peres, K. S. Novoselov, and A. K. Geim. The electronic properties of graphene. *Rev. Mod. Phys.*, 81:109, 2009.
- [200] A. D. Smith, F. Niklaus, A. Paussa, S. Vaziri, A. C. Fischer, M. Sterner, F. Forsberg, A. Delin, D. Esseni, P. Palestri, and et al. Electromechanical piezoresistive sensing in suspended graphene membranes. *Nano Lett.*, 13:3237, 2013.
- [201] R. J. Dolleman, D. Davidovikj, S. J. Cartamil-Bueno, H. S. J. van der Zant, and P. G. Steeneken. Graphene squeeze-film pressure sensors. *Nano Lett.*, 16:568, 2016.

- [202] S. J. Cartamil-Bueno, P. G. Steeneken, A. Centeno, A. Zurutuza, H. S. J. van der Zant, and S. Hourri. Colorimetry technique for scalable characterization of suspended graphene. *Nano Lett.*, page 6792, 2016.
- [203] T. Bjorkman, A. Gulans, A. V. Krashennnikov, and R. M. Nieminen. Van der Waals bonding in layered compounds from advanced density-functional first-principles calculations. *Phys. Rev. Lett.*, 108:235502, 2012.
- [204] B. Sachs, T. O. Wehling, M. I. Katsnelson, and A. I. Lichtenstein. Adhesion and electronic structure of graphene on hexagonal boron nitride substrates. *Phys. Rev. B*, 84:195414, 2011.
- [205] S. K. Jain, V. Juricic, and G. T. Barkema. Probing crystallinity of graphene samples via the vibrational density of states. *J. Phys. Chem. Lett.*, 6:3897, 2015.
- [206] P. Wang, W. Gao, Z. Cao, K. M. Liechti, and R. Huang. Numerical analysis of circular graphene bubbles. *J. Appl. Mech.*, 80:040905, 2013.
- [207] K. Yue, W. Gao, R. Huang, and K. M. Liechti. Analytical methods for the mechanics of graphene bubbles. *J. Appl. Phys.*, 112:083512, 2012.
- [208] S. K. Jain, V. Juricic, and G. T. Barkema. Structure of twisted and buckled bilayer graphene. *2D Mater.*, 4:015018, 2016.

ACKNOWLEDGEMENTS

Finally, it's time to acknowledge all the people who were there to make my PhD journey amazing. It is a pleasure for me to express my gratitude to the people who have helped me or have been an important part of my life for the last three and a half years.

First of all, My deepest gratitude goes to Gerard Barkema, my PhD supervisor. I am incredibly thankful for your supervision and inspiring guidance, you have provided me. You have shown great amount of trust on me with all this time that has helped me to pursue the projects I had in mind and do stuff which I wanted to try. I have learnt a lot of skills from you scientifically and non-scientifically. I always knew that whenever you will have even the slightest amount of time from your super busy schedule, you will stop by at my office and ask me about the things. You were and will always be a source of inspiration in my life.

I wish to offer my sincere gratitude to Vladimir Juricic, for the valuable suggestions, guidance and substantial encouragement throughout the course of my research work. I can never forget your incredible hospitality when I was in Stockholm.

I express my sincere thanks and indebtedness to all my collaborators: Normand Mousseau, Marijn van Huis, and Chang-Ming Fang. I truly enjoyed working with you and wish to collaborate further in the future. I want to thank Albert for being a good student, I really enjoyed supervising you.

I am thankful to all the current and previous members of ITF for providing me all the comfort and stimulus environment to carry out my research. I enjoyed all the discussions over lunch and nice coffee breaks, we have had. I feel proud to be part of this family.

I want to thank all my current and previous office-mates for being so nice to me and tolerate all the long discussions Gerard and I used to have in the office.

I am thankful to each and every member of Indian community in Utrecht for all those amazing get-togethers and parties. I had great fun discussing about politics, movies, music, cricket, tennis and other issues with you. All the great trips which we had together will always be in my good memories.

I want to thank all the members of CSER community in Utrecht and outside Utrecht for all those nice discussions and updates over coffee and mithais(sweets).

I am thankful to all my flatmates for being nice people to live with. I enjoyed my time sharing the apartment with you. You never made me feel bored.

I want to thank all my friends back there in India for always being supportive to me.

I recognize with warm appreciation the blessings, moral support, and cooperation provided by my parents and family.

In the end, a special thanks goes to all the nice people whom I have forgotten to mention here.

ABOUT THE AUTHOR

Sandeep Kumar Jain was born on August 30, 1990 in Newai, Rajasthan, India. After completing high school in Newai, he moved to Roorkee, Uttarakhand in 2008. At the Indian Institute of Technology, Roorkee (IITR) he received an Integrated Masters in Science degree in Chemistry with the CGPA of 8.5 in 2013. His Master's project was on the purification of industrial waste water, under the supervision of Prof. Vinod Kumar Gupta. He was recipient of the INSPIRE fellowship from the Department of Science and Technology, India (DST) for his entire graduate studies. During this time he did several internships sponsored by the Indian Academy of Sciences (IAS) on topics related to computer simulations in IISC Bangalore, IIT Delhi, and IIT Bombay. In 2013 he was selected in the Computational Sciences for Energy Research (CSER) initiative of Shell and FOM to do fully sponsored PhD research at one of the Universities in the Netherlands. He started his PhD in Physics at Utrecht University under the supervision of Prof. Gerard Barkema in the same year. His research focused on computer simulations of graphene mechanics. The important results of this study are described in this thesis.